

Are Primordial Black Holes a Natural Dark Matter Candidate?

Stefano Profumo¹

¹*Department of Physics and Santa Cruz Institute for Particle Physics,
University of California, Santa Cruz, California 95064, USA**

(Dated: June 12, 2026)

Primordial black holes (PBHs) in the asteroid-mass window (10^{17} – 10^{22} g) can account for all of the dark matter without violating any observational constraint, yet are routinely dismissed as fine-tuned. I put that dismissal to the test by applying three complementary fine-tuning measures uniformly across a broad landscape: three non-inflationary PBH production mechanisms, six classes of inflationary PBH models, and seven particle dark matter benchmarks, all evaluated against the same observable target. Three distinct naturalness universality classes emerge, determined entirely by the analytic structure of the abundance map rather than by the nature of the dark matter candidate. Biased-domain-wall PBHs are as natural as off-resonance weakly interacting massive particles and freeze-in particles; early-matter-domination and first-order phase transition PBH mechanisms occupy an intermediate tier alongside coannihilating WIMPs, unified by a structural identity in which the fine-tuning measure equals the logarithm of the ratio of the formation scale to the matter–radiation equality scale; and single-field ultra-slow-roll inflationary collapse is severely tuned for a distinct reason: a double exponential in which the power spectrum amplitude is itself exponentially sensitive to the inflaton potential coefficients, on top of the exponential collapse sensitivity of the abundance map. My main conclusion is that *the claim that PBH dark matter is generically fine-tuned conflates the worst case with a landscape spanning every naturalness tier*. The three-measure protocol also resolves a tension in the recent literature: the Barbieri–Giudice and Iovino–Riotto fine-tuning measures answer complementary questions and are reconciled within the two-layer decomposition developed here.

I. INTRODUCTION

The identity of dark matter remains one of the central open questions of physics. Among the candidates that have attracted sustained interest are weakly interacting massive particles (WIMPs) [1, 2], axions [3–5], feebly interacting (“frozen-in”) particles [6, 7], and asymmetric dark matter [8, 9]. More recently, primordial black holes (PBHs) have re-emerged as a viable dark matter candidate [10, 11], particularly in the asteroid-mass window ($10^{17} \lesssim M_{\text{PBH}}/\text{g} \lesssim 10^{22}$) where Hawking evaporation is negligible, microlensing and disruption constraints are weak, and the PBH fraction $f_{\text{PBH}} \equiv \Omega_{\text{PBH}}/\Omega_{\text{DM}}$ can equal unity [12–14].

A common objection to PBH dark matter is that it requires fine-tuning: in inflationary PBH production the probability of collapse is exponentially sensitive to the primordial curvature power spectrum, which must be arranged to produce the right number density in the right mass window. This argument is frequently made qualitatively, but rarely subjected to the same quantitative scrutiny applied to WIMP dark matter, where a similar exponential sensitivity is implicitly encoded, for instance, in the fabled thermal freeze-out mechanism. The WIMP miracle, the coincidence that a particle with electroweak-scale mass and coupling naturally freezes out with $\Omega h^2 \approx 0.12$, is itself a statement about naturalness, with a well-defined quantitative expression that deserves comparison.

The fine-tuning of dark matter relic abundances has attracted quantitative attention most prominently in the supersymmetric WIMP context. Grothaus, Lindner, and Takanishi [15] applied the Barbieri–Giudice (BG) measure [16], which quantifies how sensitively a physical observable responds to fractional variations of the underlying input parameters, $\Delta \equiv \max_i |\partial \ln \Omega / \partial \ln x_i|$, to neutralino dark matter in the MSSM, showing that direct-detection exclusions preferentially eliminate untuned parameter regions. The most comprehensive MSSM treatment was given by Cabrera *et al.* [17], who studied all major neutralino annihilation mechanisms under a unified BG framework; their finding that funnel and coannihilation scenarios carry the highest combined tuning is fully consistent with the WIMP benchmarks of the present paper. King and Roberts [18] coined the term “supernatural dark matter” for MSSM regions where the relic abundance is achieved with no fine-tuning at all.

For PBH dark matter, the fine-tuning discussion has been framed almost entirely around the inflationary-collapse mechanism. Several studies have quantified the sensitivity of the PBH abundance to the inflaton potential shape in the ultra-slow-roll regime [19, 20]. Kalaja *et al.* [21] showed that the curvature power-spectrum variance σ must lie within a $\sim 7\%$ fractional window to produce all of the dark matter as PBHs under Gaussian statistics, a result broadly consistent with the quantitative fine-tuning estimates of Refs. [19, 20]. Iovino and Riotto [22], by contrast, apply Wilson’s naturalness criterion to single-field inflationary PBH models and conclude that they are not technically unnatural when the measure is formulated symmetrically around the target

* profumo@ucsc.edu

abundance — a conclusion that sits in apparent tension with the sensitivity estimates above. The present paper resolves this tension: the two approaches answer complementary questions and are reconciled within the two-layer decomposition developed here.

Three important gaps remain in the existing literature that this paper fills. First, no prior work has compared PBH and particle dark matter fine-tuning under a *common* measure applied to a *common* observable target ($\Omega_{\text{DM}}h^2 = 0.120$); the two communities have developed parallel but disconnected naturalness vocabularies. Second, the non-inflationary PBH formation mechanisms, including biased domain walls, first-order phase transitions, and early matter domination, have never been analyzed from a quantitative fine-tuning perspective. Third, no systematic comparison of fine-tuning *across* inflationary PBH model classes, from curvaton and spectator-field models through hybrid inflation to single-field ultra-slow-roll, has been presented within a unified, internally consistent fine-tuning measure framework. The present paper addresses all three gaps.

In what follows I apply the BG measure to the parameter spaces of three non-inflationary PBH formation mechanisms, six classes of inflationary PBH model, and seven particle dark matter benchmarks, using an identical protocol for each: $\Delta = 1$ means the abundance scales linearly with the parameter (perfectly natural), $\Delta \gg 1$ means it is exponentially sensitive (fine-tuned).

The principal results of this analysis are:

1. The fine-tuning of any dark matter construction is set by the analytic structure of its abundance map, *not* by whether the dark matter is a particle or a gravitational relic. Three universality classes emerge, and PBH constructions appear in all three.
2. Biased-domain-wall PBHs are as natural as off-resonance WIMPs, freeze-in particles, and post-inflationary axions, and substantially more natural than the coannihilating or resonant-funnel WIMPs that survive current direct-detection limits. Within the PBH paradigm alone the naturalness hierarchy spans more than seven orders of magnitude, from the gravity-fixed domain-wall construction at one extreme to single-field ultra-slow-roll inflationary collapse at the other.
3. Constructions with a single exponential factor in their abundance universally satisfy $\Delta \approx 14\text{--}50$ on the observed dark matter contour, independently of the underlying microscopic physics; the precise value is set by the logarithm of the ratio of the formation temperature to the matter–radiation equality temperature. Coannihilating WIMPs and early-matter-domination PBHs occupy this universality class robustly. First-order phase transition PBHs also fall here within a standard single-exponential approximation for the collapse probability, but a more accurate treatment raises the fine-tuning estimate significantly, and tracing the abundance back

to the underlying scalar potential reveals a further double-exponential structure with $\Delta \sim 10^3\text{--}10^4$. Curvaton inflationary PBH models occupy this intermediate tier only for low reheating temperatures; for standard high-reheating scenarios they are elevated to the most-tuned class, with the reheating temperature setting the boundary between the two. The off-resonance WIMP “miracle”, by contrast, falls in the natural class: when the freeze-out exponential is absorbed into the measured annihilation cross section, the abundance map reduces to a pure power law with $\Delta = 2$.

4. Resonance- or cancellation-dependent constructions (e.g. Higgs-funnel WIMP) and single-field inflationary collapse models are both highly tuned, but for distinct reasons: the former through a narrow annihilation pole, the latter through a double exponential in which the power spectrum amplitude is itself exponentially sensitive to inflaton potential coefficients, on top of an additional exponential sensitivity in the condition for collapse. Multi-field and spectator-field inflationary models avoid the second exponential and fall into the intermediate universality class.

This paper is organized as follows. In Sec. II I define the fine-tuning measures and establish the protocol applied uniformly to all scenarios. In Sec. III I derive the BG measure for three non-inflationary PBH formation mechanisms (Secs. III A–III C), presenting analytic results and parameter-space heatmaps, and then map the framework onto six classes of inflationary PBH model (Sec. III D), including a systematic comparison of their two-layer tuning structure. In Sec. IV I apply the same analysis to seven particle dark matter benchmarks. In Sec. V I compare the full set of results, establish the three universality classes, and prove the structural identity $\Delta \approx \ln(\text{scale ratio})$ that unifies the Class II scenarios; the tier classification is shown to be robust to the choice of fine-tuning convention by presenting Δ_{BG} alongside alternate fine-tuning measures, namely the Strumia–Rattazzi measure Δ_{SR} and the island half-width ϵ . Section VI places the results in broader context, discusses limitations, and identifies directions for follow-up. Conclusions are in Sec. VII.

II. THE BARBIERI–GIUDICE MEASURE APPLIED TO RELIC ABUNDANCES

A. Definition and conventions

Fine-tuning in the context of new physics models was first quantified systematically by Barbieri and Giudice [16], who sought to measure how sensitively the electroweak scale depends on parameters in the supersymmetric spectrum. Given a physical observable \mathcal{O} and a

set of independent input parameters $\{x_i\}$, the Barbieri–Giudice (BG) measure is defined as

$$\Delta \equiv \max_i \Delta_i, \quad \Delta_i \equiv \left| \frac{\partial \ln \mathcal{O}}{\partial \ln x_i} \right|. \quad (1)$$

The interpretation is direct: $\Delta_i = n$ means that a fractional change ϵ in the parameter x_i produces a fractional change $n\epsilon$ in the observable \mathcal{O} . A construction is considered to be “natural” if $\Delta \sim \mathcal{O}(1)$, “moderately tuned” if $\Delta \sim \mathcal{O}(10)$ – $\mathcal{O}(100)$, and “highly tuned” if $\Delta \gg 100$; the requirement $\Delta < 10$ is commonly adopted as a naturalness criterion in the SUSY literature [16, 23], though no sharp threshold carries fundamental significance.

In this paper the observable is the dark matter relic abundance, $\mathcal{O} \equiv \Omega h^2$, evaluated at the benchmark values of the model parameters and compared against the Planck 2018 measurement $\Omega_{\text{DM}} h^2 = 0.1200 \pm 0.0012$ [24]. The sensitivity Δ_i measures how precisely one must specify x_i in order for the predicted abundance to land within, say, a factor of two of $\Omega_{\text{DM}} h^2$: a value $\Delta_i = 35$ means that a $\sim 2\%$ variation in x_i takes the predicted abundance outside this window.¹

The BG measure is a *local* quantity: it characterizes the sensitivity of $\Omega_{\text{DM}} h^2$ to small variations around a chosen benchmark point in parameter space. It should be distinguished from related but inequivalent notions of fine-tuning, including the prior probability of landing on the $\Omega = \Omega_{\text{DM}}$ surface from a random draw of parameters, and the fractional volume of the natural region relative to the prior volume. I return to the distinction between these concepts, and to the specific case of misalignment-axion dark matter where it is particularly consequential, in Sec. V E.

The BG measure is symmetric in the sense that Δ_i takes the same value whether one uses $\mathcal{O} = \Omega h^2$ or $\mathcal{O} = 1/(\Omega h^2)$ as the observable, since $|\partial \ln \mathcal{O} / \partial \ln x_i|$ is unchanged by this inversion. For PBH scenarios, replacing Ωh^2 with f_{PBH} also leaves Δ unchanged, since $f_{\text{PBH}} = \Omega_{\text{PBH}} h^2 / \Omega_{\text{DM}} h^2$ differs only by the constant $\Omega_{\text{DM}} h^2$. It is *not* symmetric under reparametrizations of the parameter space: Δ evaluated with respect to parameters $\{x_i\}$ and $\{y_j = f_j(x)\}$ will generally differ if f_j is nonlinear. The physical content of Δ therefore depends on the identification of fundamental parameters, which I address in Sec. II B.

For reference, a pure power-law abundance map of the form

$$\Omega h^2 \propto \prod_i x_i^{\alpha_i} \quad (2)$$

yields $\Delta_i = |\alpha_i|$ identically everywhere in parameter space. For an abundance set by a single exponential,

$$\Omega h^2 \propto e^{-Ax} \cdot x^\beta, \quad (3)$$

the dominant contribution on the $\Omega h^2 = \Omega_{\text{DM}} h^2$ surface is

$$\Delta_x \approx Ax = \ln \left[\frac{\Omega_{\text{natural}}}{\Omega_{\text{DM}} h^2} \right], \quad (4)$$

where Ω_{natural} is the abundance that would obtain if the exponential were replaced by unity. The full derivative is $\Delta_x = Ax + \beta$, so the approximation $\Delta_x \approx Ax$ overestimates the true value by $-\beta/(Ax)$; for the early-matter-domination benchmark where $\beta = 5$ and $Ax \approx 9$ – 19 , the correction is 20–35% and is the reason the benchmark $\Delta_\sigma = 14.4$ (which includes the prefactor term +5) is larger than the pure-exponential approximation $Ax \approx 9$ – 10 at $\sigma = 0.055$. This result, which is exact when $\beta = 0$ and approximate otherwise, is central to understanding why the three “single-exponential” dark matter constructions discussed in Sec. V yield a universal value $\Delta \approx \ln(T_{\text{form}}/T_{\text{eq}}) \approx 14$ – 50 . Constructions with a Breit–Wigner resonance yield $\Delta \sim M^2/(\Gamma M) \gg \ln(\text{scale ratio})$, a qualitatively distinct and much more severe tuning.

Two complementary measures are computed alongside BG throughout this paper. The *Strumia–Rattazzi* (SR) measure [25] replaces the maximum with a quadrature sum over all parameter directions:

$$\Delta_{\text{SR}} \equiv \sqrt{\sum_i \Delta_i^2} = |\nabla_{\ln x} \ln \Omega h^2|. \quad (5)$$

This equals the magnitude of the log-gradient vector and is sensitive to fine-tuning distributed across multiple parameters simultaneously. For single-parameter scenarios, obviously, $\Delta_{\text{SR}} = \Delta_{\text{BG}}$; for scenarios where all parameters are equally sensitive (e.g. ADM with $\Delta_M = \Delta_R = 1$), $\Delta_{\text{SR}} = \sqrt{n} \Delta_{\text{BG}}$ where n is the number of parameters.

The *island half-width* ϵ in the most sensitive parameter direction provides the most operationally transparent measure of tuning. Rather than asking how steeply the abundance responds to a parameter shift (BG) or summing sensitivities in quadrature (SR), ϵ asks directly: what is the fractional range of the most sensitive parameter that is compatible with the observed dark matter density? Formally,

$$\epsilon \equiv \frac{\Delta x_{\text{sens}}}{x_{\text{sens}}} \Big|_{\text{island}} \approx \frac{\ln 2}{\Delta_{\text{BG}}} \approx \frac{0.693}{\Delta_{\text{BG}}}, \quad (6)$$

where Δx_{sens} is the full fractional width of the natural island in the direction of the most sensitive parameter x_{sens} (the parameter with the largest $|\Delta_i|$), and the approximation holds for a factor-of-2 abundance band. The equivalence $\epsilon \approx \ln 2 / \Delta_{\text{BG}}$ follows directly from the definition of Δ_{BG} : a fractional shift $\delta x/x$ changes $\ln \Omega$ by $\Delta_{\text{BG}} \cdot \delta x/x$,

¹ A fractional shift ϵ in x_i produces a fractional shift $\Delta_i \cdot \epsilon$ in Ωh^2 ; requiring the abundance to remain within a factor of two of the target imposes $\Delta_i \cdot \epsilon \lesssim \ln 2 \approx 0.69$, hence $\epsilon \lesssim 0.69/\Delta_i$. For $\Delta_i = 35$ this gives $\epsilon \lesssim 2\%$; more generally, the fractional precision requirement is $\epsilon \approx 69\%/\Delta_i$.

so the island boundary is reached when $\Delta_{\text{BG}} \cdot \epsilon \approx \ln 2$ (a factor of 2 in Ω). The result is a single percentage that answers the most experimentally concrete version of the naturalness question. To illustrate with two benchmarks defined below: benchmark B3 (coannihilation, Sec. IV A 3, $\Delta = 48$) requires M_{NLSP} to be specified to within $\epsilon = 1.4\%$ to remain in the natural island; benchmark B5 (asymmetric dark matter, Sec. IV C, $\Delta = 1$) tolerates a factor of two in either direction ($\epsilon = 75\%$).

The three measures, BG, SR, and ϵ , are not independent; they are related by construction and probe the same underlying sensitivity from different angles. BG isolates the worst-case direction; SR weights all directions equally; ϵ converts the worst-case sensitivity into an experimentally interpretable precision requirement. In single-parameter scenarios all three agree exactly. In multi-parameter scenarios BG and SR diverge by at most \sqrt{n} (where n is the number of equally sensitive parameters), and ϵ always tracks BG through Eq. (6). The three measures have been applied and compared in the context of supersymmetric dark matter and electroweak naturalness by several authors. Anderson and Castano [26] introduced a normalised variant of BG that accounts for the expected sensitivity of the prior; Strumia [25] proposed the quadrature measure adopted here as Δ_{SR} ; Cabrera, Casas, and Ruiz de Austri [27] applied both BG and Bayesian posterior-volume measures to MSSM dark matter and found them to agree on tier assignments while disagreeing on absolute values by factors of a few.

A separate line of work has addressed fine-tuning measures specifically in the context of inflationary PBH production. Iovino and Riotto [22] identified a pathology of the BG measure when applied to the inflaton potential coefficients $\{c_k\}$: as the target PBH abundance is reduced below the observed dark matter density (i.e. as $f_{\text{PBH}} \rightarrow 0$), the BG measure grows without bound even though a model predicting fewer PBHs is physically less constrained, not more. This occurs because BG measures the local log-slope $|\partial \ln \Omega / \partial \ln c_k|$ without reference to whether Ω is above or below the target; as the exponential suppression is tuned further, the log-slope at any fixed point in parameter space continues to grow. Iovino and Riotto proposed Wilson’s naturalness criterion as a remedy: a parameter is natural if its value is stable under small variations of the UV completion, independent of the abundance it produces. Their measure assigns a value close to unity to essentially all inflationary PBH models, in sharp contrast to the BG values of 10^2 – 10^8 discussed in Sec. III D.

The present paper avoids this pathology by construction, because all three measures (BG, SR, ϵ) are evaluated *on* the $f_{\text{PBH}} = 1$ contour rather than at an arbitrary point in parameter space. The relevant question is not “how sensitive is the model at some generic parameter point?” but “how precisely must each parameter be specified to maintain the observed dark matter density?”; and this question is only meaningful on the $f_{\text{PBH}} = 1$ contour. Evaluated there, the BG measure is

finite and well-defined for all scenarios in the comparison, including inflationary collapse (Eq. 44), and the Iovino–Riotto pathology does not arise. The Wilson question, “does a technically natural UV completion exist for the required parameter values?”, is complementary and physically meaningful, but it answers a different question than the one asked here; Sec. V E returns to this distinction in the context of the prior-probability vs. local-sensitivity debate. To the best of my knowledge, this is the first study to apply all three measures simultaneously to a cross-paradigm comparison that includes PBH formation mechanisms alongside particle dark matter candidates.

B. Choice of fundamental parameters

Because the BG measure is not reparametrization-invariant, the choice of what to call a “fundamental” parameter must be specified and physically motivated. I adopt the following convention throughout this paper: *the fundamental parameters are the independently specified inputs to the UV Lagrangian or to the cosmological initial conditions of the model under consideration*, evaluated at the relevant renormalization scale. For a particle physics model these are the pole masses and Lagrangian coupling constants; in supersymmetric models they are the soft supersymmetry-breaking masses at the mediation scale; for cosmological constructions they are the scales and couplings of the relevant phase transition or symmetry-breaking potential, together with any field-space initial conditions.

This convention has concrete implications for several of the scenarios analyzed below.

Coannihilation.— In the Minimal Supersymmetric Standard Model (MSSM) [28], supersymmetry is broken in a hidden sector and the breaking is transmitted to the visible sector through a mediation mechanism (gravity, gauge, or anomaly mediation) at a high scale M_{med} . The low-energy spectrum is then determined by a set of soft-breaking mass terms in the Lagrangian; crucially, each soft mass is an *independent* parameter at M_{med} , and there is no symmetry or dynamics that correlates them in the absence of additional model structure. For the coannihilation scenario, the two relevant soft masses are M_1 (the bino mass parameter, which sets $M_\chi \equiv |M_1|$ at low energies) and the soft mass $m_{\tilde{f}}$ of the lightest sfermion (stop, stau, or sneutrino), which sets M_{NLSP} (I take the bino as the lightest neutralino and the lightest sfermion as the NLSP; the analysis is qualitatively identical for any spectrum where the two lightest states are nearly degenerate). Coannihilation is relevant when M_{NLSP} and M_χ are nearly degenerate: the NLSP is present in the thermal bath at freeze-out and its annihilation cross section $\langle \sigma v \rangle_{\text{NLSP}}$ contributes to the effective rate that sets the relic density. The contribution is Boltzmann-suppressed by a factor $e^{-x_F \delta}$ (Eq. 52), where $x_F \equiv m_\chi / T_F \approx 25$ is the ratio of the dark matter mass to the freeze-out temperature T_F [29, 30] and $\delta \equiv (M_{\text{NLSP}} - M_\chi) / M_\chi$ is the

fractional mass splitting. Since $T_F \simeq m_\chi/x_F$ is set by the freeze-out condition $\langle\sigma v\rangle n_\chi = H$, and $x_F \approx 20\text{--}30$ for weak-scale dark matter regardless of the exact cross section [29], the exponential suppression can be substantial even for splitting $\delta \sim 0.05\text{--}0.10$.

The fractional mass splitting δ is a *derived* quantity: it is the difference of two Lagrangian parameters, not itself a fundamental input. Taking BG derivatives with respect to δ at fixed M_χ gives

$$\Delta_\delta = x_F \delta + \mathcal{O}(\delta^2) \approx 1\text{--}2 \quad (x_F \delta \ll 1), \quad (7)$$

which substantially underestimates the tuning because the derivative $\partial \ln \Omega / \partial \ln \delta$ vanishes as $\delta \rightarrow 0$ by construction: the coordinate δ crosses zero at the threshold where the two masses are degenerate, and multiplicative log-derivatives are pathologically small near any additive zero. Taking derivatives with respect to the independent Lagrangian parameters (M_χ, M_{NLSP}) at fixed mediation-scale boundary conditions instead yields

$$\Delta_{M_{\text{NLSP}}} = x_F \frac{M_{\text{NLSP}}}{M_\chi} \approx 26\text{--}50, \quad (8)$$

which correctly captures the sensitivity of the Boltzmann-suppressed coannihilation rate to the NLSP pole mass: a 2% shift in M_{NLSP} at fixed M_χ changes δ by 2%, which changes $e^{-x_F \delta}$ by a factor $e^{\pm 0.5} \approx 1.6$, shifting Ωh^2 by $\sim 50\%$ and taking the model outside the natural island. The MSSM coannihilation benchmark B3 uses the parametrization $(M_\chi, M_{\text{NLSP}})$ and yields $\Delta \approx 48$ as a consequence (Eq. 8; see also Sec. IV A 3). This distinction between derived and fundamental parameters has been noted in the electroweak fine-tuning literature [31] but is rarely applied consistently to dark matter relic calculations.

Axion misalignment.— The initial misalignment angle $\theta_i \in [-\pi, \pi]$ is a cosmological initial condition, not a Lagrangian parameter, and is independently specified from f_a , the axion decay constant. It is therefore treated as a separate fundamental input. The important distinction between the BG measure evaluated with respect to θ_i (which gives $\Delta \approx 2$ for $\theta_i \sim 1$) and the prior probability of θ_i being small (which gives a prior tuning $\sim 1/\theta_i$ for a flat distribution) is discussed in Sec. V E.

PBH formation rates.— For the PBH mechanisms analyzed in Sec. III, the fundamental parameters are the scales and couplings appearing in the potential or power spectrum of the underlying model, e.g. the symmetry-breaking scale η and bias energy density V_b for domain walls, the modulus mass m_ϕ and curvature perturbation amplitude σ for early matter domination, and the transition temperature T_* , nucleation rate parameter β/H , and latent-heat parameter α for the FOPT. All three sets of parameters are taken as independent inputs, and BG derivatives are evaluated holding all other parameters fixed.

C. Numerical protocol

All BG derivatives in this paper are evaluated numerically via central finite differences in log-space,

$$\Delta_i \approx \frac{|\ln \Omega(x_i e^h) - \ln \Omega(x_i e^{-h})|}{2h}, \quad h = 10^{-4}. \quad (9)$$

This step size is small enough to suppress second-order corrections to better than 1 part in 10^6 for all smooth abundance functions considered, yet large enough to avoid floating-point cancellation errors. Analytic closed-form expressions for Δ_i are derived independently in Appendix A for all cases where the abundance map is sufficiently simple; numerical and analytic results agree to better than 0.1% in every case.

Parameter-space heatmaps are computed on grids of 400×400 points, logarithmically spaced over the ranges specified in the captions of Figs. 1–5. The color scale is identical across all panels: $\log_{10} \Delta \in [0, 3.5]$ on the `viridis_r` colormap, saturating to dark purple for $\Delta > 3000$. This shared scale is here the principal visual device for comparing fine-tuning across production paradigms.

The *natural island* in each panel is defined as the region of parameter space satisfying

$$0.06 \leq \Omega h^2 \leq 0.24 \quad (10)$$

(i.e. within a factor of two of $\Omega_{\text{DM}} h^2 = 0.120$) together with all constraints listed in Table I. The factor-of-two band is chosen to include representative theoretical uncertainties in the relic-abundance calculation (QCD uncertainties in g_* , perturbative corrections to annihilation cross sections, etc.) without enlarging the island to the point of obscuring the tuning structure. Results are qualitatively insensitive to widening this band to a factor of 3 or narrowing it to 30%. For PBH mechanisms, Ωh^2 is replaced by f_{PBH} (both measure the fraction of dark matter), and the gray dashed contours in the PBH heatmaps show the wider ± 1 dex sidebands $f_{\text{PBH}} \in [0.1, 10]$ as visual guides; all BG derivatives and island half-widths are computed using the factor-of-two band of Eq. (10) applied to f_{PBH} (i.e. $f_{\text{PBH}} \in [0.06/0.12, 0.24/0.12] \equiv [0.5, 2]$), consistent with the particle DM protocol.

TABLE I. Observational constraints applied in this paper and the scenarios to which they are relevant. The stochastic gravitational-wave background from the FOPT itself is not listed here because it constrains the GW signal rather than f_{PBH} directly; this constraint is discussed qualitatively in Sec. III C and Sec. VI A. All PBH abundance constraints are already encoded in the $f_{\text{PBH}} = 1$ requirement and the asteroid-mass window.

Constraint	Value	Applies to
LZ-2024 SI cross section	see [32]	WIMPs
Planck 2018 $\Omega_{\text{DM}} h^2$	0.1200 ± 0.0012	all
PBH asteroid window	$10^{17}\text{--}10^{22}$ g	PBHs
Ly α forest	$M_{\text{DM}} \geq 3$ keV	FIMPs

The direct-detection constraint for WIMPs is implemented via the spin-independent cross section per nucleon,

$$\sigma_{\text{SI}}(M_S, \lambda) = \frac{\lambda^2 f_N^2 m_N^4 \mu_{SN}^2}{\pi M_S^2 M_h^4}, \quad (11)$$

where $f_N = 0.30$ is the nucleon Higgs form factor [33], $m_N = 0.939$ GeV, and $\mu_{SN} = m_N M_S / (m_N + M_S)$ is the singlet–nucleon reduced mass. The LZ 2024 sensitivity curve is approximated by a piecewise power law calibrated to the published limit [32]; this prescription overestimates exclusion at $M_S \lesssim 10$ GeV and underestimates it above ~ 10 TeV, but neither regime contains any of the benchmarks analyzed in this paper. The Lyman- α forest constraint on the freeze-in DM mass ($M_{\text{DM}} \gtrsim 3$ keV for production from a 100-GeV mediator [34, 35]) is implemented as a hard boundary in the FIMP parameter plane.

III. PRIMORDIAL BLACK HOLE DARK MATTER

The formation of PBHs in the asteroid-mass window has been studied in a wide variety of cosmological scenarios. Three non-inflationary mechanisms have received particular attention for their ability to produce $f_{\text{PBH}} \approx 1$ without additional cosmological ingredients: a network of biased domain walls [36], an early matter-dominated era driven by a decaying modulus field [37–40], and a strongly first-order phase transition in a hidden sector [41–43]. The most extensively discussed mechanism in the literature is single-field inflation with an enhanced small-scale power spectrum, generated by an inflection point or ultra-slow-roll phase in the inflaton potential [19, 44, 45]; multi-field and spectator-field variants offer partial relief from the severe inflationary fine-tuning [20]. A distinct inflationary mechanism is the collapse of Higgs field fluctuations near the electroweak vacuum instability scale [46].

For the three non-inflationary mechanisms, I derive the abundance map $f_{\text{PBH}}(\{x_i\})$ from the underlying model parameters, compute Δ analytically, and display the result as a parameter-space heatmap (Secs. III A–III C). Inflationary mechanisms are treated separately in Sec. III D: rather than a single heatmap, I map the BG framework onto six representative inflationary model classes and compare their two-layer tuning structure systematically (Fig. 2). This distinction in treatment reflects a genuine physical difference. For the non-inflationary mechanisms, the fundamental Lagrangian parameters map onto f_{PBH} through a single, well-calibrated chain with no hidden exponentials; the BG measure can therefore be computed precisely and displayed as a smooth landscape. For inflationary models, the mapping from inflaton potential coefficients $\{c_k\}$ to σ to f_{PBH} involves two successive exponentials whose ratio

depends sensitively on the potential shape, leading to estimates that span several orders of magnitude depending on the model class. Furthermore, as noted by Iovino and Riotto [22], applying BG to the potential coefficients off the $f_{\text{PBH}} = 1$ contour raises a subtlety: Δ grows without bound as $f_{\text{PBH}} \rightarrow 0$ even for variations that are physically harmless. The approach adopted throughout this paper, i.e. evaluating all measures *on* the $f_{\text{PBH}} = 1$ contour, avoids this pathology by construction (see Sec. V D).

All four mechanisms produce PBHs whose mass is set by the Hubble horizon at formation,

$$M_{\text{PBH}} \simeq \frac{3.8 M_{\text{Pl}}^3}{T_{\text{form}}^2}, \quad (12)$$

where T_{form} is the temperature at which PBH formation occurs (in natural units $c = k_B = 1$). The asteroid-mass window 10^{17} – 10^{22} g requires formation temperatures $10^4 \lesssim T_{\text{form}}/\text{GeV} \lesssim 10^{6.5}$, shown as gold vertical lines in Fig. 1.

A. Biased domain walls

1. Formation mechanism and abundance map

Consider a scalar field ϕ with a discrete \mathbb{Z}_2 symmetry $\phi \rightarrow -\phi$ that is spontaneously broken when ϕ acquires a vacuum expectation value $\pm\eta$ at a phase transition in the early Universe. The resulting potential has two degenerate minima separated by a potential barrier, and the field takes different values in causally disconnected regions; the boundaries between these regions form a network of two-dimensional topological defects called *domain walls* [47, 48]. Each wall carries a surface energy density (tension) $\sigma_w \sim \eta^3$, where η is the symmetry-breaking scale; the exact coefficient is model-dependent and of order unity, and is absorbed into η throughout.

In the exact \mathbb{Z}_2 limit the two vacua are energetically degenerate and the wall network is cosmologically stable [47], which would lead to domain-wall domination and conflict with cosmology [48]. A small explicit breaking of the \mathbb{Z}_2 symmetry lifts this degeneracy by an energy density V_{bias} between the two vacua. Such a bias arises naturally from Planck-suppressed operators in the scalar potential [49, 50], or can be introduced by hand; in either case it can be parametrized as $V_{\text{bias}} = V_b^4$, where V_b is an effective bias energy scale. The pressure difference V_{bias} across each wall provides a volume force that drives the lower-energy vacuum to expand, causing the network to collapse and annihilate at a temperature T_{ann} set by the competition between this volume pressure and the Hubble friction that resists wall motion [48, 51]:

$$T_{\text{ann}} \simeq \left(\frac{90}{\pi^2 g_*} \right)^{1/4} \sqrt{\frac{c_t M_{\text{Pl}} V_b^4}{\eta^3}}, \quad (13)$$

where $g_* \approx 100$ counts relativistic degrees of freedom and $c_t \approx 0.30$ is a numerical coefficient fitted to the

wall-network simulations of Ref. [51]. At T_{ann} , a fraction $p \approx 10^{-3}$ of horizon-sized wall segments collapse gravitationally into PBHs [36, 51]. This collapse probability is calibrated from simulations of the wall-network dynamics [51]: it reflects the small fraction of Hubble volumes in which the converging wall geometry generates a local overdensity sufficient to exceed the gravitational collapse threshold. The resulting PBH mass and formation fraction are

$$M_{\text{PBH}} \simeq \frac{3.8 M_{\text{Pl}}^3}{T_{\text{ann}}^2} \propto \frac{\eta^3}{V_b^4}, \quad (14)$$

$$\beta_{\text{PBH}} \equiv \left. \frac{\rho_{\text{PBH}}}{\rho_{\text{tot}}} \right|_{T_{\text{ann}}} \simeq \frac{p V_b^4}{\frac{\pi^2}{30} g_* T_{\text{ann}}^4}. \quad (15)$$

The present-day PBH dark matter fraction is obtained by redshifting β_{PBH} from T_{ann} to matter–radiation equality at $T_{\text{eq}} = 0.75$ eV:

$$f_{\text{PBH}} \simeq \beta_{\text{PBH}} \frac{T_{\text{ann}}}{0.84 T_{\text{eq}}}, \quad (16)$$

where the factor 0.84 accounts for the change in g_* between T_{ann} and T_{eq} [12]. Substituting Eqs. (13)–(15) into Eq. (16) and collecting powers, one finds

$$\boxed{f_{\text{PBH}} \propto \frac{\eta^{9/2}}{V_b^2}}, \quad (17)$$

a *pure power-law* in the two fundamental parameters (η, V_b) with no exponential factor. This is the central structural result for this construction: the abundance map is a monomial, and the BG fine-tuning measure is therefore constant across the entire parameter space.

The asteroid-mass window 10^{17} – 10^{22} g requires, via Eq. (14),

$$T_{\text{ann}} \in [10^5, 3 \times 10^7] \text{ GeV} \approx [10^{4.9}, 10^{7.5}] \text{ GeV}. \quad (18)$$

These boundaries follow directly from inverting $M_{\text{PBH}} = 3.8 M_{\text{Pl}}^3/T_{\text{ann}}^2$: at $T_{\text{ann}} = 10^5$ GeV one obtains $M_{\text{PBH}} \approx 10^{22}$ g (upper edge), and at $T_{\text{ann}} = 3 \times 10^7$ GeV one obtains $M_{\text{PBH}} \approx 10^{17}$ g (lower edge).

The benchmark $\eta = 2.4 \times 10^6$ GeV, $V_b = 2$ TeV is chosen as the simultaneous intersection of three conditions. First, $f_{\text{PBH}} \approx 1$, so PBHs account for all of the dark matter. Second, $T_{\text{ann}} \approx 5 \times 10^5$ GeV, placing $M_{\text{PBH}} \approx 4 \times 10^{20}$ g well within the asteroid window. Third, $V_b = 2$ TeV is within 20% of the gravity-induced bias value $V_b^{\text{grav}} = (\eta^5/M_{\text{Pl}})^{1/4} \approx 2.4$ TeV at this η , so the bias is naturally generated by Planck-suppressed operators of the form ϕ^5/M_{Pl} evaluated at $\phi = \eta$, i.e. $V_{\text{bias}} \sim \eta^5/M_{\text{Pl}}$ [49, 50], without introducing a new free scale.

$$V_b^{\text{grav}}(\eta) \equiv (\eta^5/M_{\text{Pl}})^{1/4}. \quad (19)$$

These three conditions together identify $\eta \approx 2.4 \times 10^6$ GeV as a theoretically motivated “sweet spot”: a

single symmetry-breaking scale that simultaneously accounts for all of the dark matter, targets the asteroid-mass window, and requires no bias scale beyond what quantum gravity generates automatically. A particularly clean sub-class is the “gravity-induced bias” scenario in which one sets $V_b = V_b^{\text{grav}}$ exactly, reducing the construction to a single-parameter family parametrized by η alone.

2. Analytic fine-tuning structure

From Eq. (17) the BG sensitivities follow immediately by log-differentiation:

$$\Delta_\eta = \left| \frac{\partial \ln f_{\text{PBH}}}{\partial \ln \eta} \right| = \frac{9}{2}, \quad \Delta_{V_b} = \left| \frac{\partial \ln f_{\text{PBH}}}{\partial \ln V_b} \right| = 2. \quad (20)$$

Both are *exact constants*, independent of the values of η and V_b and of the location in parameter space. The overall measure is

$$\Delta_{\text{DW}} = \max(\Delta_\eta, \Delta_{V_b}) = \frac{9}{2} \quad \forall (\eta, V_b). \quad (21)$$

For the gravity-induced-bias sub-case, substituting $V_b \propto \eta^{5/4} M_{\text{Pl}}^{-1/4}$ into Eq. (17) gives $f_{\text{PBH}} \propto M_{\text{Pl}}^{1/2} \eta^2$, so the single-parameter measure reduces to $\Delta_\eta^{(\text{grav})} = 2$, the minimum value compatible with a non-trivial dependence on any dimensionful scale.

As shown below, this result places biased-domain-wall PBHs in the same naturalness tier as off-resonance heavy WIMPs and freeze-in particles (all with $\Delta \approx 2$), and substantially below the coannihilation and FOPT constructions discussed below. The quantitative answer to the title question is clear for this mechanism: biased-domain-wall PBHs are *not* fine-tuned by any reasonable standard.

3. Parameter-space heatmap

Figure 1(a) shows $\log_{10} \Delta$ in the $(\log_{10} \eta, \log_{10} V_b)$ plane. The entire panel is uniformly pale yellow, the lowest color on the shared scale, reflecting the analytic result $\Delta = 9/2$ everywhere, a direct consequence of the pure power-law structure $f_{\text{PBH}} \propto \eta^{9/2}/V_b^2$ (Eq. 17). The thick black contour marks $f_{\text{PBH}} = 1$; gray dashed contours at $f_{\text{PBH}} = 0.1$ and 10 define the ± 1 dex sidebands that bound the natural island (green hatching). The two gold-orange lines show the asteroid-mass boundaries $M_{\text{PBH}} = 10^{17}$ g and 10^{22} g; these are nearly parallel to the $f_{\text{PBH}} = 1$ contour because both f_{PBH} and M_{PBH} are controlled by the same parameter combination η^3/V_b^4 (Eqs. 14 and 17). The magenta dash-dotted line shows the gravity-induced-bias locus $V_b = (\eta^5/M_{\text{Pl}})^{1/4}$ (Eq. 19), along which the bias is generated by Planck-suppressed operators rather than freely tuned. This locus

passes through the natural island and through the benchmark point ($\eta = 2.4 \times 10^6$ GeV, $V_b = 2$ TeV; gold star), confirming that the Planck-suppressed scenario naturally populates the asteroid-mass window without any additional parameter adjustment.

B. Early matter domination

1. Formation mechanism and abundance map

A natural setting for an early matter-dominated era is provided by string-theoretic moduli: scalar fields ϕ with only gravitational-strength couplings to ordinary matter that are ubiquitous in compactifications of extra dimensions [52, 53]. More broadly, any scalar field that begins to oscillate coherently in the early Universe when the Hubble rate drops below its mass, $H \sim m_\phi$, behaves as a pressureless fluid and temporarily dominates the energy density before decaying [53]. Such a field decays with a rate set by dimensional analysis for a gravitationally coupled particle, $\Gamma_\phi \sim c_\phi m_\phi^3/M_{\text{Pl}}^2$, where $c_\phi \sim 10^{-3}$ encodes loop and phase-space suppression factors [52]. When H drops to Γ_ϕ , the field decays and reheats the Universe to a temperature [37, 38, 53]

$$T_{\text{rh}} \simeq 0.55 \left(\frac{c_\phi m_\phi^3}{M_{\text{Pl}}} \right)^{1/2}. \quad (22)$$

The period of matter domination preceding reheating alters cosmological perturbation growth in a way that is crucial for PBH production. In a radiation-dominated background, sub-Hubble density perturbations oscillate and decay; in a matter-dominated background, the same perturbations grow as $\delta\rho/\rho \propto a$ (where a is the scale factor), and sufficiently large fluctuations can overcome pressure support and collapse gravitationally before reheating occurs [37, 54]. The relevant perturbations are curvature perturbations inherited from inflation, characterized by their root-mean-square amplitude σ on the scale that re-enters the Hubble horizon during the matter-dominated era. The fraction of the energy density that collapses into PBHs depends sensitively on how many Hubble patches contain a perturbation large enough to collapse; this collapse criterion in a pressureless medium was derived analytically and verified numerically by Harada, Yoo, Kohri, and Nakama (HYKN) [55], who found

$$\beta_{\text{AM}}(\sigma) \simeq 4.6 \times 10^{-6} \sigma^5 \exp\left(-\frac{0.147}{\sigma^{4/3}}\right). \quad (23)$$

Here β_{AM} is the mass fraction of the Universe that collapses into PBHs at the time of formation. The σ^5 prefactor reflects the five-dimensional phase-space volume for a fluctuation to exceed the collapse threshold in a pressureless fluid (compared to the exponential-only Press–Schechter form in radiation domination [56]), while

the exponential encodes the probability tail of a Gaussian distribution above the threshold density contrast $\delta_c \simeq 0.05$ appropriate to matter domination [55]. The two contributions are equal at $\sigma \approx 0.050$, close to the natural-island benchmark, so neither can be neglected.

The PBH mass equals the Hubble-horizon mass at the time of collapse, which for this mechanism occurs just before reheating:

$$M_{\text{PBH}} \simeq \frac{3.8 M_{\text{Pl}}^3}{T_{\text{rh}}^2} \propto m_\phi^{-3}, \quad (24)$$

where the proportionality uses Eq. (22). The asteroid-mass window $M_{\text{PBH}} \in [10^{17}, 10^{22}]$ g therefore maps to a modulus-mass range $m_\phi \in [4 \times 10^{10}, 2 \times 10^{12}]$ GeV, as shown by the gold vertical lines in Fig. 1(b). The present-day dark matter fraction is obtained by redshifting β_{AM} from the formation epoch to matter–radiation equality at $T_{\text{eq}} = 0.75$ eV:

$$f_{\text{PBH}}(m_\phi, \sigma) \simeq \beta_{\text{AM}}(\sigma) \frac{T_{\text{rh}}(m_\phi)}{0.84 T_{\text{eq}}}. \quad (25)$$

The factor 0.84 accounts for the change in relativistic degrees of freedom g_* between T_{rh} and T_{eq} [12]. The dependence on m_ϕ enters solely through T_{rh} and is a pure power law, $f_{\text{PBH}} \propto m_\phi^{3/2} \beta_{\text{AM}}(\sigma)$, while the σ dependence through Eq. (23) is non-trivial, containing both the polynomial prefactor and the exponential that will give rise to the characteristic Class II fine-tuning structure analyzed in Sec. III B 2.

2. Analytic fine-tuning structure

Differentiating Eq. (25) with respect to $\ln m_\phi$ and $\ln \sigma$:

$$\Delta_{m_\phi} = \left| \frac{\partial \ln f_{\text{PBH}}}{\partial \ln m_\phi} \right| = \frac{3}{2}, \quad (26)$$

$$\Delta_\sigma = \left| \frac{\partial \ln f_{\text{PBH}}}{\partial \ln \sigma} \right| = 5 + \frac{0.196}{\sigma^{4/3}}. \quad (27)$$

The modulus-mass sensitivity $\Delta_{m_\phi} = 3/2$ is a constant, reflecting the simple power-law connection $T_{\text{rh}} \propto m_\phi^{3/2}$. The curvature-variance sensitivity Δ_σ is dominated by the exponential factor in β_{AM} at small σ and by the prefactor at large σ ; the two contributions are equal at $\sigma^{4/3} = 0.196/5 \approx 0.039$, i.e. $\sigma \approx 0.050$. Since the natural island (defined by $f_{\text{PBH}} \approx 1$ in the asteroid window) requires $\sigma \in [0.037, 0.071]$ at the benchmark $m_\phi = 9 \times 10^{10}$ GeV, the relevant range is

$$\Delta_\sigma^{(\text{island})} \in [12, 21], \quad (28)$$

with a benchmark value $\Delta_\sigma = 14.4$ at $\sigma = 0.055$.

The benchmark value $\sigma = 0.055$ is chosen because it sits near $\sigma \approx 0.050$ where the exponential and polynomial terms in Eq. (23) contribute equally ($0.147/\sigma^{4/3} \approx 5$),

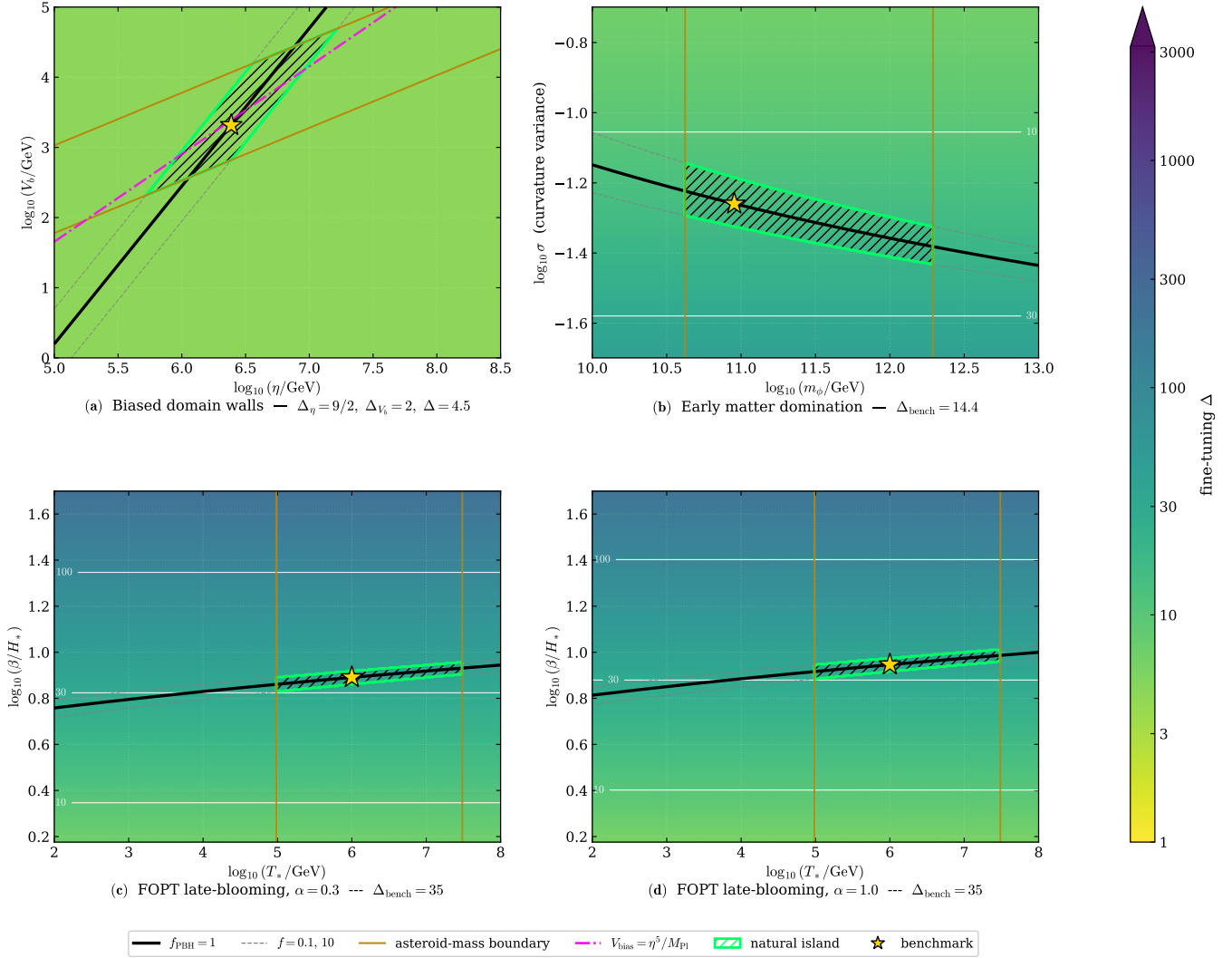


FIG. 1. Fine-tuning of the three PBH dark-matter formation mechanisms analyzed in this paper. *Background color*: $\log_{10} \Delta$ on a shared scale $\Delta \in [1, 3000]$ (pale yellow = natural, dark purple = highly tuned; see colorbar at right). *Thick black contour*: $f_{\text{PBH}} = 1$. *Gray dashed contours*: $f_{\text{PBH}} = 0.1$ and 10 (± 1 dex sidebands). *Gold/orange vertical lines*: asteroid-mass boundaries $M_{\text{PBH}} = 10^{17}$ g and 10^{22} g. *Green hatching*: natural island, defined as $0.1 \leq f_{\text{PBH}} \leq 10$ within the asteroid-mass window and satisfying all observational constraints. *Gold star*: benchmark point. **(a)** Biased domain walls in the (η, V_b) plane (\log_{10} axes; η = symmetry-breaking scale, V_b = bias energy scale; Eq. 17). The magenta dash-dotted line is the gravity-induced-bias locus $V_b = (\eta^5/M_{\text{Pl}})^{1/4}$. The panel is uniformly pale yellow, reflecting $\Delta = 9/2$ everywhere (Eq. 21). Benchmark: $\eta = 2.4 \times 10^6$ GeV, $V_b = 2$ TeV. **(b)** Early matter domination in the (m_ϕ, σ) plane (m_ϕ = modulus mass, σ = curvature perturbation variance; Eqs. 23–25). The color gradient from yellow-green to teal reflects the rising $\Delta_\sigma = 5 + 0.196/\sigma^{4/3}$ (Eq. 27) as σ decreases. The asteroid-mass boundaries correspond to $m_\phi \in [4 \times 10^{10}, 2 \times 10^{12}]$ GeV (Eq. 24). Benchmark: $m_\phi = 9 \times 10^{10}$ GeV, $\sigma = 0.055$, giving $M_{\text{PBH}} \approx 10^{21}$ g; $\Delta = 14.4$. **(c, d)** FOPT late-blooming in the $(T_*, \beta/H_*)$ plane for $\alpha = 0.3$ (panel c) and $\alpha = 1.0$ (panel d). The two panels are nearly identical, confirming the α -independence of the key identity Eq. (37). The $f_{\text{PBH}} = 1$ contour coincides with the $\Delta = 30$ contour throughout, making $\Delta_{\beta/H} = \ln(T_*/0.84T_{\text{eq}}) \approx 35$ directly visible. Benchmark: $T_* = 10^6$ GeV, $\beta/H_* = 7.78$ ($\alpha = 0.3$) and 8.84 ($\alpha = 1.0$); both at $\Delta = 35$.

making it a physically representative point at which neither term dominates and the value $\Delta_\sigma = 14.4$ is typical of the natural island. It corresponds to a curvature power spectrum amplitude $\mathcal{P}_{\mathcal{R}}(k_{\text{form}}) \approx \sigma^2 \approx 3 \times 10^{-3}$ on the asteroid-mass scale, a factor of $\sim 10^6$ above the CMB amplitude. Values $\sigma \lesssim 0.04$ exponentially suppress β_{AM} and require an unrealistically high m_ϕ to compensate;

values $\sigma \gtrsim 0.10$ overproduce PBHs and push m_ϕ below the asteroid-mass lower boundary. The natural island in σ is therefore bounded from below by the exponential tail of the HYKN formula and from above by the asteroid-mass constraint, precisely the two-sided confinement that makes $\Delta_\sigma \approx 14$ a robust result within this window.

The overall measure $\Delta_{\text{MD}} = \max(3/2, \Delta_\sigma) = \Delta_\sigma$

across the entire natural island, placing this construction firmly in the intermediate “single-exponential” class despite the σ^5 prefactor moderating the growth rate.

The value $\sigma \approx 0.055$ required for $f_{\text{PBH}} = 1$ in the asteroid-mass window corresponds to a primordial curvature power spectrum amplitude $\mathcal{P}_{\mathcal{R}} \approx \sigma^2 \approx 3 \times 10^{-3}$ at the formation scale k_{form} , some seven orders of magnitude above the CMB amplitude $\mathcal{P}_{\mathcal{R}}^{\text{CMB}} \approx 2 \times 10^{-9}$. Generating such an enhancement without disturbing CMB scales requires additional model ingredients — a spectator field, a feature in the inflationary potential, or resonant particle production [44, 45, 57] — whose model-building cost I fold into the tuning through the single effective parameter σ , rather than through the inflaton potential shape. This treatment is appropriate for the early-matter-domination mechanism, where σ is a free parameter of the cosmological initial conditions; for inflationary models, the additional cost of generating the required σ from the inflaton potential is treated separately in Sec. III D as a second layer of tuning.

3. Parameter-space heatmap

Figure 1(b) shows $\log_{10} \Delta$ in the (m_ϕ, σ) plane, with the x-axis spanning the modulus masses relevant for asteroid-mass PBH production, $m_\phi \in [10^{10}, 10^{13}]$ GeV. In contrast to the domain-wall panel, a clear color gradient is visible: the panel darkens from yellow-green at large σ (low tuning, $\Delta \approx 7$) toward teal at small σ (higher tuning, $\Delta \approx 20$), reflecting the rising exponential sensitivity $\Delta_\sigma = 5 + 0.196/\sigma^{4/3}$ (Eq. 27) as the Gaussian tail that controls collapse is pushed further into the rare-event regime. The $\Delta = 10$ and $\Delta = 30$ white contours bracket the natural island, confirming the analytic range $\Delta_\sigma \in [12, 21]$ of Eq. (28). The vertical gold lines mark the asteroid-mass boundaries $M_{\text{PBH}} = 10^{17}$ g and 10^{22} g, which correspond via Eq. (24) to $m_\phi \in [4 \times 10^{10}, 2 \times 10^{12}]$ GeV; the constraint is purely horizontal because M_{PBH} depends on m_ϕ alone and not on σ . The natural island (green hatching) is a diagonal strip running along the $f_{\text{PBH}} = 1$ contour. Its tilt reflects the interplay between the two parameters: increasing σ raises β_{AM} through the HYKN formula, which would overproduce PBHs unless compensated by a larger m_ϕ (hence higher T_{rh} and stronger dilution from formation to equality). The benchmark $m_\phi = 9 \times 10^{10}$ GeV, $\sigma = 0.055$ (gold star) lies within the asteroid-mass natural island at $M_{\text{PBH}} \approx 10^{21}$ g and $\Delta = 14.4$.

A guaranteed observational consequence of the enhanced curvature power spectrum $\mathcal{P}_{\mathcal{R}}(k_{\text{form}}) \approx \sigma^2 \approx 3 \times 10^{-3}$ required for asteroid-mass PBH production is a stochastic gravitational-wave background (SGWB) sourced at second order in perturbation theory by the same scalar perturbations [58, 59]. The peak frequency of this scalar-induced GW (SIGW) background is set by the formation temperature, $f_{\text{peak}} \approx 3 \times 10^{-3}$ Hz ($T_{\text{form}}/10^6$ GeV), placing it in the mHz–Hz band

for the asteroid-mass window, precisely the target range of LISA and DECIGO [60]. The SIGW amplitude scales as $\Omega_{\text{GW}} h^2 \sim \mathcal{P}_{\mathcal{R}}^2 \sim 10^{-6}–10^{-4}$ at the benchmark $\sigma = 0.055$, which is within the projected LISA sensitivity for transition temperatures $T_{\text{form}} \gtrsim 10^5$ GeV [60]. Current bounds from Planck on the effective number of relativistic species, $\Delta N_{\text{eff}} \lesssim 0.3$, translate into an integrated upper bound $\int \Omega_{\text{GW}} d \ln f \lesssim 5 \times 10^{-6}$ that does not constrain the benchmark point but begins to disfavor $\sigma \gtrsim 0.15$ across the full asteroid-mass range [60]. The SIGW signal is therefore a robust and near-future testable prediction of the early-matter-domination PBH mechanism, and constitutes an independent observational channel complementary to microlensing searches.

C. First-order phase transition

1. Formation mechanism and abundance map

A first-order phase transition (FOPT) occurs when a field Φ in a hidden sector tunnels from a metastable false vacuum to the true vacuum of its potential, rather than rolling continuously as in a second-order transition. The transition proceeds by the stochastic nucleation of bubbles of the true vacuum within the false-vacuum background; these bubbles expand at close to the speed of light, collide, and eventually convert the entire Universe to the new phase [61, 62]. I consider a FOPT occurring at a temperature T_* in a hidden sector that is thermally coupled to the Standard Model plasma, so that the transition temperature is a physical parameter that sets the PBH mass through the Hubble horizon at that time.

Two dimensionless parameters characterize the transition completely for the purposes of PBH production. The *transition strength* α is the ratio of the latent heat released during nucleation to the ambient radiation energy density,

$$\alpha \equiv \frac{\Delta V - T_* \partial \Delta V / \partial T_*}{\rho_{\text{rad}}(T_*)}, \quad (29)$$

where ΔV is the difference in free-energy density between the two phases [63]. A small α corresponds to a weak transition in which latent heat is a minor perturbation to the radiation bath; a large α corresponds to a strong, potentially runaway transition that can dramatically reheat the Universe. The *transition rate parameter* β/H_* measures how rapidly the nucleation rate grows relative to the Hubble rate at T_* ; equivalently, H_*/β is the duration of the transition in Hubble units, with small β/H_* corresponding to a slow, prolonged transition and large β/H_* to an almost instantaneous one.

Regions of the false vacuum that are not reached by any bubble wall before the transition ends are compressed by the surrounding expanding walls. If the resulting overdensity exceeds the gravitational collapse threshold, these regions form PBHs [41–43, 64–66]. The probability

that a given Hubble-volume region remains in the false vacuum until the end of the transition is determined by the nucleation statistics; for an exponentially growing nucleation rate $\Gamma \propto e^{\beta t}$ (the standard approximation [60]), the fraction of the Universe that collapses into PBHs is

$$\beta_{\text{PBH}} = \exp\left[-S(\alpha) \frac{\beta}{H_*}\right], \quad (30)$$

where $S(\alpha)$ encodes how efficiently the transition converts false-vacuum regions into PBHs as a function of its strength². $S(\alpha)$ is model-dependent, but can be computed analytically for a given scalar potential; for the hidden-sector benchmark model of Ref. [43] the result is well approximated by the interpolating formula

$$S(\alpha) \simeq 5.5 - \frac{2\alpha}{\alpha + 0.3}, \quad (31)$$

which decreases monotonically from $S(0) = 5.5$ in the weak-transition limit (where the radiation bath is barely disturbed and the false-vacuum survival probability is relatively insensitive to α) to $S(\infty) = 3.5$ in the ultra-strong limit (where the latent heat dominates and bubble walls run away [60, 63]). The coefficients in Eq. (31) are specific to that model; different bubble-wall velocities, plasma couplings, or reheating dynamics would yield different values. As I show below in Eq. (37), however, the key fine-tuning identity $S(\alpha)\beta/H_*|_{f_{\text{PBH}}=1} = \ln[T_*/(0.84 T_{\text{eq}})]$ follows from setting $f_{\text{PBH}} = 1$ in Eq. (32) and holds for *any* monotone $S(\alpha)$; the fine-tuning result is therefore model-independent even though $S(\alpha)$ is not. The PBH mass is set by the Hubble horizon at T_* , $M_{\text{PBH}} \simeq 3.8 M_{\text{Pl}}^3/T_*^2$, and the present-day dark matter fraction is

$$f_{\text{PBH}}(T_*, \beta/H_*, \alpha) = \exp\left[-S(\alpha) \frac{\beta}{H_*}\right] \cdot \frac{T_*}{0.84 T_{\text{eq}}}. \quad (32)$$

The parameter space of interest for this mechanism is defined entirely by the requirement $f_{\text{PBH}} \approx 1$ within the asteroid-mass window, which fixes $\beta/H_* \sim 5\text{--}15$

at the benchmark temperatures $T_* \sim 10^5\text{--}10^7$ GeV. It is a non-trivial consequence that this same range of β/H_* lies within the sensitivity reach of LISA and next-generation ground-based gravitational-wave detectors for the stochastic background produced by the transition itself [60, 68]: FOPT-PBH dark matter is therefore simultaneously a target of gravitational-wave observatories and microlensing surveys, not because the two observations are by construction linked, but because both probe the same underlying parameter β/H_* .

2. Analytic fine-tuning structure

Differentiating Eq. (32):

$$\Delta_{T_*} = \left| \frac{\partial \ln f_{\text{PBH}}}{\partial \ln T_*} \right| = 1, \quad (33)$$

$$\Delta_{\beta/H} = \left| \frac{\partial \ln f_{\text{PBH}}}{\partial \ln(\beta/H_*)} \right| = S(\alpha) \frac{\beta}{H_*}, \quad (34)$$

$$\Delta_{\alpha} = \left| \frac{\partial \ln f_{\text{PBH}}}{\partial \ln \alpha} \right| = \frac{\beta}{H_*} \cdot \frac{0.6\alpha}{(\alpha + 0.3)^2}. \quad (35)$$

The temperature sensitivity $\Delta_{T_*} = 1$ is a constant, since $f_{\text{PBH}} \propto T_*$ through the dilution factor alone. The dominant contribution is $\Delta_{\beta/H}$, which grows linearly with β/H_* .

The key result emerges upon imposing the condition $f_{\text{PBH}} = 1$, that is, solving Eq. (32) for β/H_* at fixed T_* and α :

$$S(\alpha) \frac{\beta}{H_*} \Big|_{f_{\text{PBH}}=1} = \ln \left[\frac{T_*}{0.84 T_{\text{eq}}} \right]. \quad (36)$$

Substituting Eq. (36) into Eq. (34),

$$\Delta_{\beta/H} \Big|_{f_{\text{PBH}}=1} = \ln \left[\frac{T_*}{0.84 T_{\text{eq}}} \right] \approx 30\text{--}37 \quad (37)$$

for $T_* \in [10^4, 10^{6.5}]$ GeV (the asteroid-mass formation window). This result is exact for any α and any T_* in the relevant range, and is independent of the specific value of $S(\alpha)$: *the fine-tuning of FOPT-PBH dark matter is determined entirely by the logarithm of the dilution ratio from formation to equality, and is insensitive to the strength or dynamics of the phase transition.* The nucleation-rate parameter β/H_* must be tuned to $\sim 3\%$ precision to land on the $f_{\text{PBH}} = 1$ contour.

Equation (37) is the gravitational-sector analog of the thermal-freeze-out tuning $\Delta \approx x_F \simeq 25$ for standard WIMPs (see Sec. IV A 3); both express the cost of exponentially suppressing a natural formation rate to match the observed dark matter density. This structural identity is the central observation of Sec. V.

² Equation (30) is the standard phenomenological approximation in which the false-vacuum survival fraction is written as a single exponential in the nucleation-rate parameter β/H_* , treating β/H_* as a fundamental input. A more complete analysis of the collapse probability in the supercooled limit, tracking the full past-light-cone percolation integral, shows that $\mathcal{P}_{\text{coll}}$ is super-exponential in β/H [36]: the BG derivative evaluated from that formula at the benchmark $\beta/H_* \approx 8$ gives $\Delta_{\beta/H} \approx 265$ rather than ≈ 35 , placing FOPT-PBH in Class III even at the phenomenological level (Sec. VIB, Eq. 72). At a deeper level, tracing f_{PBH} back to the microphysical scalar potential through the Euclidean action $S_3(T_p)/T_p$ yields a double-exponential (“super-exponential”) structure, $f_{\text{PBH}} \simeq M \exp(-Q \exp(-S_3(T_p)/T_p))$, with $Q \sim 10^{77}$ [67], giving $\Delta \sim 10^3\text{--}10^4$. The fine-tuning analysis in Eqs. (33)–(37) uses the single-exponential approximation and therefore gives a *lower bound* on the true BG measure; see Sec. VIB for the full assessment.

3. Parameter-space heatmap

Figures 1(c) and 1(d) show $\log_{10} \Delta$ in the $(T_*, \beta/H_*)$ plane for $\alpha = 0.3$ (moderately strong transition, $S(0.3) \approx 4.1$) and $\alpha = 1.0$ (strong transition, $S(1.0) \approx 4.0$), respectively. Both panels share the same qualitative color structure: a uniform teal background corresponding to $\Delta \approx 35$ throughout most of the plane, with darker (more tuned) shading at large β/H_* where the exponential suppression of β_{PBH} becomes more severe, and lighter shading at small β/H_* where PBH overproduction would occur. The $\Delta = 30$ white contour runs nearly horizontally across each panel and coincides almost exactly with the $f_{\text{PBH}} = 1$ contour (thick black), making the key identity $\Delta_{\beta/H} = \ln[T_*/(0.84 T_{\text{eq}})] \approx 35$ (Eq. 37) directly visible as a geometric feature of both plots.

The two panels are strikingly similar despite the factor-of-three difference in α : the $f_{\text{PBH}} = 1$ contour shifts upward by only $\Delta \log_{10}(\beta/H_*) \approx 0.07$ between panels (c) and (d), corresponding to $\beta/H_* = 7.78$ vs. 8.84 at the benchmark temperature $T_* = 10^6$ GeV. This near-degeneracy is the visual confirmation of the α -independence established analytically in Eq. (37): since $S(0.3) \approx 4.1 \approx S(1.0) \approx 4.0$, the required value of β/H_* to achieve $f_{\text{PBH}} = 1$ at fixed T_* changes by only $\sim 14\%$, and the fine-tuning $\Delta = 35$ is identical in both cases.

The natural island (green hatching, $0.1 \leq f_{\text{PBH}} \leq 10$ within the asteroid-mass window) appears in both panels as a narrow, nearly horizontal strip at $\log_{10}(\beta/H_*) \approx 0.9$. Its horizontal extent spans the full asteroid-mass temperature range $\log_{10}(T_*/\text{GeV}) \in [4.7, 7.6]$ (bounded by the vertical gold lines), a factor of ~ 800 in T_* . This wide coverage means that a single value of β/H_* , independently of the transition temperature, places the mechanism in the asteroid-mass window; the PBH mass is selected by T_* (with $\Delta_{T_*} = 1$, a one-parameter freedom) while the abundance is controlled by β/H_* (with $\Delta_{\beta/H} \approx 35$ within the single-exponential approximation used here, and ≈ 265 from the more accurate collapse formula of Ref. [36]; see Sec. VIB). The color scale in both panels therefore represents a *lower bound* on the true BG measure. The benchmark $T_* = 10^6$ GeV is marked by gold stars in both panels; the required nucleation rate is $\beta/H_* = 7.78$ in panel (c) and 8.84 in panel (d), and both stars lie precisely on the $f_{\text{PBH}} = 1$ contour at $\Delta = 35$.

D. Inflationary collapse: a two-layer structure

The three mechanisms analyzed above (biased domain walls, early matter domination, and first-order phase transitions) do not exhaust the list of PBH formation channels. The most extensively studied mechanism in the literature is the collapse of large-amplitude curvature perturbations generated during single-field inflation. In the standard picture, inflation produces a nearly scale-invariant power spectrum of curvature perturbations $\mathcal{P}_{\mathcal{R}}(k)$ whose amplitude on CMB scales is $\mathcal{P}_{\mathcal{R}} \approx 2 \times 10^{-9}$.

PBH formation requires $\mathcal{P}_{\mathcal{R}} \sim 10^{-2}$ – 10^{-3} on sub-CMB scales corresponding to the asteroid-mass Hubble horizon, an enhancement of $\mathcal{O}(10^6$ – $10^7)$ relative to the CMB amplitude [44, 45]. Such an enhancement is typically achieved through a feature in the single-field inflaton potential, most commonly an inflection point or a phase of ultra-slow-roll (USR), during which the inflaton velocity is briefly reduced to near zero, allowing quantum fluctuations to grow to large amplitude on the scales that cross the Hubble horizon at that moment [19, 45]. The curvature perturbation variance σ that enters the collapse formula (Eq. 23) is related to the power spectrum by $\sigma^2 \approx \int_{k_{\text{form}}} \mathcal{P}_{\mathcal{R}}(k) W^2(k) d \ln k$, where $W(k)$ is a window function on the formation scale k_{form} ; for a narrow peak at k_{form} , $\sigma \approx \mathcal{P}_{\mathcal{R}}^{1/2}(k_{\text{form}})$, though more generally σ depends on the full spectral shape through the window-function integral. Since the present analysis treats σ as a free effective parameter, the precise form of this relation does not affect the fine-tuning conclusions; the model-building cost of generating the required large σ from the inflaton potential is instead captured by the Layer 2 analysis below.

I do not analyze inflationary PBH production in the same detail as the previous three mechanisms, partly because its fine-tuning has already received dedicated attention in the literature [19–22], and partly for the methodological reason explained in the opening of this section. Instead, I develop a two-layer decomposition of the inflationary fine-tuning: a first layer capturing the sensitivity of the PBH abundance to the curvature power spectrum amplitude σ , whose value depends critically on the reheating history, and a second layer capturing the additional sensitivity of σ to the inflaton potential coefficients. This decomposition places the six inflationary model classes into a systematic hierarchy and clarifies why their fine-tuning spans more than seven orders of magnitude.

The inflationary mechanism involves two successive parameter-to-observable maps, each contributing independently to the total fine-tuning.

Layer 1: $\sigma \rightarrow f_{\text{PBH}}$. The form of the collapse fraction $\beta(\sigma)$ depends on the equation of state at the epoch when the enhanced perturbations re-enter the Hubble horizon, and this distinction is physically important for the fine-tuning estimate.

For the early-matter-domination mechanism of Sec. IIIB, collapse occurs during a pressureless era and is described by the HYKN formula (23) with threshold $\delta_c \approx 0.05$, giving $\Delta_{\sigma}^{(\text{MD})} \approx 14$ (Eq. 27). I refer to this as the Layer 1 floor for the MD case: it sets a minimum fine-tuning cost independent of whatever mechanism generates the required σ .

For inflationary PBH models the background at re-entry depends critically on the reheating temperature T_{reh} . Two limiting cases arise.

Low reheating ($T_{\text{reh}} \lesssim T_{\text{form}}$). If the inflaton decay rate is small, the inflaton oscillates coherently after inflation ends and the universe is matter-dominated

at the epoch when the formation-scale perturbations re-enter the horizon [38, 53]. In this case the collapse occurs in an MD background and the HYKN formula with $\delta_c \approx 0.05$ applies, giving a Layer 1 floor identical to the non-inflationary early-MD mechanism:

$$\Delta_\sigma^{(\text{MD})} \approx 14, \quad (38)$$

identical to Eq. (27). For asteroid-mass PBHs with $T_{\text{form}} \sim 10^4\text{--}10^7$ GeV, this requires $T_{\text{reh}} \lesssim 10^7$ GeV, achievable in models with a weakly-coupled inflaton sector. Note that while the Layer 1 floor is the same as in the non-inflationary early-MD case, the two scenarios are physically distinct: here σ is not a free initial condition but is generated by the inflaton potential, and the additional cost of achieving the required σ is captured by Layer 2.

High reheating ($T_{\text{reh}} \gg T_{\text{form}}$). In the standard scenario where reheating completes well before the formation scale re-enters the horizon, the background is radiation-dominated at re-entry [11]. The collapse fraction follows the Press–Schechter form with $\delta_c \approx 0.45\text{--}0.55$ [21]:

$$\beta_{\text{RD}}(\sigma) = \frac{1}{2} \operatorname{erfc}\left(\frac{\delta_c}{\sqrt{2}\sigma}\right) \approx \frac{\sigma}{\delta_c\sqrt{2\pi}} \exp\left(-\frac{\delta_c^2}{2\sigma^2}\right), \quad (39)$$

where the approximation holds for $\delta_c/(\sqrt{2}\sigma) \gg 1$. Log-differentiating Eq. (39):

$$\Delta_\sigma^{(\text{RD})} = \left| \frac{\partial \ln \beta_{\text{RD}}}{\partial \ln \sigma} \right| = 1 + \frac{\delta_c^2}{\sigma^2}. \quad (40)$$

For asteroid-mass PBH production one requires $\beta_{\text{RD}} \sim 10^{-9}\text{--}10^{-15}$, giving $\delta_c^2/(2\sigma^2) \approx 20\text{--}35$, so $\sigma \approx 0.05\text{--}0.07$ for $\delta_c = 0.45\text{--}0.55$. Evaluating Eq. (40):

$$\Delta_\sigma^{(\text{RD})} \approx 57\text{--}70 \quad (\sigma \approx 0.06, \delta_c \approx 0.45\text{--}0.55), \quad (41)$$

approximately five times larger than the matter-dominated value of Eq. (38), reflecting the much higher collapse threshold in radiation domination.

The two Layer 1 floors bracket the Layer 1 contribution to the fine-tuning of inflationary models:

$$\Delta_\sigma^{(\text{inf})} \in [\Delta_\sigma^{(\text{MD})}, \Delta_\sigma^{(\text{RD})}] \approx [14, 57\text{--}70], \quad (42)$$

depending entirely on the reheating history. Figure 2 displays Δ_{tot} for both cases side by side, with the same x -axis scale to make the factor-of-five shift in the Layer 1 floor directly visible; note that for model classes with large Layer 2 sensitivity the total tuning is dominated by Layer 2 and the factor-of-five shift between panels becomes a small fractional effect. The enhanced power spectrum required for inflationary PBH production carries the same unavoidable scalar-induced gravitational-wave (SIGW) background prediction discussed in Sec. III B, with the additional feature that the peak frequency and amplitude directly encode the inflaton potential shape [44, 58, 59], making it a particularly powerful discriminant between inflationary PBH models.

Layer 2: $\{c_k\} \rightarrow \sigma$. The additional tuning specific to inflationary models enters through the mapping from the inflaton potential coefficients $\{c_k\}$ — e.g. the height of the inflection point, its slope, and the field value at which USR begins — to the power spectrum amplitude σ on the formation scale. Near an inflection point, the inflaton velocity $\dot{\phi}$ passes through a local minimum whose depth is controlled by the local slope c_{slope} of the potential. The power spectrum amplitude depends on $\dot{\phi}^{-2}$ at horizon crossing, so it is exponentially sensitive to c_{slope} :

$$\sigma \propto \exp\left(-\frac{\text{const}}{c_{\text{slope}}}\right). \quad (43)$$

A fractional change $\delta c_{\text{slope}}/c_{\text{slope}}$ therefore produces a fractional change $\delta\sigma/\sigma \propto \delta c_{\text{slope}}/c_{\text{slope}}^2$, an exponentially amplified response. Hertzberg and Yamada [19] quantified this explicitly for polynomial inflation potentials: a change in the potential coefficients by one part in $10^2\text{--}10^8$ (depending on the specific model) shifts the power spectrum peak amplitude by an order-one factor, implying $\Delta_{\sigma/c_k} \sim 10^2\text{--}10^8$. The total BG measure for the potential coefficients is therefore the product of the two layers,

$$\Delta_{c_k} \sim \Delta_\sigma \times \Delta_{\sigma/c_k} \sim (14\text{--}70) \times (10^2\text{--}10^8), \quad (44)$$

placing single-field inflationary collapse in Class III or beyond (as defined in Sec. V B) for essentially all realistic potentials [20, 21], with the Layer 1 factor ranging from 14 (low-reheating MD collapse) to 57–70 (high-reheating RD collapse) as discussed above. This double-exponential structure has no analog in the three mechanisms analyzed above, where the fundamental parameters (m_ϕ , V_b , T_* , β/H_*) map onto f_{PBH} through at most one exponential, and not through any hidden exponential in the parameter-to- σ map.

Note that the magnitude of Layer 2 varies enormously across inflationary model classes, as summarized in Fig. 2 and reviewed in detail in the next section. For single-field USR and inflection-point potentials $\Delta_{\sigma/c_k} \sim 10^2\text{--}10^8$, placing the total fine-tuning firmly in Class III or beyond (Sec. V B) regardless of the reheating history. For multi-field and spectator-field models $\Delta_{\sigma/c_k} \sim 2\text{--}10$; the total tuning then depends on whether collapse occurs in RD ($\Delta_{\text{tot}} \approx 115\text{--}700$, Class III for standard high reheating) or MD ($\Delta_{\text{tot}} \approx 21\text{--}140$, Class II to lower Class III for low reheating with $T_{\text{reh}} \lesssim T_{\text{form}}$). The severe fine-tuning of single-field USR inflationary PBH production is a specific pathology of models that rely on an exponentially sensitive slow-roll feature to amplify the power spectrum; the reheating history then sets the overall tuning scale for all other inflationary model classes.

The recent analysis of Iovino and Riotto [22] reaches a more optimistic conclusion by applying Wilson’s naturalness criterion to the potential coefficients rather than to σ . Their measure assigns a value close to unity even for fine-tuned inflaton potentials because it is constructed to

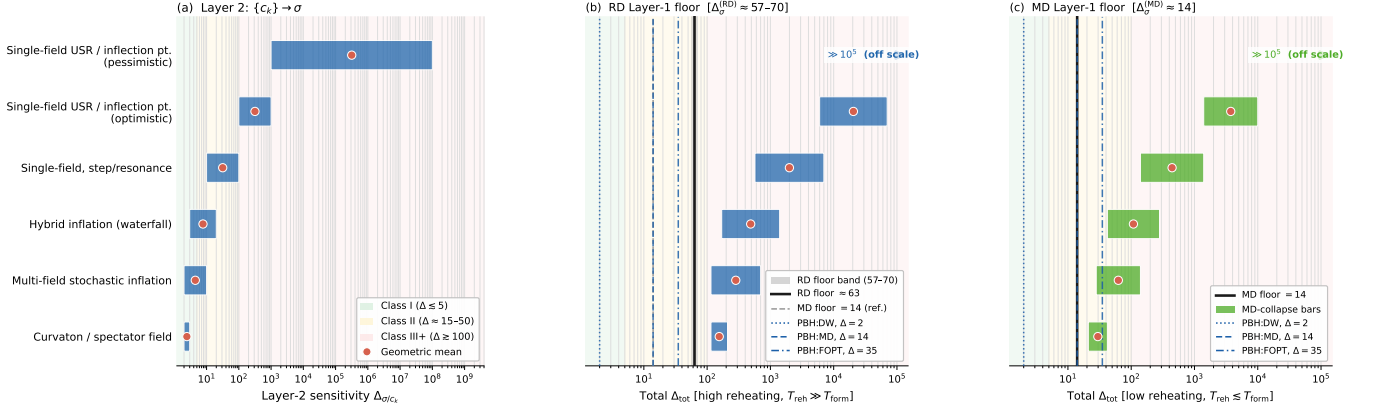


FIG. 2. Comparison of Layer 2 sensitivity (Δ_{σ/c_k} , panel a) and total fine-tuning ($\Delta_{\text{tot}} = \Delta_{\sigma} \times \Delta_{\sigma/c_k}$, panels b and c) across six inflationary PBH model classes, ordered from most natural (bottom) to most tuned (top). Bars show the estimated range within each class; the dot marks the geometric mean. Background shading indicates qualitative fine-tuning tier bands (Class I, II, and III; defined in Sec. VB). *Panel (b)*: total fine-tuning with the matter-dominated HYKN Layer 1 floor $\Delta_{\sigma}^{(\text{MD})} \approx 14$ (Eq. 38), applicable when $T_{\text{reh}} \lesssim T_{\text{form}}$ (low reheating, inflaton-oscillation MD era at re-entry). *Panel (c)*: total fine-tuning with the radiation-dominated Press–Schechter Layer 1 floor $\Delta_{\sigma}^{(\text{RD})} \approx 57\text{--}70$ (Eq. 41), applicable when $T_{\text{reh}} \gg T_{\text{form}}$ (standard high reheating, RD background at re-entry). The x -axes of panels (b) and (c) are identical (capped at 10^5) to make the factor-of-five shift in the Layer 1 floor directly visible; the top row (single-field USR pessimistic, $\Delta_{\text{tot}} \gtrsim 10^9\text{--}10^{10}$) is off scale and indicated by an arrow. Thick vertical gray lines mark the respective Layer 1 floor in each total-tuning panel; in panel (c) the gray band spans the 57–70 range. Blue vertical lines show the three non-inflationary PBH benchmarks (dotted: DW gravity-fixed, $\Delta = 2$; dashed: early MD, $\Delta = 14$; dash-dotted: FOPT, $\Delta = 35$, single-exponential approximation; see Sec. VIB for the more accurate estimate $\Delta \approx 265$). All ranges are estimates based on analytic scaling arguments and the results of Refs. [19, 69–75]; precise values are model-dependent.

be insensitive to the overall normalization of the abundance: a potential that predicts $f_{\text{PBH}} = 0.001$ and one that predicts $f_{\text{PBH}} = 1$ are treated as equally natural. The BG measure is more conservative in this respect: it registers the full sensitivity of f_{PBH} to each parameter along the observable contour $f_{\text{PBH}} = 1$, and therefore captures the double-exponential cost of maintaining that condition via an inflection-point potential. Both approaches are internally consistent, and answer complementary questions. The BG question is: “how precisely must the potential coefficient c_k be specified to keep $f_{\text{PBH}} \approx 1$?” The Wilson question is: “does a technically natural UV completion exist in which c_k takes its current value?” For the cross-paradigm comparison of this paper, the BG question is the relevant one, since it is the same question being asked of all other dark matter mechanisms in the comparison.

1. Fine-tuning across inflationary model classes

The analysis above shows that the double-exponential structure of Layer 2 is a specific property of single-field inflection-point or USR models, not a universal feature of inflationary PBH production. Figure 2 quantifies Layer 2 (Δ_{σ/c_k} , panel a) and the total fine-tuning Δ_{tot} for two choices of Layer 1 floor (panels b and c): the matter-dominated HYKN floor $\Delta_{\sigma}^{(\text{MD})} \approx 14$ that applies when $T_{\text{reh}} \lesssim T_{\text{form}}$ (low reheating, inflaton-oscillation era at

re-entry), and the radiation-dominated Press–Schechter floor $\Delta_{\sigma}^{(\text{RD})} \approx 57\text{--}70$ that applies when $T_{\text{reh}} \gg T_{\text{form}}$ (standard high reheating). The x -axes of panels (b) and (c) are identical to facilitate direct comparison; the pessimistic USR row ($\Delta_{\text{tot}} \gtrsim 10^9\text{--}10^{10}$) is off the shared scale and marked by an arrow. For reference, the three non-inflationary PBH benchmarks are shown as vertical blue lines in both total-tuning panels at $\Delta = 2, 14,$ and 35 .

I now discuss each model class in turn.

a. Curvaton and spectator-field models ($\Delta_{\sigma/c_k} \approx 2\text{--}3$; $\Delta_{\text{tot}} \approx 115\text{--}210$ [RD] or $21\text{--}42$ [MD]). In the curvaton mechanism, a light spectator field χ with mass $m_{\chi} \ll H_{\text{inf}}$ acquires perturbations $\delta\chi \simeq H_{\text{inf}}/(2\pi)$ during inflation and later converts them into curvature perturbations when it decays [76, 77]. PBH production requires an enhanced curvature perturbation on sub-CMB scales, which can be arranged if χ rolls along a self-interacting potential that generates a non-Gaussian or scale-dependent signal on those scales [69, 70]. The key structural property is that the curvature power spectrum scales as $\mathcal{P}_{\mathcal{R}} \propto (H_{\text{inf}}/m_{\chi})^{2n}$ for some integer $n \geq 1$ depending on the interaction structure. The BG sensitivity of σ to the curvaton mass is therefore $\Delta_{\sigma/m_{\chi}} = n \approx 1\text{--}2$, and to the self-coupling $\Delta_{\sigma/\lambda} \approx 1$. The combined Layer 2 is $\Delta_{\sigma/c_k} \approx 2\text{--}3$. Multiplied by the RD Layer 1 floor $\Delta_{\sigma}^{(\text{RD})} \approx 57\text{--}70$ (Eq. 41), the total fine-tuning is $\Delta_{\text{tot}} \approx 115\text{--}210$ (Class III, Sec. VB) for standard high-reheating scenarios. For low-reheating scenarios where

collapse occurs during the inflaton-oscillation matter-dominated era, the MD Layer 1 floor applies and the total reduces to $\Delta_{\text{tot}} \approx 21\text{--}42$ (Class II, Sec. VB), comparable to the early-matter-domination mechanism of Sec. IIIB. The reheating temperature is therefore a critical parameter that determines whether curvaton PBH models belong to Class II or Class III.

b. Multi-field stochastic inflation ($\Delta_{\sigma/c_k} \approx 2\text{--}10$; $\Delta_{\text{tot}} \approx 115\text{--}700$ [RD] or $28\text{--}140$ [MD]). When the inflaton traverses an approximately flat direction, quantum diffusion can compete with or dominate the classical drift, and the statistics of perturbations must be described by a Fokker–Planck equation rather than the standard linear perturbation theory [78]. In multi-field models where a secondary field undergoes stochastic diffusion, the power spectrum amplitude on a given scale is controlled by the ratio $H_{\text{inf}}/M_{\text{flat}}$, where M_{flat} is the effective mass of the flat direction [71, 79]. Since $\mathcal{P}_{\mathcal{R}} \propto (H_{\text{inf}}/M_{\text{flat}})^4$, the Layer 2 sensitivity is $\Delta_{\sigma/M_{\text{flat}}} \approx 2$ per parameter, giving a combined $\Delta_{\sigma/c_k} \approx 2\text{--}10$ when multiple parameters of the flat-direction potential contribute. Multiplied by the RD Layer 1 floor $\Delta_{\sigma}^{(\text{RD})} \approx 57\text{--}70$ (Eq. 41), the total fine-tuning range is $\Delta_{\text{tot}} \approx 115\text{--}700$ (Class III, Sec. VB) for high-reheating scenarios; with the MD floor the range reduces to $\Delta_{\text{tot}} \approx 28\text{--}140$, straddling the Class II/III boundary. The upper end of this range arises when the stochastic enhancement requires the flat direction to remain nearly degenerate with the inflationary trajectory for a precise number of e-folds [71], introducing additional sensitivity that stretches the Layer 2 estimate toward its upper bound.

c. Hybrid inflation with waterfall transition ($\Delta_{\sigma/c_k} \approx 3\text{--}20$; $\Delta_{\text{tot}} \approx 170\text{--}1400$ [RD] or $42\text{--}280$ [MD]). In hybrid inflation, the inflaton ϕ rolls toward a critical value ϕ_c at which a “waterfall” field ψ becomes tachyonic and triggers the end of inflation [80]. Near ϕ_c , the perturbations of ψ are dramatically amplified because its effective mass $m_{\psi}^2 \approx g^2(\phi - \phi_c)M^{-2} - \mu^2$ approaches zero, and regions where the transition is delayed can collapse into PBHs [72]. The curvature power spectrum amplitude scales as a power law in the coupling g and the mass parameter μ : $\mathcal{P}_{\mathcal{R}} \propto g^{-2n} \mu^{2m}$ for integers n, m depending on the potential shape, giving $\Delta_{\sigma/g} \approx n$ and $\Delta_{\sigma/\mu} \approx m$. For a mild waterfall ($|\phi - \phi_c|$ not exponentially small), $n + m \approx 3\text{--}5$ and the Layer 2 tuning is modest. However, as $\phi \rightarrow \phi_c$ more closely, the enhancement duration becomes exponentially sensitive to the proximity to the critical point, stretching Δ_{σ/c_k} toward $10\text{--}20$ at the upper end. Multiplied by the RD Layer 1 floor, the resulting total tuning is $\Delta_{\text{tot}} \approx 170\text{--}1400$ (Class III, Sec. VB) for high-reheating scenarios; with the MD floor the range is $\Delta_{\text{tot}} \approx 42\text{--}280$, in the lower part of Class III.

d. Single-field with step or resonance feature ($\Delta_{\sigma/c_k} \approx 10\text{--}100$; $\Delta_{\text{tot}} \approx 570\text{--}7000$ [RD] or $140\text{--}1400$ [MD]). A sharp feature such as a step, a bump, or a periodic modulation in the single-field inflaton potential can resonantly amplify perturbations as modes cross the feature [73, 81]. For a step of height h at field value ϕ_s ,

the peak power spectrum scales roughly as $\mathcal{P}_{\mathcal{R}}^{\text{peak}} \propto h^2$, a polynomial relationship giving $\Delta_{\sigma/h} \approx 1$. The dominant source of Layer 2 tuning is therefore not the feature amplitude but its position: the resonance condition requires that precisely the modes corresponding to the asteroid-mass scale cross the horizon when the inflaton is at the step location. A small change $\delta\phi_s$ in the step position shifts the resonant scale by $\delta k/k \sim \delta\phi_s/(\phi_s - \phi_{\text{CMB}})$, changing which physical scales are enhanced. In terms of the inflaton potential coefficients, $\Delta_{\sigma/\phi_s} \sim 10\text{--}50$ because ϕ_s must be tuned at the $2\text{--}10\%$ level to target the asteroid-mass window specifically. The combined Layer 2 is $\Delta_{\sigma/c_k} \approx 10\text{--}100$; multiplied by the RD Layer 1 floor this gives $\Delta_{\text{tot}} \approx 570\text{--}7000$ (Class III, Sec. VB) for high-reheating scenarios, or $\Delta_{\text{tot}} \approx 140\text{--}1400$ with the MD floor. A key advantage of this class of models is that the prediction is falsifiable: the power spectrum feature also produces a distinctive oscillatory signature in the SIGW background [81] that is detectable by LISA for formation temperatures in the asteroid-mass range.

e. Single-field USR / inflection point, optimistic ($\Delta_{\sigma/c_k} \approx 10^2\text{--}10^3$; $\Delta_{\text{tot}} \approx 6000\text{--}7 \times 10^4$ [RD] or $1400\text{--}10^4$ [MD]). For a single inflaton field with an inflection point, the slow-roll velocity passes through a local minimum controlled by the local slope c_{slope} of the potential. In the USR regime, quantum perturbations grow as $\delta\phi \propto e^{3Ht}$ rather than remaining constant, amplifying the power spectrum by a factor $e^{6\Delta N_{\text{USR}}}$ over ΔN_{USR} e-folds of USR evolution [74]. The number of USR e-folds required to achieve $\mathcal{P}_{\mathcal{R}} \sim 10^{-2}$ from a CMB-scale amplitude $\mathcal{P}_{\mathcal{R}}^{\text{CMB}} \sim 2 \times 10^{-9}$ is $\Delta N_{\text{USR}} \approx 2.7$, which in turn requires the potential slope to satisfy $c_{\text{slope}} \approx \text{const}/\Delta N_{\text{USR}}$. In the optimistic case, corresponding to potentials where the inflection point is only mildly fine-tuned and the coefficients are of order unity, $\Delta_{\sigma/c_{\text{slope}}} \approx \text{const}/c_{\text{slope}} \sim 10^2\text{--}10^3$ (the Hertzberg–Yamada lower-end result [19]). Multiplied by the RD Layer 1 floor, the total tuning is $\Delta_{\text{tot}} \approx 6000\text{--}7 \times 10^4$ (high-reheating) or $\Delta_{\text{tot}} \approx 1400\text{--}10^4$ (low-reheating), in either case deep in Class III (Sec. VB); a change of order 0.1% in the inflaton potential slope is sufficient to miss the target abundance by a factor of order unity.

f. Single-field USR / inflection point, pessimistic ($\Delta_{\sigma/c_k} \approx 10^3\text{--}10^8$; $\Delta_{\text{tot}} \gtrsim 10^{10}$ [RD] or $\gtrsim 10^9$ [MD]). For a generic polynomial inflaton potential, the relation between the potential coefficients at the inflection point and the resulting power spectrum amplitude is far more sensitive than the optimistic case suggests. A detailed analysis of polynomial potentials of the form $V(\phi) = V_0[1 + a_2(\phi/M)^2 + a_3(\phi/M)^3 + \dots]$ by Hertzberg and Yamada [19] and by Kannike, Raidal, and Veerman [75] shows that the required amplitude $\mathcal{P}_{\mathcal{R}} \sim 10^{-2}$ at k_{form} is consistent with the CMB constraint $\mathcal{P}_{\mathcal{R}} \sim 2 \times 10^{-9}$ at k_{CMB} only if the potential coefficients satisfy a set of near-cancellation conditions. In the generic case, achieving both constraints simultaneously requires tuning the coefficients to within one part in $10^3\text{--}10^8$, giving $\Delta_{\sigma/c_k} \sim 10^3\text{--}10^8$. Multiplied by the RD Layer 1 floor,

the resulting total fine-tuning reaches $\Delta_{\text{tot}} \gtrsim 10^{10}$ (high-reheating) or $\Delta_{\text{tot}} \gtrsim 10^9$ (low-reheating), far exceeding any other scenario considered in this paper in either case. This pessimistic range represents the majority of the parameter space for generic polynomial inflaton potentials; the optimistic range is accessible only in models with additional symmetry or structure that correlates the potential coefficients in a way that reduces the cancellation requirement.

The overall message of Fig. 2 is stark: the fine-tuning of inflationary PBH production spans more than seven orders of magnitude depending on the model class, in either reheating scenario. For low reheating ($T_{\text{reh}} \lesssim T_{\text{form}}$, MD Layer 1 floor), curvaton and spectator-field models ($\Delta_{\text{tot}} \approx 21\text{--}42$) fall in Class II, comparable to the non-inflationary early-MD mechanism and to coannihilating-WIMP dark matter. For high reheating ($T_{\text{reh}} \gg T_{\text{form}}$, RD Layer 1 floor), every inflationary class falls in Class III or beyond; the most natural class (curvaton/spectator, $\Delta_{\text{tot}} \approx 115\text{--}210$) is roughly five times more tuned than the corresponding low-reheating estimate, reflecting the factor-of-five ratio of the two Layer 1 floors — a shift that is clearly visible for model classes with small Layer 2 sensitivity, but becomes a minor correction when Layer 2 dominates. In both cases the Layer 2 sensitivity Δ_{σ/c_k} spans five orders of magnitude from curvaton models to single-field USR potentials, so the mechanism for enhancing the power spectrum remains the most physically informative quantity regardless of the reheating history.

IV. PARTICLE DARK MATTER BENCHMARKS

I now apply the same BG protocol to seven particle dark matter benchmarks spanning four production paradigms: thermal-relic WIMPs (B1–B3), freeze-in (B4), asymmetric dark matter (B5), and axions (B6, B7). The purpose is not to provide a comprehensive survey of the particle dark matter landscape, but to place specific, representative benchmarks into the same quantitative framework used for the PBH constructions in Sec. III. The benchmarks are chosen to span the full range of BG fine-tuning observed in the particle literature and to correspond to physically well-motivated, phenomenologically viable scenarios.

A. Thermal-relic WIMPs

Thermal relics freeze out when their annihilation rate falls below the Hubble rate at temperature $T_{\text{fo}} = M_\chi/x_F$ with $x_F \approx 25$ [1, 82]. The relic abundance is then determined by the Lee–Weinberg relation

$$\Omega_\chi h^2 \simeq \frac{1.07 \times 10^9 \text{ GeV}^{-1} x_F}{g_*^{1/2} M_{\text{Pl}} \langle \sigma v \rangle_{\text{fo}}}, \quad (45)$$

where $g_* \approx 86$ counts the effective relativistic degrees of freedom at freeze-out and $\langle \sigma v \rangle_{\text{fo}}$ is the thermally-averaged annihilation cross section evaluated at T_{fo} . The “WIMP miracle” is the observation that for $M_\chi \sim 100$ GeV and gauge-coupling-strength $\langle \sigma v \rangle \sim \alpha_W^2/M_W^2 \sim 6.7 \times 10^{-9} \text{ GeV}^{-2}$, Eq. (45) gives $\Omega h^2 \approx 0.12$ [1]. I analyze three qualitatively distinct WIMP benchmarks that span the range of BG fine-tuning encountered in this paradigm.

1. Off-resonance Higgs-portal singlet (B1)

The simplest renormalizable portal between the Standard Model and a dark sector is the real singlet scalar S with Lagrangian

$$\mathcal{L} \supset \frac{1}{2}(\partial S)^2 - \frac{1}{2}M_S^2 S^2 - \frac{\lambda_{HS}}{4} S^2 H^\dagger H, \quad (46)$$

where λ_{HS} is the Higgs-portal coupling [83–85]. After electroweak symmetry breaking, S acquires an effective coupling to the physical Higgs h and annihilates through $SS \rightarrow hh, WW, ZZ, \bar{f}f$ channels. In the off-resonance regime $M_S \gg M_h/2$, the thermally-averaged cross section for these channels scales as

$$\langle \sigma v \rangle \simeq \lambda_{HS}^2 \frac{v_{\text{EW}}^2}{8\pi M_S^2} \equiv \lambda_{HS}^2 \sigma_0 (2 \text{ TeV}/M_S)^2, \quad (47)$$

where $\sigma_0 = 6.7 \times 10^{-9} \text{ GeV}^{-2}$ is calibrated so that the benchmark B1 ($M_S = 2 \text{ TeV}$, $\lambda_{HS} = 1.0$) satisfies $\Omega h^2 = 0.12$ exactly. Substituting into Eq. (45),

$$\Omega h^2 \propto \frac{M_S^2}{\lambda_{HS}^2}, \quad (48)$$

a pure power-law in both parameters. Log-differentiation gives immediately

$$\Delta_{M_S}^{(\text{B1})} = 2, \quad \Delta_{\lambda_{HS}}^{(\text{B1})} = 2, \quad \Delta^{(\text{B1})} = 2. \quad (49)$$

These are constants, independent of (M_S, λ_{HS}) , for the same structural reason as the domain-wall PBH: the abundance is a monomial in the parameters.

The spin-independent direct-detection cross section at benchmark B1 is $\sigma_{\text{SI}} \approx 1.3 \times 10^{-49} \text{ cm}^2$, more than two orders of magnitude below the LZ 2024 limit at $M_S = 2 \text{ TeV}$. Benchmark B1 is therefore currently unconstrained by direct detection, and lies in the “decoupling” regime of the singlet parameter space where the WIMP is heavy enough to satisfy both relic density and direct-detection constraints without fine-tuning.

2. Higgs-funnel resonant singlet (B2)

When $M_S \approx M_h/2 \approx 62.5 \text{ GeV}$, the annihilation proceeds through an s -channel Higgs resonance. The

thermally-averaged cross section is enhanced relative to the off-resonance value by a Breit–Wigner factor,

$$\langle\sigma v\rangle_{\text{res}} \simeq \langle\sigma v\rangle_{\text{off}} \times \frac{R_{\text{max}}(\Gamma_h M_h)^2}{(s_{\text{eff}} - M_h^2)^2 + (\Gamma_h M_h)^2}, \quad (50)$$

where $s_{\text{eff}} = 4M_S^2(1 + 3/2x_F)$ is the center-of-mass energy squared evaluated at the freeze-out temperature, $\Gamma_h = 4.07 \times 10^{-3}$ GeV is the total Higgs width, and $R_{\text{max}} \approx 10^4$ is the peak resonance enhancement after thermal averaging [29, 86]. Benchmark B2 ($M_S = 60.7$ GeV, $\lambda_{HS} = 0.026$) is calibrated so that $\Omega h^2 = 0.12$ on the near-resonance tail.

The BG measure in the resonant regime is dominated by the sensitivity of $s_{\text{eff}} - M_h^2$ to M_S : a fractional shift ϵ in M_S shifts the denominator in Eq. (50) by $\delta(s_{\text{eff}} - M_h^2) \approx 8M_S^2 \epsilon$, producing a fractional change in $\langle\sigma v\rangle$ of order $8M_S^2/(\Gamma_h M_h)$. More precisely, numerical evaluation at B2 gives

$$\Delta_{M_S}^{(\text{B2})} \approx 6500, \quad \Delta_{\lambda_{HS}}^{(\text{B2})} = 2, \quad \Delta^{(\text{B2})} \approx 6500. \quad (51)$$

The coupling sensitivity remains at 2 because $\langle\sigma v\rangle \propto \lambda_{HS}^2$ regardless of whether the resonance is resolved, but the mass sensitivity is set by the inverse fractional pole width: $\Delta_{M_S}^{(\text{B2})} \sim 8M_S^2/(\Gamma_h M_h) \approx 4M_h/\Gamma_h \approx 1.2 \times 10^5$, reduced to ~ 6500 by thermal averaging at finite x_F . This is the “funnel tuning” that appears generically in models where the relic density is set by a resonant annihilation channel, including the A -funnel of the MSSM [29] and the Z -funnel of Higgs-portal dark matter.

The benchmark B2 is not yet excluded by LZ 2024 ($\sigma_{\text{SI}} \approx 9 \times 10^{-50}$ cm², well below the sensitivity limit at 60 GeV), but the combination of small coupling required by the relic density and the extreme sensitivity of the abundance to M_S makes this benchmark qualitatively distinct from B1: it is natural in λ_{HS} but requires the singlet mass to be fixed at the sub-percent level.

3. Coannihilating MSSM bino (B3)

When the lightest supersymmetric particle (LSP) is a bino-like neutralino χ with mass M_χ , its self-annihilation cross section is suppressed by the hypercharge coupling and the typically large sfermion masses appearing in t -channel exchange diagrams. The relic density from bino self-annihilation alone generically exceeds $\Omega h^2 = 0.12$ by orders of magnitude. Coannihilation with a nearly-degenerate next-to-lightest supersymmetric particle (NLSP) resolves this by augmenting the effective annihilation rate with the NLSP’s own (typically gauge-strength) cross section, weighted by the Boltzmann-suppressed NLSP number density at freeze-out [29, 30]:

$$\begin{aligned} \langle\sigma v\rangle_{\text{eff}} &\approx \langle\sigma v\rangle_{\chi\chi} \\ &+ 2g_{\text{eff}} f(x_F) \sqrt{\langle\sigma v\rangle_{\chi\chi} \langle\sigma v\rangle_{\text{NLSP}}} \\ &+ g_{\text{eff}}^2 f^2(x_F) \langle\sigma v\rangle_{\text{NLSP}}, \end{aligned} \quad (52)$$

where $g_{\text{eff}} \approx 4$ counts the NLSP internal degrees of freedom relative to the bino, and $f(x_F) = (1 + \delta)^{3/2} \exp(-\delta x_F)$ with $\delta = (M_{\text{NLSP}} - M_\chi)/M_\chi$ is the Boltzmann suppression factor. The benchmark B3 ($M_\chi = 1$ TeV, $M_{\text{NLSP}} = 1.05$ TeV, i.e. $\delta = 0.05$) is calibrated so that $\Omega h^2 \approx 0.12$ with $\langle\sigma v\rangle_{\text{NLSP}} = 0.66 \sigma_0 (1 \text{ TeV}/M_\chi)^2$.

As discussed in Sec. IIB, the BG derivatives must be taken with respect to the fundamental soft masses (M_χ, M_{NLSP}) rather than the derived splitting δ . The exponential factor $f(x_F) = (1 + \delta)^{3/2} e^{-\delta x_F}$ gives, at fixed M_χ ,

$$\frac{\partial \ln \langle\sigma v\rangle_{\text{eff}}}{\partial \ln M_{\text{NLSP}}} \approx -\delta x_F \frac{M_{\text{NLSP}}}{M_\chi} = -\delta x_F (1 + \delta), \quad (53)$$

and the BG measure on Ω (which is inversely proportional to $\langle\sigma v\rangle_{\text{eff}}$) satisfies

$$\Delta_{M_{\text{NLSP}}}^{(\text{B3})} \approx x_F \frac{M_{\text{NLSP}}}{M_\chi} \approx 26 \frac{M_{\text{NLSP}}}{M_\chi}. \quad (54)$$

At benchmark B3, $M_{\text{NLSP}}/M_\chi = 1.05$, giving $\Delta_{M_{\text{NLSP}}} \approx 48$, while $\Delta_{M_\chi} \approx 46$ from the overall $\langle\sigma v\rangle_{\text{NLSP}} \propto M_\chi^{-2}$ dependence. The total measure is $\Delta^{(\text{B3})} = 48$.

This result places the coannihilating WIMP solidly in the same tier as FOPT-PBH dark matter ($\Delta = 35$), and for the same structural reason: both constructions contain a single exponential whose argument is forced by the requirement $\Omega = \Omega_{\text{DM}}$ to equal $\ln(T_{\text{form}}/T_{\text{eq}})$ or $x_F \delta$, respectively (see Sec. VC). The BG landscape of Fig. 3(b), computed in the $(M_\chi, M_{\text{NLSP}})$ plane, shows the natural island as a narrow teal-colored strip hugging the diagonal $M_{\text{NLSP}} = M_\chi$ at a fixed $\Delta \approx 48$ set by $x_F M_{\text{NLSP}}/M_\chi$ across the full mass range 100 GeV to 10 TeV.

B. Freeze-in (FIMP)

1. Production mechanism and abundance map

Feebly interacting massive particles (FIMPs) [6, 7] never reach thermal equilibrium with the Standard Model bath; instead, they are produced gradually in the forward direction through infrequent collisions or decays. In the IR-dominated freeze-in scenario relevant here, production is dominated by decays of a heavy Standard Model or dark-sector mediator B with mass M_B and decay coupling y to two DM particles, $B \rightarrow \text{DM} + X$. Following Hall et al. [6], the yield produced by this mechanism from $T \gg M_B$ down to $T = 0$ is

$$Y_{\text{FI}} = \frac{45 \mathcal{X}_{\text{FI}}}{\pi^4 g_*^{3/2}} \cdot \frac{y^2 M_{\text{Pl}}}{M_B} \equiv K_{\text{FI}} \frac{y^2 M_{\text{Pl}}}{M_B}, \quad (55)$$

where $K_{\text{FI}} \approx 1.7 \times 10^{-3}$ for $g_* = 100$ and \mathcal{X}_{FI} is a dimensionless integral of order unity that depends mildly on

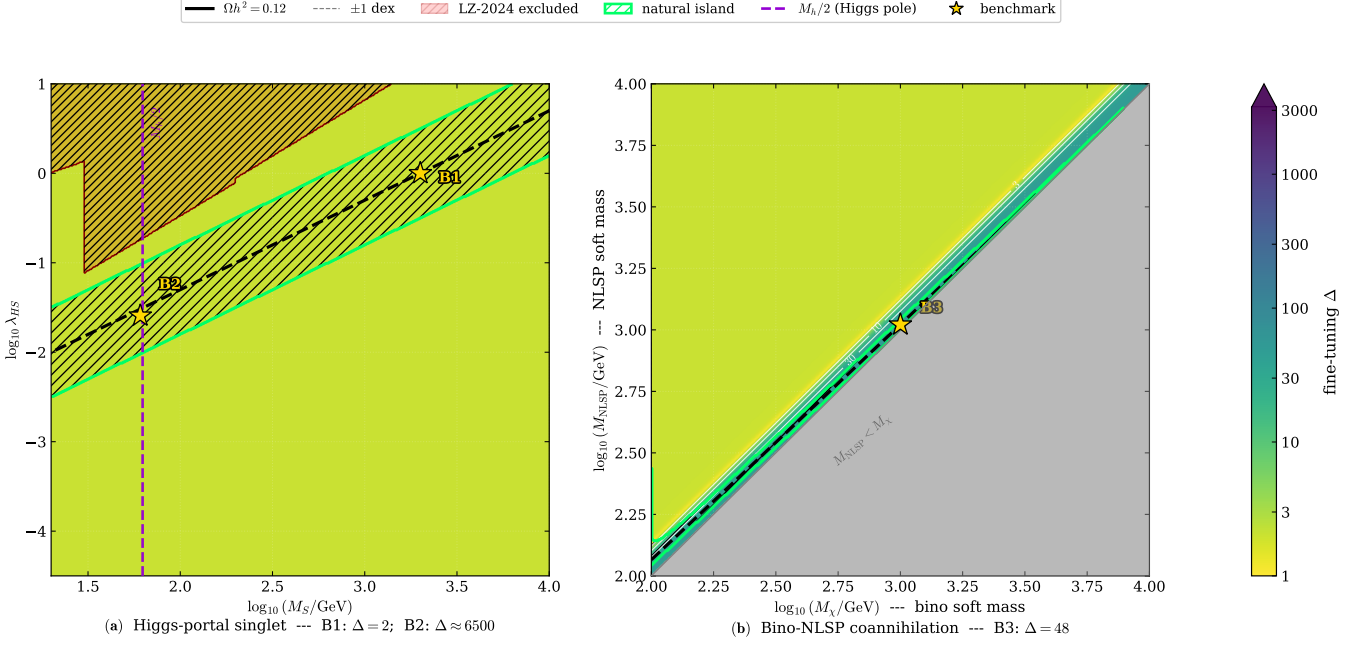


FIG. 3. Fine-tuning of thermal-relic WIMP dark matter. Color scale, contours, and natural island (green hatching) as in Fig. 1, with $\Omega h^2 = 0.12$ replacing $f_{\text{PBH}} = 1$ as the abundance target. The red-shaded region is excluded at 90% CL by LZ 2024 spin-independent direct detection [32]. (a) Real singlet Higgs-portal WIMP in the (M_S, λ_{HS}) plane (Eq. 46). The cyan dotted vertical line marks $M_S = M_h/2$ (Higgs pole). Benchmark B1 (off-resonance, gold star): $M_S = 2$ TeV, $\lambda_{HS} = 1$; $\Delta = 2.0$. Benchmark B2 (Higgs funnel, gold star): $M_S = 60.7$ GeV, $\lambda_{HS} = 0.026$; $\Delta \approx 6500$ (color saturated to dark purple). The contrast between B1 (uniformly yellow stripe) and B2 (deep purple near the resonance) illustrates the Class I vs. Class III distinction. (b) MSSM bino-NLSP coannihilation in the fundamental soft-mass plane $(M_\chi, M_{\text{NLSP}})$, using Eqs. (52)–(54). The gray-shaded triangle is the unphysical region $M_{\text{NLSP}} < M_\chi$. The natural island (narrow teal strip) hugs the diagonal at constant $\Delta \approx 48 = x_F M_{\text{NLSP}}/M_\chi$. Benchmark B3: $M_\chi = 1$ TeV, $M_{\text{NLSP}} = 1.05$ TeV; $\Delta = 48$.

the spin of B . The present-day dark matter abundance is then

$$\Omega_{\text{DM}} h^2 = M_{\text{DM}} Y_{\text{FI}} \frac{s_0}{\rho_c/h^2} \propto M_{\text{DM}} y^2 \frac{M_{\text{Pl}}}{M_B}, \quad (56)$$

where $s_0/(\rho_c/h^2) \approx 2.7 \times 10^8 \text{ GeV}^{-1}$ converts yield to Ωh^2 [82]. I fix the mediator mass $M_B = 100$ GeV (electroweak scale) as a representative choice; the scaling $\Omega h^2 \propto M_B^{-1}$ means that changing M_B by a factor of 10 shifts the natural value of y by a factor of $\sqrt{10}$, but does not change the BG measure.

Benchmark B4 is defined by $M_{\text{DM}} = 1$ GeV and $y = 1.46 \times 10^{-12}$, giving $\Omega h^2 = 0.120$.

2. Fine-tuning structure

Since Eq. (56) is a pure monomial in (M_{DM}, y) with fixed M_B ,

$$\Delta_{M_{\text{DM}}}^{(\text{B4})} = 1, \quad \Delta_y^{(\text{B4})} = 2, \quad \Delta^{(\text{B4})} = 2 \quad (57)$$

exactly, everywhere in the (M_{DM}, y) plane. The mass sensitivity is unity because $\Omega \propto M_{\text{DM}}$ linearly; the coupling sensitivity is two because $\Omega \propto y^2$. These are

constants, independent of the benchmark point, for the same structural reason as benchmark B1 and the biased-domain-wall PBH: the abundance map is a power-law monomial with no exponential, resonance, or cancellation.

The FIMP scenario is thus as natural as the off-resonance WIMP by the BG criterion, despite the coupling being smaller by nine orders of magnitude. The febleness of the coupling is not fine-tuning in the BG sense; it is, rather, the *prediction* of the freeze-in mechanism, which requires $y \sim 10^{-12}$ to avoid thermalizing the DM sector. What the BG measure quantifies is not the smallness of y itself, but the sensitivity of Ωh^2 to *fractional variations* of y ; a factor-of-two change in y changes Ωh^2 by a factor of four, which is $\Delta_y = 2$, perfectly natural.

3. Parameter-space heatmap

Figure 4(a) shows $\log_{10} \Delta$ in the (M_{DM}, y) plane for $M_B = 100$ GeV. The panel is uniformly pale yellow at the minimum of the color scale ($\Delta = 2$) throughout the physically accessible region, with the natural island (green hatching along the $\Omega h^2 = 0.12$ contour) form-

ing a clean diagonal stripe of slope $-1/2$ in the log–log plane, as expected from $y \propto M_{\text{DM}}^{-1/2}$ at fixed Ω . The red-shaded region at $M_{\text{DM}} \lesssim 3$ keV marks the Lyman- α forest exclusion for freeze-in production from a 100-GeV mediator [34, 35]. Benchmark B4 (gold star) lies at the center of the natural island in the phenomenologically well-motivated GeV mass range. The uniformity of the heatmap is perhaps the most striking visual feature of the FIMP panel: there are no gradients, no tuned corners, and no preferred points other than those set by external constraints.

C. Asymmetric dark matter

1. Abundance map and fine-tuning

Asymmetric dark matter (ADM) [8, 9] posits that the present-day dark matter abundance is set not by thermal freeze-out but by a primordial asymmetry between DM particles and antiparticles, generated by the same baryogenesis mechanism that produced the baryon asymmetry. If the DM asymmetry per comoving entropy is $\eta_{\text{DM}} = (n_{\text{DM}} - n_{\bar{\text{DM}}})/s$, and all $\bar{\text{DM}}$ is annihilated away efficiently (as required for the mechanism to work), then

$$\frac{\Omega_{\text{DM}}}{\Omega_b} = \frac{M_{\text{DM}}}{m_p} R, \quad R \equiv \frac{\eta_{\text{DM}}}{\eta_B}, \quad (58)$$

where $m_p = 0.938$ GeV is the proton mass and $\eta_B \approx 8.7 \times 10^{-11}$ is the baryon asymmetry [24]. With $\Omega_b h^2 = 0.0224$ and $\Omega_{\text{DM}} h^2 = 0.120$, the observed ratio $\Omega_{\text{DM}}/\Omega_b = 5.4$ requires

$$M_{\text{DM}} R \simeq 5.0 m_p \approx 4.7 \text{ GeV}. \quad (59)$$

The natural island in the (M_{DM}, R) plane is the hyperbola $M_{\text{DM}} \times R = 4.7$ GeV (or within a factor of two thereof), ranging from the proton mass at $R = 5$ to multi-TeV masses at $R \sim 10^{-3}$. Benchmark B5 is defined by $M_{\text{DM}} = 5.0$ GeV, $R = 1$ (equal DM and baryon asymmetries), a canonical choice motivated by models in which baryogenesis and DM asymmetry generation proceed via the same operator [9].

Since Eq. (58) is linear in both M_{DM} and R ,

$$\Delta_{M_{\text{DM}}}^{(\text{B5})} = 1, \quad \Delta_R^{(\text{B5})} = 1, \quad \Delta^{(\text{B5})} = 1. \quad (60)$$

This is the minimum possible BG measure for a non-trivial abundance map: $\Delta = 1$ means the abundance is simply proportional to the parameter, and a factor-of-two change in either M_{DM} or R produces a factor-of-two change in $\Omega_{\text{DM}} h^2$. Asymmetric dark matter is the most natural dark matter scenario in the full comparison precisely because its abundance is set by a ratio of number densities (R) that is itself a direct observable, and by the particle mass M_{DM} , both entering linearly.

Figure 4(b) shows the ADM parameter space in the (M_{DM}, R) plane. The panel is uniformly yellow at

$\Delta = 1$ throughout, with the natural island forming the $M_{\text{DM}} \times R = 4.7$ GeV diagonal. The cyan dashed line at $R = 1$ marks the ‘‘canonical ADM’’ locus where DM and baryon asymmetries are equal; benchmark B5 sits at its intersection with the natural island.

D. Axions

The QCD axion [3–5] acquires a mass $m_a \simeq 5.7 \mu\text{eV} (10^{12} \text{ GeV}/f_a)$ from non-perturbative QCD effects, where f_a is the Peccei–Quinn (PQ) symmetry-breaking scale. Its cosmological abundance depends critically on whether PQ symmetry breaks before or after inflation, leading to two qualitatively distinct scenarios with different numbers of free parameters and different BG structures.

1. Misalignment (pre-inflationary PQ breaking)

If PQ symmetry breaks before the end of inflation, the axion field $\theta = a/f_a$ is homogenized over superhorizon scales and takes a single value $\theta_i \in [-\pi, \pi]$ throughout our observable Universe (the ‘‘misalignment angle’’). When the Hubble rate falls below the axion mass at temperature $T_{\text{osc}} \sim \Lambda_{\text{QCD}}$, the field begins to oscillate coherently around $\theta = 0$, and the energy density of these oscillations constitutes the dark matter relic. Including the anharmonic correction $F(\theta_i)$ that becomes important as $\theta_i \rightarrow \pi$ [87],

$$\Omega_a h^2 \simeq 0.18 \theta_i^2 \left(\frac{f_a}{10^{12} \text{ GeV}} \right)^{1.19} F(\theta_i), \quad (61)$$

where the exponent 1.19 arises from the temperature dependence of the axion mass near the QCD transition [88] and $F(\theta_i)$ is a smooth, monotonically increasing function satisfying $F(\theta_i) \rightarrow 1$ as $\theta_i \rightarrow 0$ and $F(\theta_i) \rightarrow \infty$ as $\theta_i \rightarrow \pi$ [87]. Benchmark B6 is defined by $f_a = 10^{12}$ GeV and $\theta_i = 0.82$, which gives $\Omega h^2 = 0.131$ with $F(\theta_i) \approx 1$ (anharmonic corrections are $\lesssim 10\%$ at this angle); this is within 9% of the observed value, consistent with theoretical uncertainties in the relic-abundance calculation.

The BG sensitivities follow from log-differentiation of Eq. (61):

$$\Delta_{f_a}^{(\text{B6})} = 1.19, \quad (62)$$

$$\Delta_{\theta_i}^{(\text{B6})} = 2 + \theta_i \frac{\partial \ln F}{\partial \theta_i} \approx 2.2 \quad (\theta_i = 0.82), \quad (63)$$

giving $\Delta^{(\text{B6})} = \max(1.19, 2.2) = 2.2$.

This places the misalignment axion with $\theta_i \sim 1$ comfortably in the natural tier (Class I of Sec. V B). However, there is an important subtlety that the BG measure alone does not capture. If f_a is large (e.g., $f_a = 10^{16}$ GeV as in models with a GUT-scale or string-theoretic PQ scale), then $\Omega h^2 = 0.12$ requires a small misalignment angle

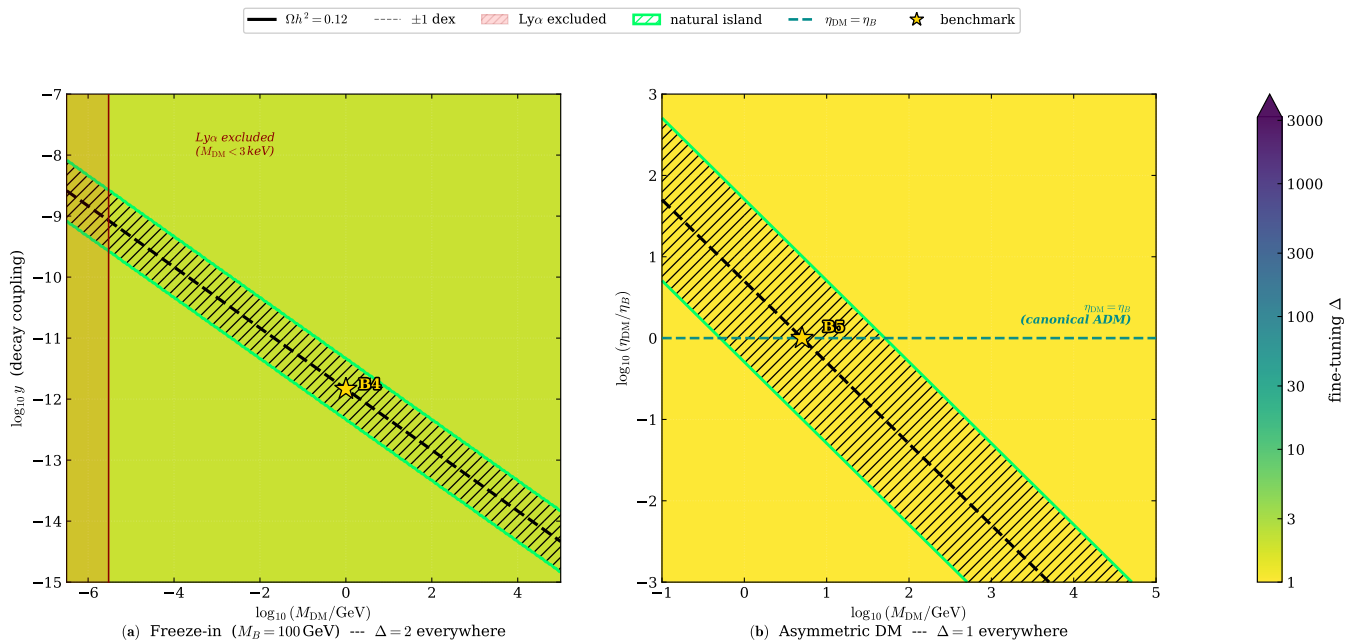


FIG. 4. Fine-tuning of non-thermal dark matter production. Color scale and conventions as in Fig. 1. Both panels are uniformly pale yellow, reflecting power-law abundance maps with $\Delta \leq 2$ everywhere. **(a)** Freeze-in via heavy-mediator decay $B \rightarrow \text{DM} + X$ with fixed mediator mass $M_B = 100$ GeV, in the (M_{DM}, y) plane (Eqs. 55–56). The red-shaded region at $M_{\text{DM}} \lesssim 3$ keV is excluded by Lyman- α forest observations [34, 35]. The natural island is the diagonal stripe $y \propto M_{\text{DM}}^{-1/2}$ (from $\Omega \propto M_{\text{DM}} y^2$). $\Delta = 2$ throughout the entire accessible parameter space (Eq. 57). Benchmark B4: $M_{\text{DM}} = 1$ GeV, $y = 1.46 \times 10^{-12}$; $\Delta = 2$. **(b)** Asymmetric dark matter in the $(M_{\text{DM}}, \eta_{\text{DM}}/\eta_B)$ plane (Eq. 58). The cyan dashed horizontal line marks the “canonical ADM” locus $\eta_{\text{DM}} = \eta_B$. The natural island is the hyperbola $M_{\text{DM}}(\eta_{\text{DM}}/\eta_B) = 4.7$ GeV. $\Delta = 1$ throughout (Eq. 60), the minimum possible BG measure for a non-trivial abundance map. Benchmark B5: $M_{\text{DM}} = 5$ GeV, $\eta_{\text{DM}}/\eta_B = 1$; $\Delta = 1$.

$\theta_i \simeq (0.18 (f_a/10^{12})^{1.19})^{-1/2} \approx 3 \times 10^{-3}$, well below the natural value of order unity. The local BG sensitivity at this point remains $\Delta \approx 2$, but since θ_i is a cosmological initial condition with a flat prior on $[-\pi, \pi]$, the prior probability of landing at $\theta_i \lesssim 3 \times 10^{-3}$ is $\sim 10^{-3}$, corresponding to a “prior tuning” of ~ 300 that the BG measure does not register. This distinction between local sensitivity and prior probability is discussed in detail in Sec. V E.

Figure 5(a) displays the (f_a, θ_i) parameter space. The BG heatmap transitions from yellow-green at moderate f_a (where $\Delta \approx 2.2$, dominated by Δ_{θ_i}) to yellow at small θ_i (where anharmonic contributions vanish and $\Delta \rightarrow \max(1.19, 2) = 2$). Near $\theta_i \rightarrow \pi$ (magenta dash-dotted line), Δ_{θ_i} diverges with the anharmonic enhancement, visible as a color gradient toward the top of the panel. The natural island (green hatching) runs diagonally across the panel following the $\Omega h^2 = 0.12$ contour, from large f_a and small θ_i to small f_a and $\theta_i \sim 1$. The benchmark B6 (gold star, $f_a = 10^{12}$ GeV, $\theta_i = 0.82$) and the anthropic benchmark B6_{anthr} (orange square, $f_a = 10^{16}$ GeV, $\theta_i \approx 3 \times 10^{-3}$) both lie on the $\Omega h^2 = 0.12$ contour, both with $\Delta \approx 2$, illustrating that the BG measure does not distinguish between them.

2. Post-inflationary PQ (string decay)

If PQ symmetry breaks *after* inflation, different Hubble patches independently choose their phase when the $U(1)_{\text{PQ}}$ symmetry breaks, and the axion field has no single misalignment angle. Instead, a network of cosmic strings forms at the PQ transition and radiates axions as it evolves; the axion relic density is dominated by the string-network emission rather than by misalignment [89, 90]. In this scenario the yield depends only on f_a through the string tension $\mu \propto f_a^2$ and the mass $m_a \propto f_a^{-1}$, with no free initial condition θ_i . Large-scale numerical simulations [91] find

$$\Omega_a h^2 \simeq \mathcal{C} \left(\frac{f_a}{5 \times 10^{10} \text{ GeV}} \right)^{1.19}, \quad (64)$$

where $\mathcal{C} \approx 0.12$ is calibrated so that $f_a = 5 \times 10^{10}$ GeV gives the observed abundance, and the exponent 1.19 is the same as in the misalignment case. The simulation of Ref. [91] gives a preferred range $f_a \simeq (2-8) \times 10^{10}$ GeV at 95% confidence, incorporating uncertainties from the string network logarithm and from the QCD mass modeling.

The BG measure for the post-inflationary scenario has

only a single parameter:

$$\Delta_{f_a}^{(B7)} = 1.19 \quad \forall f_a. \quad (65)$$

This is the lowest BG fine-tuning of any construction in the comparison after pure asymmetric dark matter ($\Delta = 1$), and it applies globally — not just at a benchmark, but over the entire parameter space. The post-inflationary axion scenario is also the most *predictive* dark matter construction in the comparison: it has a single parameter f_a that is constrained from above by the requirement $\Omega h^2 \leq 0.12$, from below by astrophysical bounds on the axion–photon coupling [92], and is now being targeted directly by cavity haloscope experiments [93, 94] and by the CMB Stage-4 spectral distortion measurements expected to probe $f_a \lesssim 3 \times 10^{11}$ GeV [95]. Benchmark B7 is defined by $f_a = 5 \times 10^{10}$ GeV.

Figure 5(b) displays $\Omega_a h^2$ as a function of f_a (black curve) against the constant $\Delta = 1.19$ background. The entire panel is a uniform pale yellow, the minimum of the shared color scale, confirming that the post-inflationary axion scenario sits at the floor of BG fine-tuning across all scales. The cyan band marks the preferred f_a range from the Buschmann et al. [91] simulations, which corresponds to the portion of the natural island (green shading) constrained by current simulations. The benchmark B7 (gold star) lies within both the green and cyan bands simultaneously.

V. COMPARISON AND STRUCTURAL INSIGHTS

A. The fine-tuning hierarchy

Table II ranks all twelve scenarios by Δ_{BG} , ordered from most natural to most tuned, and assigns each to one of the three universality classes defined in Sec. VB. The data reveal a clear three-tier structure whose boundaries are set by the analytic form of the abundance map, not by the nature of the dark matter candidate.

B. Three universality classes

The twelve scenarios fall into three qualitatively distinct tiers distinguished by the analytic form of their abundance maps; the precise definitions and membership are given below, and Fig. 6 summarizes the hierarchy visually.

Before discussing each tier, I establish that the classification is robust to the choice of fine-tuning measure. Table III reports all three measures, Δ_{BG} , Δ_{SR} , and ϵ , for every benchmark. The key observations are: (i) Δ_{SR} and Δ_{BG} agree to within 40% for all scenarios except B3, where both soft masses are nearly equally sensitive ($\Delta_{M_\chi} = 46$, $\Delta_{M_{\text{NLSP}}} = 48$), giving $\Delta_{\text{SR}} = \sqrt{46^2 + 48^2} \approx 67$, a factor of $\sqrt{2}$ above $\Delta_{\text{BG}} = 48$. For

TABLE II. Barbieri–Giudice fine-tuning measure at benchmarks. Scenarios are listed in order of increasing Δ . The “type” column indicates the production paradigm. The inflationary-collapse entry is a lower-end estimate (Sec. III D); the corresponding bar in Fig. 6 is shown truncated. For the first-order phase transition mechanism the transition strength parameter α has $\Delta_\alpha \approx 3$ –4 (Class I) and does not drive the dominant tuning; only the nucleation rate β/H_* is reported here. All inflationary model classes (Fig. 2) fall in Class III or beyond for standard high-reheating scenarios ($T_{\text{reh}} \gg T_{\text{form}}$, RD Layer 1 floor $\Delta_\sigma^{(\text{RD})} \approx 57$ –70); curvaton and spectator-field models move to Class II for low-reheating scenarios ($T_{\text{reh}} \lesssim T_{\text{form}}$, MD Layer 1 floor $\Delta_\sigma^{(\text{MD})} \approx 14$). The two first-order phase transition benchmarks ($\alpha = 0.3$ and $\alpha = 1.0$) are listed separately in Table III to demonstrate α -independence, but are counted as a single mechanism here.

Scenario (benchmark)	Type	Δ	Tier
Asymmetric DM (B5)	ADM	1.0	I
Axion: post-inflationary (B7)	Axion	1.19	I
PBH: DW, gravity-fixed bias	PBH	2.0	I
WIMP: off-resonance (B1)	WIMP	2.0	I
FIMP: freeze-in (B4)	FIMP	2.0	I
Axion: misalignment (B6)	Axion	2.2	I
PBH: DW, free V_b	PBH	4.5	I
PBH: early matter dom.	PBH	14	II
PBH: phase transition	PBH	35 ^a	II/III ^a
WIMP: coannihilation (B3)	WIMP	48	II
WIMP: Higgs funnel (B2)	WIMP	6500	III
PBH: inflation, single-field	PBH	$\gtrsim 10^3$	III ^{+,b}

^a $\Delta \approx 35$ uses the single-exponential approximation Eq. (30); the more accurate super-exponential collapse probability of Ref. [36] gives $\Delta \approx 265$ (Class III) at the benchmark $\beta/H_* \approx 8$, and tracing the abundance to the underlying scalar potential gives $\Delta \sim 10^3$ – 10^4 (Sec. VIB).

^b The quoted value is a lower-end estimate for single-field ultra-slow-roll and inflection-point models. Curvaton and spectator-field inflationary models are substantially more natural: $\Delta \approx 21$ –42 (Class II) for low-reheating scenarios ($T_{\text{reh}} \lesssim T_{\text{form}}$, MD Layer 1 floor), rising to $\Delta \approx 115$ –210 (Class III) for standard high-reheating scenarios ($T_{\text{reh}} \gg T_{\text{form}}$, RD Layer 1 floor); see Sec. III D and Fig. 2.

all single-parameter-dominated scenarios (B2, the two FOPT benchmarks, the MD case), SR and BG are identical to three significant figures. (ii) The island half-width ϵ is monotonically related to Δ_{BG} through $\epsilon \approx 0.69/\Delta_{\text{BG}}$ (Eq. 6), with values ranging from $\epsilon = 75\%$ for ADM to $\epsilon < 0.1\%$ for the Higgs-funnel WIMP. (iii) No scenario changes tier under either alternative measure. The three-tier classification is therefore a structural property of the abundance maps, independent of whether one uses the max (BG), quadrature (SR), or geometric (ϵ) convention.

Figure 7 displays this comparison visually. The left panel shows paired horizontal bars for Δ_{BG} (solid) and Δ_{SR} (hatched, same color) for all twelve benchmarks on a logarithmic scale, with the island half-width ϵ read off the top axis. The sole exception is benchmark B3 (WIMP coannihilation), whose SR bar (66.5, hatched) visibly extends beyond its BG bar (48.0, solid): the two

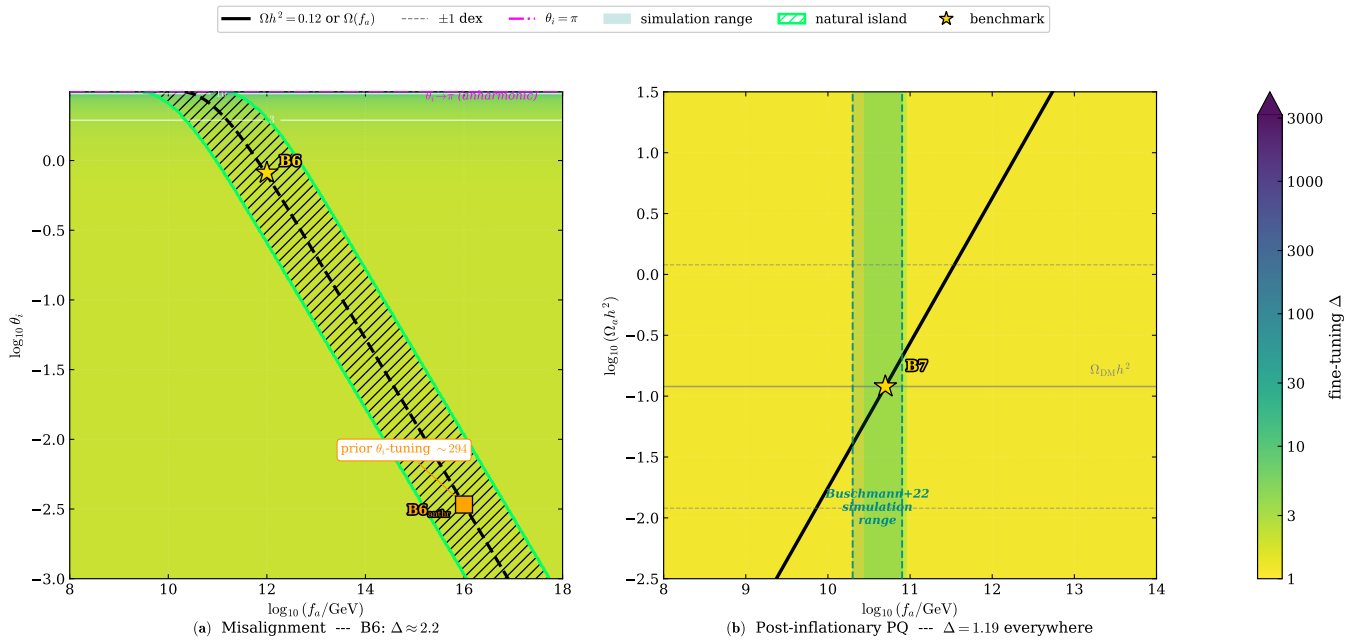


FIG. 5. Fine-tuning of QCD axion dark matter for two cosmological histories of PQ symmetry breaking. Color scale and conventions as in Fig. 1. **(a)** Misalignment mechanism (pre-inflationary PQ breaking) in the (f_a, θ_i) plane (Eq. 61). The magenta dash-dotted horizontal line at $\theta_i = \pi$ marks the onset of the anharmonic divergence $F(\theta_i) \rightarrow \infty$. The color gradient near this line reflects the diverging Δ_{θ_i} . The natural island (green hatching) runs diagonally from small f_a , $\theta_i \sim 1$ to large f_a , small θ_i . Gold star B6: $f_a = 10^{12}$ GeV, $\theta_i = 0.82$; $\Delta = 2.2$. Orange square B6_{anthr}: $f_a = 10^{16}$ GeV, $\theta_i \approx 3 \times 10^{-3}$; local $\Delta = 2.0$, but prior tuning ≈ 300 (see Sec. VE). **(b)** Post-inflationary PQ (string-network scenario), showing $\Omega_a h^2$ vs. f_a (black curve) against the uniform $\Delta = 1.19$ background (Eq. 64). The entire panel is uniformly pale yellow: $\Delta_{f_a} = 1.19$ everywhere, the lowest fine-tuning of any construction in the comparison other than pure asymmetric dark matter. The cyan shaded band marks the preferred f_a range $(2-8) \times 10^{10}$ GeV from the large-scale string-network simulations of Ref. [91]. The green shaded band marks the natural island. Gray horizontal lines show $\Omega_{\text{DM}} h^2 = 0.12$ (solid) and ± 1 dex (dashed). Gold star B7: $f_a = 5 \times 10^{10}$ GeV; $\Delta = 1.19$.

soft masses M_χ and M_{NLSP} contribute nearly equally to the log-gradient, so the quadrature adds a factor $\approx \sqrt{2}$. The right panel confirms this geometrically on a log-log scatter of Δ_{SR} vs. Δ_{BG} : every scenario except B3 lies on the solid reference line $\Delta_{\text{SR}} = \Delta_{\text{BG}}$; B3 lies exactly on the dashed $\sqrt{2}$ line. No scenario changes tier under either measure.

Class I: power-law constructions ($\Delta \lesssim 5$).— In these scenarios Ωh^2 is a monomial in the input parameters, $\Omega h^2 \propto \prod_i x_i^{\alpha_i}$, so that $\Delta_i = |\alpha_i|$ exactly. There is no exponential factor, no resonant enhancement, and no cancellation between large contributions. Class I contains seven of the twelve scenarios: asymmetric dark matter ($\Delta = 1$), the post-inflationary axion ($\Delta = 1.19$), biased-domain-wall PBHs with gravity-induced bias ($\Delta = 2$), the off-resonance WIMP ($\Delta = 2$), freeze-in via mediator decay ($\Delta = 2$), the misalignment axion at $\theta_i \sim 1$ ($\Delta = 2.2$), and biased-domain-wall PBHs with free V_b ($\Delta = 4.5$). The striking feature of Class I is its diversity: it contains representatives from every production paradigm: gravitational PBH formation, thermal freeze-out, non-thermal freeze-in, asymmetric generation, and wave-mechanical misalignment. Fine-tuning is evidently *not* a property of the nature of dark matter, but of its

abundance map.

Note that the transition strength α is a Class I parameter for the FOPT mechanism. At fixed T_* , the $f_{\text{PBH}} = 1$ contour in the $(\alpha, \beta/H_*)$ plane satisfies $\beta/H_* = \ln[T_*/(0.84T_{\text{eq}})]/S(\alpha)$, shifting by only 56% as α ranges from 0 to ∞ . The BG derivative in the α direction evaluates to $\Delta_\alpha = \beta/H_* \cdot 0.6\alpha/(\alpha + 0.3)^2 \approx 3-4$ on the natural island, placing α firmly in Class I alongside the domain-wall and off-resonance WIMP parameters. The dominant tuning cost of the FOPT mechanism is carried entirely by β/H_* , with α a spectator that shifts the required nucleation rate by a modest and calculable amount.

Class II: single-exponential constructions ($\Delta \approx 15-50$).— These scenarios contain exactly one exponential factor in Ωh^2 , whose argument is forced by $\Omega = \Omega_{\text{DM}}$ to be of order $\ln(T_{\text{form}}/T_{\text{eq}})$ or x_F . Class II contains three scenarios within the single-exponential approximation: PBH early matter domination ($\Delta = 14$), FOPT-PBH ($\Delta = 35$), and WIMP coannihilation ($\Delta = 48$). Despite spanning modulus decay, hidden-sector percolation, and electroweak-scale MSSM thermodynamics, they share the same tier because each uses a single expo-

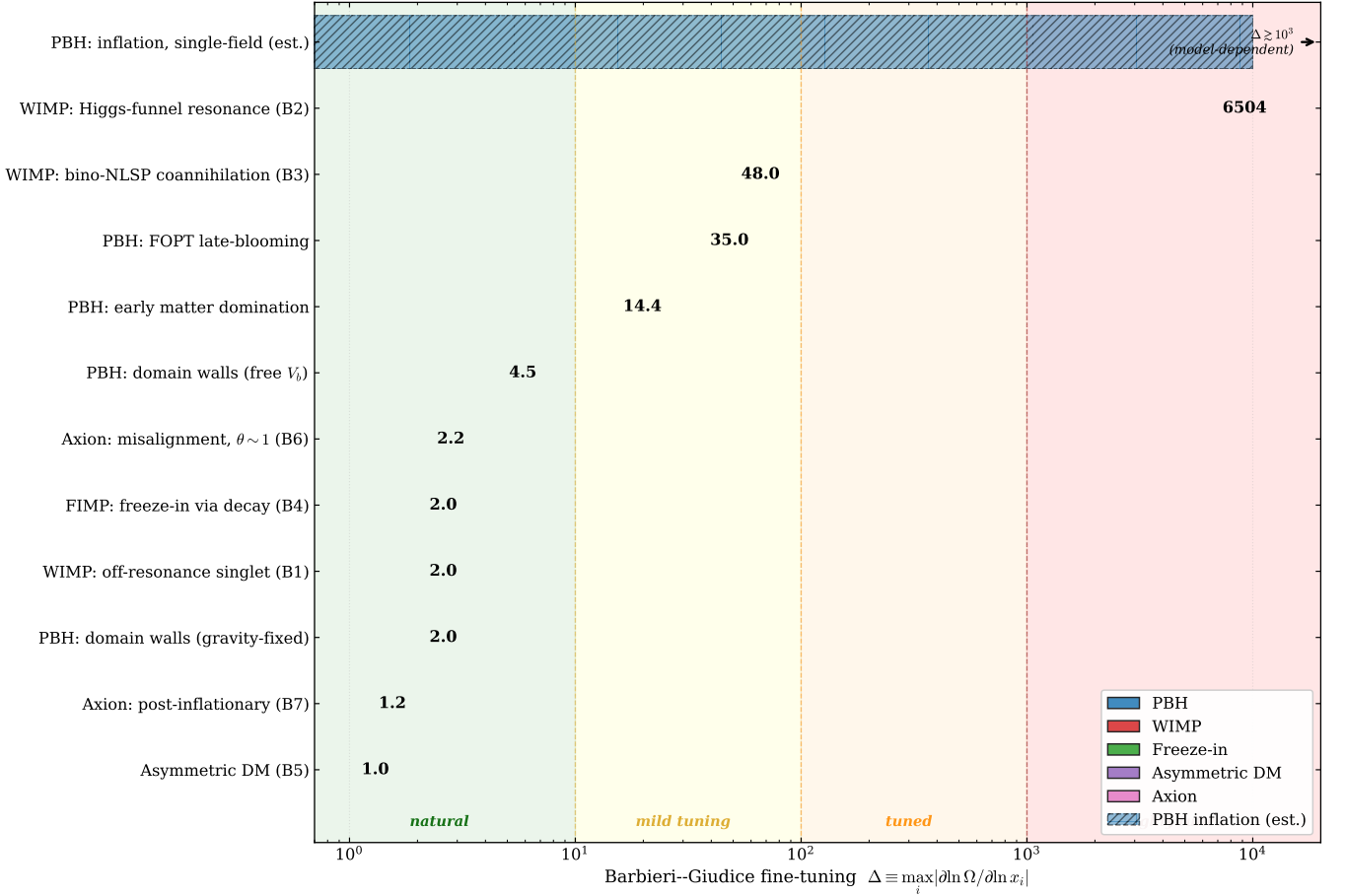


FIG. 6. Summary of the Barbieri–Giudice fine-tuning measure Δ at the benchmark points listed in Table II, ordered from most natural (bottom) to most tuned (top). Bar colors indicate the production paradigm: *blue* = PBH, *red* = thermal-relic WIMP, *green* = freeze-in (FIMP), *purple* = asymmetric dark matter, *pink* = axion. Background shading indicates qualitative tuning tiers: *green* ($\Delta < 10$, natural), *yellow* ($10 \leq \Delta < 100$, mild tuning), *orange* ($100 \leq \Delta < 1000$, tuned), *red* ($\Delta \geq 1000$, highly tuned). The topmost bar (PBH: inflation, single-field) is shown hatched and truncated with an arrow: the value is a lower-end estimate $\Delta \gtrsim 10^3$ derived from Eq. (44), with the precise value model-dependent and potentially orders of magnitude larger (see Secs. III D and V B). The FOPT-PBH bar shows $\Delta = 35$ from the single-exponential approximation Eq. (30); the more accurate super-exponential collapse probability [36] gives $\Delta \approx 265$ at the benchmark (Class III), and the microphysical estimate gives $\Delta \sim 10^3$ – 10^4 (Sec. VI B, Eq. 72). All inflationary model classes fall in Class III or beyond once the correct radiation-dominated Layer 1 floor is applied (Sec. III D and Sec. VI B).

nential to bridge the gap between a naturally large formation/annihilation rate and the small residual required by Ω_{DM} . None of the inflationary PBH model classes belong to Class II for standard high-reheating scenarios, once the correct radiation-dominated Layer 1 floor ($\Delta_{\sigma}^{(\text{RD})} \approx 57$ – 70 , Eq. 41) is used. However, for low-reheating scenarios in which the inflaton-oscillation era is still ongoing when the formation-scale perturbations re-enter the horizon ($T_{\text{reh}} \lesssim T_{\text{form}}$), the MD Layer 1 floor applies and curvaton/spectator models ($\Delta_{\text{tot}} \approx 21$ – 42) return to Class II; see Eq. (42) and Fig. 2(c). Coannihilation belongs to Class II while the standard off-resonance WIMP (B1) is Class I: in B1 the freeze-out exponential e^{-x_F} is absorbed into the power-law cross-section normalization σ_0 , leaving a pure

monomial $\Omega h^2 \propto M_S^2/\lambda_{HS}^2$; in B3 the Boltzmann suppression $e^{-x_F \delta}$ depends explicitly on the mass splitting δ , an independent Lagrangian parameter, creating the single-exponential Class II structure. We note, however, that the Class II assignment for FOPT-PBH dark matter is conditional on using the single-exponential approximation Eq. (30). Using the more accurate super-exponential collapse probability of Ref. [36] (Eq. 70) gives $\Delta_{\beta/H} \approx 265$ at the benchmark, placing FOPT-PBH in Class III at the phenomenological level. Tracing the abundance back to the underlying scalar potential reveals a further double-exponential structure [67] with $\Delta \sim 10^3$ – 10^4 (Sec. VI B); see Eq. (72)–(74) for the full assessment.

Class III and beyond: resonance, cancellation, and

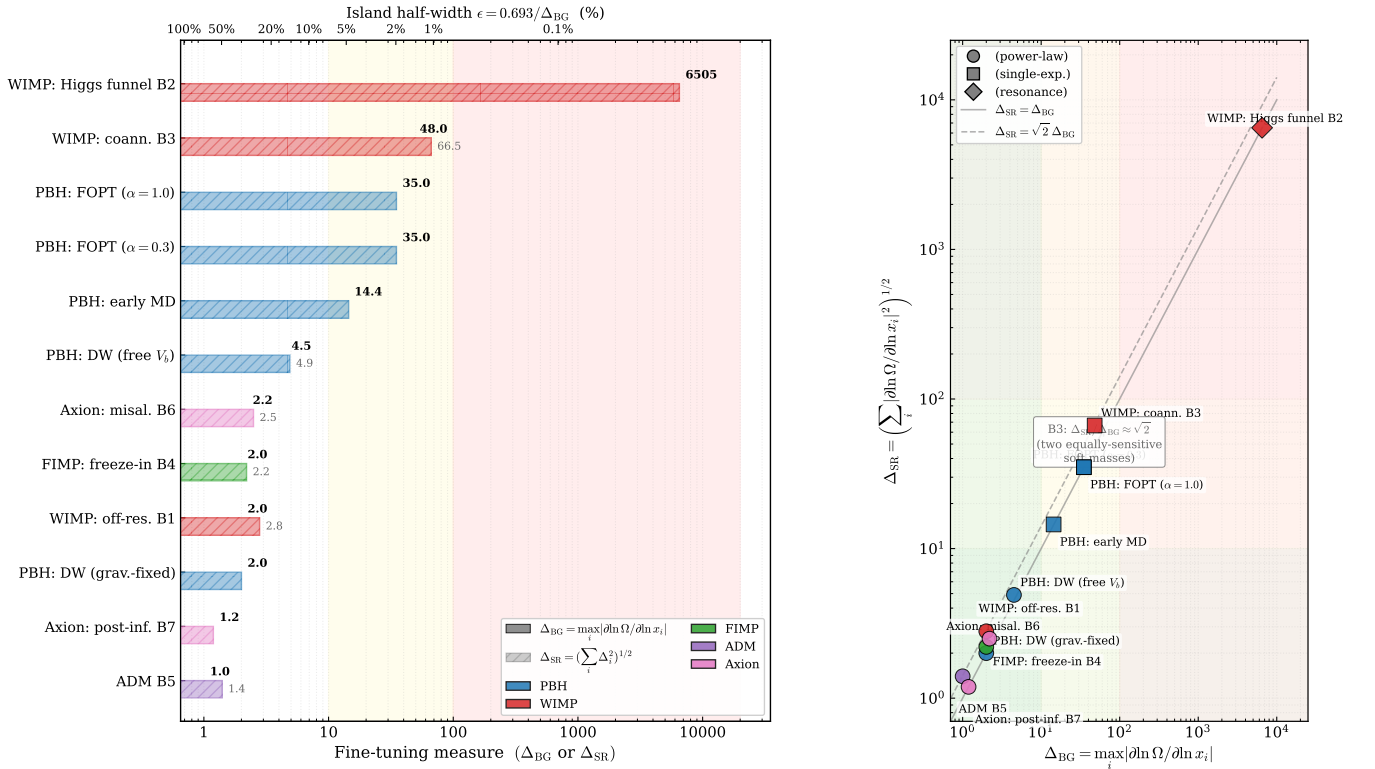


FIG. 7. Comparison of the Barbieri–Giudice (Δ_{BG}), Strumia–Rattazzi (Δ_{SR}), and island half-width (ϵ) fine-tuning measures across all benchmarks of Table III. *Left*: Paired horizontal bars for Δ_{BG} (solid) and Δ_{SR} (hatched, lighter); the top axis reads off $\epsilon = 0.693/\Delta_{BG}$ directly as a percentage. Bar colors follow the paradigm convention of Fig. 6. Background shading bands mark the three tiers. *Right*: Δ_{SR} vs. Δ_{BG} on log–log axes. Marker shapes distinguish Class I (circles), Class II (squares), and Class III (diamond). The solid gray diagonal is $\Delta_{SR} = \Delta_{BG}$; the dashed line shows $\Delta_{SR} = \sqrt{2} \Delta_{BG}$, the expectation for two equally-sensitive parameters. All scenarios lie on the solid diagonal except B3 (WIMP coannihilation, red square), which sits on the dashed line because both soft masses contribute equally. No scenario changes tier under either measure.

double-exponential constructions ($\Delta \gtrsim 10^3$).— This tier is populated by two qualitatively distinct mechanisms.

The WIMP Higgs funnel (B2, $\Delta \approx 6500$) is tuned by a Breit–Wigner resonance: the effective annihilation rate is enhanced by a factor $\sim M_h/\Gamma_h \approx 3 \times 10^4$ at the pole, reduced by thermal averaging to ~ 6500 . A 0.01% shift in M_S exits the natural island. Other resonance constructions in this tier include the MSSM A -funnel neutralino and Sommerfeld-enhanced WIMPs near an annihilation threshold.

Inflationary single-field collapse enters Class III from a structurally different direction. Its large fine-tuning arises not from a resonance but from a *double exponential*: the potential coefficients $\{c_k\}$ map exponentially onto σ , which then maps exponentially onto f_{PBH} through the HYKN formula. The BG measure for the potential coefficients is therefore (Eq. 44)

$$\Delta_{c_k} \sim \Delta_\sigma \cdot \Delta_{\sigma/c_k} \sim (57\text{--}70) \times (10^2\text{--}10^8), \quad (66)$$

far exceeding the Class II range for standard high-reheating scenarios. The large uncertainty in this estimate is intrinsic: different potential shapes produce widely varying Layer 2 sensitivities, and multi-field or

spectator-field models can reduce Δ_{σ/c_k} enough to bring the total into Class II for low-reheating scenarios ($T_{\text{reh}} \lesssim T_{\text{form}}$, MD Layer 1 floor); for standard high-reheating all inflationary classes remain in Class III or beyond (Sec. IIID).

The contrast within the PBH paradigm is striking: domain-wall and gravity-fixed PBH mechanisms sit in Class I alongside the most natural particle dark matter candidates, while single-field inflationary collapse sits in Class III or beyond. Both the lowest and the highest fine-tuning in the entire dark matter landscape belong to PBH dark matter.

C. The single-exponential universality identity

The coincidence among Class II scenarios can be stated precisely as a theorem.

Theorem. Consider any dark matter construction whose relic abundance takes the form

$$\Omega h^2 = \mathcal{A}(\{x_j\}_{j \neq i}) e^{-A x_i} \quad (67)$$

for some parameter x_i , with \mathcal{A} a function of the remain-

ing parameters that does not vanish on the $\Omega = \Omega_{\text{DM}}$ surface. Then the BG measure with respect to x_i , evaluated on the $\Omega h^2 = \Omega_{\text{DM}} h^2$ contour, satisfies

$$\Delta_{x_i} \Big|_{\Omega=\Omega_{\text{DM}}} = A x_i = \ln \left[\frac{\mathcal{A}}{\Omega_{\text{DM}} h^2} \right] \equiv \ln \left[\frac{\Omega_{\text{natural}}}{\Omega_{\text{DM}} h^2} \right], \quad (68)$$

where $\Omega_{\text{natural}} \equiv \mathcal{A}$ is the prefactor that the exponential must suppress to achieve Ω_{DM} ; it is not a physically realizable relic density (for FOPT-PBH, $\mathcal{A} = T_*/(0.84 T_{\text{eq}}) \sim 10^{14}\text{--}10^{20}$), but rather the “unquenched” abundance that would result if no exponential suppression were present.

Proof. From Eq. (67), $\partial \ln \Omega / \partial \ln x_i = -A x_i$, so $\Delta_{x_i} = A x_i$. On the $\Omega = \Omega_{\text{DM}}$ contour, $e^{-A x_i} = \Omega_{\text{DM}} / \mathcal{A}$, hence $A x_i = \ln(\mathcal{A} / \Omega_{\text{DM}})$. \square

Applying it to the Class II scenarios within the single-exponential approximation Eq. (30):

FOPT-PBH. On $f_{\text{PBH}} = 1$: $\Delta_{\beta/H} = \ln[T_*/(0.84 T_{\text{eq}})] \approx 30\text{--}37$, reproducing Eq. (37) exactly. The more accurate super-exponential formula (Sec. VIB) gives $\Delta \approx 265$ at the benchmark, so the identity holds only within the approximation and the Class II placement of FOPT-PBH is not robust.

WIMP coannihilation. On $\Omega = \Omega_{\text{DM}}$: $\Delta_{M_{\text{NLSP}}} \approx x_F M_{\text{NLSP}} / M_\chi = 48$ at benchmark B3 (Eq. 54).

PBH early matter domination. The exponential argument $0.147/\sigma^{4/3}$ evaluates to $\approx 9\text{--}19$ across the natural island. Multiplying by $4/3$ gives the contribution $0.196/\sigma^{4/3} \approx 12\text{--}25$, to which the prefactor term $+5$ is added, yielding the full $\Delta_\sigma = 5 + 0.196/\sigma^{4/3} \approx 12\text{--}21$ (Eq. 28). The approximate pure-exponential value $Ax \approx 9\text{--}19$ is smaller than the full measure because the σ^5 prefactor in Eq. (23) contributes $+\beta = +5$, a 20–35% correction at the natural-island benchmark that accounts for the difference.

Numerically,

$$\ln \left[\frac{T_{\text{form}}}{0.84 T_{\text{eq}}} \right] \approx 2.3 \log_{10} \left[\frac{T_{\text{form}}}{1 \text{ eV}} \right] \approx 30\text{--}37 \quad (69)$$

for $T_{\text{form}} \in [10^4, 10^7]$ GeV, and the WIMP coannihilation result $x_F M_{\text{NLSP}} / M_\chi$ falls in the same range. Both are set by the same cosmological clock: the ratio of the formation/freeze-out scale to T_{eq} . Note that inflationary collapse, while sharing Layer 1 of this identity ($\Delta_\sigma \approx 14$ from HYKN), does not satisfy Eq. (68) as a whole: its Layer 2 adds an additional large exponential that takes the total well outside the Class II range.

D. Sensitivity to parameter choice

The BG measure is not invariant under reparametrizations, so the values in Table II depend on the conventions of Sec. IIB. The most consequential choice is coannihilation benchmark B3.

Parametrizing by (M_χ, δ) with $\delta = (M_{\text{NLSP}} - M_\chi) / M_\chi$ gives $\Delta_\delta = x_F \delta \approx 1.3$, misleadingly low because δ vanishes at the threshold by construction. Parametrizing

by the two independent soft masses $(M_\chi, M_{\text{NLSP}})$ gives the correct $\Delta_{M_{\text{NLSP}}} = 48$ (Eq. 54). The convention is unambiguous: fundamental parameters are those independently specified at the UV scale. In the MSSM, $M_\chi = |M_1|$ and M_{NLSP} are set by independent soft terms; δ is not a Lagrangian parameter. Treating g_* as fixed introduces $\Delta_{g_*} \lesssim 0.5$, well below the dominant contributions.

E. Prior probability vs. local sensitivity

The BG measure quantifies local sensitivity: how precisely must each parameter be specified to maintain Ω_{DM} ? This differs from the prior-volume question: what fraction of randomly chosen parameter values satisfies $\Omega h^2 \in [0.06, 0.24]$?

The misalignment axion illustrates this most clearly. Benchmark B6 ($f_a = 10^{12}$ GeV, $\theta_i = 0.82$) and $B6_{\text{anthr}}$ ($f_a = 10^{16}$ GeV, $\theta_i \approx 3 \times 10^{-3}$) both have local $\Delta \approx 2.0\text{--}2.2$, since $\Omega h^2 \propto \theta_i^2$ has the same power-law structure regardless of benchmark. However, $\theta_i = 3 \times 10^{-3}$ is a factor of ~ 300 below the natural $\mathcal{O}(1)$ value; on a flat prior $[-\pi, \pi]$ the probability of landing there by chance is $\sim 10^{-3}$. This prior tuning of ~ 300 is in addition to, and qualitatively different from, the local BG measure of 2.

The same distinction is central to interpreting inflationary PBH collapse. The BG Layer 2 measure $\Delta_{c_k} \gg 10^2$ (Eq. 66) is a local sensitivity statement: how much does f_{PBH} change when c_k is varied fractionally? The Wilson naturalness argument of Iovino and Riotto [22] is instead a prior-volume statement: does a technically natural UV completion exist in which c_k takes its current value? Both are physically meaningful. This paper focuses on the local BG question throughout, which is why the inflationary entry carries a \gtrsim rather than a precise value, and why B6 and $B6_{\text{anthr}}$ receive the same tier classification.

VI. DISCUSSION

A. Implications for the primordial black hole paradigm

The central message for the PBH community is that the question “are PBHs fine-tuned?” does not have a single answer: *it crucially depends on the formation mechanism.* Among the three mechanisms analyzed in detail here, biased domain walls are genuinely natural ($\Delta = 2\text{--}4.5$), early matter domination occupies an intermediate Class II tier ($\Delta \approx 14$, comparable to the coannihilation WIMP level), and FOPT-PBH gives $\Delta \approx 35$ within the single-exponential approximation Eq. (30), rising to $\Delta \approx 265$ (Class III) with the more accurate collapse formula [36] (see Sec. VIB). When the six classes of inflationary PBH model analyzed in Sec. IIID1 are in-

cluded, the picture depends on the reheating history. For standard high-reheating scenarios ($T_{\text{reh}} \gg T_{\text{form}}$), the tuning ranges from $\Delta \approx 115\text{--}210$ for curvaton and spectator-field models (Class III, RD Layer 1 floor), through $\Delta \sim 10^2\text{--}10^3$ for step and resonance features, to $\Delta \approx 6 \times 10^3\text{--}7 \times 10^4$ (optimistic) or $\Delta \gtrsim 10^{10}$ (pessimistic) for single-field inflection-point and ultra-slow-roll models. For low-reheating scenarios ($T_{\text{reh}} \lesssim T_{\text{form}}$) where the inflaton oscillation era is still active at re-entry, the MD Layer 1 floor applies and curvaton/spectator models reduce to $\Delta \approx 21\text{--}42$ (Class II), with all other classes shifting down by a factor of ~ 5 in their Layer 1 contribution; for model classes with large Layer 2 sensitivity this shift is a minor correction to the total. The full span of the PBH fine-tuning landscape, from the gravity-fixed domain-wall construction at $\Delta = 2$ to the pessimistic single-field USR scenario at $\Delta \gg 10^4$, covers more than seven orders of magnitude — a larger range than all particle dark matter scenarios in this paper combined.

The domain-wall result deserves particular emphasis because it is least expected. Domain walls are sometimes described as a “cosmological disaster” [47, 48] requiring special engineering to avoid; the biased-wall construction turns this around, exploiting the collapse of the wall network to produce PBHs rather than treating it as a problem to be engineered away. Yet this analysis shows that the resulting abundance map contains *no* exponential: the dependence on η and V_b is purely power-law because the Hubble timescale at annihilation (which sets β_{PBH}) and the PBH mass (which sets the dilution from formation to equality) conspire to cancel all logarithmic factors. This cancellation is not an accident or a tuning; it follows algebraically from the scalings $T_{\text{ann}} \propto V_b^2/\eta^{3/2}$ and $M_{\text{PBH}} \propto \eta^3/V_b^4$. The gravity-induced-bias variant ($V_{\text{bias}} = \eta^5/M_{\text{Pl}}$) reduces the domain-wall construction to a single-parameter family with $\Delta = 2$. Among all dark matter production mechanisms, this matches the minimum achievable tuning short of the pure linear cases (ADM and post-inflationary axion), and it does so with a single technically natural small parameter: the ratio $V_{\text{bias}}/\eta^4 \sim (\eta/M_{\text{Pl}})$, which is small because $\eta \ll M_{\text{Pl}}$, not because of any special choice.

The inflationary model comparison in Fig. 2 clarifies a debate that has persisted in the literature. For high-reheating scenarios, the claim that inflationary PBH production requires fine-tuning is accurate across all inflationary model classes: the RD Layer 1 floor $\Delta_{\sigma}^{(\text{RD})} \approx 57\text{--}70$ places even the most natural inflationary class (curvaton/spectator) in Class III. For low-reheating scenarios, curvaton and spectator-field models achieve $\Delta_{\text{tot}} \approx 21\text{--}42$ (Class II), comparable to coannihilating WIMPs and the non-inflationary early-MD mechanism, while single-field USR models remain in Class III or beyond regardless of the reheating temperature. In both cases the Layer 2 sensitivity Δ_{σ/c_k} spanning five orders of magnitude from curvaton to single-field USR remains the physically informative quantity: the reheating history shifts the entire landscape up or down by a factor of five in the Layer 1

contribution, but does not change the relative ordering of model classes.

A quantitative naturalness criterion thus vindicates the biased-domain-wall PBH mechanism as robustly natural, and clarifies the status of inflationary PBH production: the frequently-stated objection that “PBH dark matter requires fine-tuning” is correct for inflationary mechanisms across all model classes under standard high-reheating assumptions, but the degree of fine-tuning spans seven orders of magnitude depending on whether the power spectrum is generated by a single-field USR phase or by a separate spectator field. More broadly, the cross-paradigm comparison shows that fine-tuning is a property of the abundance map’s analytic structure, not of whether the dark matter is a particle or a gravitational relic: the PBH paradigm alone spans all three naturalness tiers identified in this paper. Distinguishing between model classes requires precisely the framework developed here: a common measure, a common observable target, and a systematic comparison across production paradigms.

A particularly notable implication of the FOPT-PBH analysis is its multi-messenger character. The same nucleation-rate parameter $\beta/H_* \sim 5\text{--}15$ that places the PBH abundance in the asteroid-mass window also lies within the sensitivity reach of LISA and next-generation ground-based gravitational-wave detectors for the stochastic background sourced by the phase transition itself [60, 68]. This is not a coincidence engineered by model construction: it follows directly from the fine-tuning identity $S(\alpha)\beta/H_* = \ln[T_*/(0.84 T_{\text{eq}})] \approx 30\text{--}37$ (with benchmark value ≈ 35 at $T_* = 10^6$ GeV; Eq. 37), which fixes β/H_* to a window that is simultaneously relevant for PBH overproduction and for gravitational-wave detection. The more accurate super-exponential collapse probability of Ref. [36] shifts the natural island to the somewhat narrower range $\beta/H_* \sim 4\text{--}7$ (compared to the broader 5–15 from the single-exponential approximation), but preserves the overlap with the LISA sensitivity window; the multi-messenger conclusion is therefore robust, even though the fine-tuning cost is larger than the single-exponential estimate suggests, as discussed in Sec. VIB. LISA therefore has the potential to *simultaneously* constrain or confirm FOPT-PBH dark matter through two independent channels: (i) microlensing and PBH mass-function measurements in the asteroid window, and (ii) the stochastic gravitational-wave background amplitude and spectral shape. This multi-messenger leverage is unique among the PBH formation mechanisms analyzed here and makes the FOPT scenario particularly testable in the near future.

A complementary implication emerges on the particle side. The LZ 2024 results [32] eliminate much of the natural (Class I) off-resonance WIMP parameter space below ~ 1 TeV, leaving as viable primarily the Higgs-funnel (Class III, $\Delta \approx 6500$) and coannihilation (Class II, $\Delta \approx 48$) regions. As direct detection improves, the experimentally surviving WIMP parameter space migrates

toward higher tuning tiers — a trend that, if it continues, will place the most viable WIMP models at naturalness levels comparable to or worse than the FOPT-PBH scenario under its more accurate treatment (Sec. VIB).

Note that several of the Class I and Class II scenarios make near-term testable predictions: benchmark B7 (post-inflationary axion) has a model-independent prediction for f_a falsifiable by next-generation cavity haloscopes [94, 96, 97], and the early-matter-domination PBH mechanism predicts a scalar-induced gravitational-wave background detectable by LISA at $f_{\text{GW}} \sim 10^{-3}$ – 10^{-2} Hz.

B. Limitations and caveats

The analysis presented here rests on several approximations and conventions that I enumerate for completeness.

Local vs. global fine-tuning. The BG measure captures only the local, one-dimensional sensitivity to each parameter in isolation; it does not measure the total volume of the viable parameter region in the full multi-dimensional space, nor does it account for correlations between parameters. Multi-parameter generalizations of BG (including the “electroweak fine-tuning” measure [31] and Bayesian naturalness [98]) exist but require a specification of the prior, which I have deliberately avoided here; Bayesian refinements are left to future work.

Formation-rate calibration uncertainties. The domain-wall collapse fraction $p \approx 10^{-3}$ is calibrated to simulations in Ref. [51] with an order-of-magnitude uncertainty; varying p by a factor of 10 shifts the natural island in (η, V_b) without changing $\Delta = 4.5$. The HYKN formula Eq. (23) is fitted to numerical simulations for $\sigma \in [0.03, 0.2]$; extrapolation outside this range is uncertain, but the natural island lies comfortably within it. Non-Gaussian corrections to the curvature perturbation statistics can shift β_{AM} by orders of magnitude and move the natural island in σ [70], modifying the precise value of Δ_σ without changing its single-exponential class membership, since the collapse probability retains an exponential tail for any distribution with a well-defined variance. The natural island in Fig. 1(b) is also conservative in that it does not include the projected LISA constraint from the associated scalar-induced gravitational-wave background [58, 59]; including this would disfavor $\sigma \gtrsim 0.10$ across the asteroid-mass window. For benchmark B2, the thermally-averaged Breit–Wigner peak enhancement $R_{\text{max}} \approx 10^4$ is accurate to a factor of a few [29, 86]; varying it by a factor of 10 changes $\Delta^{(\text{B2})}$ by $\lesssim 30\%$, which does not affect the Class III classification.

Layer 1 floor: radiation-dominated vs. matter-dominated collapse. As discussed in Sec. IIID, the Layer 1 BG sensitivity Δ_σ for inflationary PBH models depends on whether collapse occurs in a radiation-dominated ($\Delta_\sigma^{(\text{RD})} \approx 57$ – 70) or matter-dominated ($\Delta_\sigma^{(\text{MD})} \approx 14$) background, determined entirely by the reheating temperature relative to the formation scale.

The modern numerical treatment of RD collapse [99, 100] modifies the precise value of δ_c but does not change the exponential structure $\beta_{\text{RD}} \propto \exp(-\delta_c^2/2\sigma^2)$, leaving the factor-of-five enhancement over the MD result intact; the RD tier assignments (Class III throughout) are robust to $\mathcal{O}(20\%)$ uncertainty in δ_c .

Two-layer fine-tuning structure of FOPT-PBH dark matter. Treating β/H_* as a fundamental parameter gives the single-exponential result $\Delta_{\beta/H} \approx 35$ (Class II, Sec. III C). However, the single-exponential form Eq. (30) is itself an approximation. A more complete treatment of the supercooled percolation integral [36], which tracks the full past-light-cone nucleation history, gives a super-exponential collapsed fraction

$$\mathcal{P}_{\text{coll}} \simeq \exp\left[-a\left(\frac{\beta}{H}\right)^b(1+\delta_c)^{c\beta/H}\right], \quad (70)$$

with fitted parameters $a \simeq 1.024$, $b \simeq 0.692$, $c \simeq 0.883$, valid for $\beta/H \in [3, 8]$ and $\delta_c \in [0.4, 2/3]$. The BG derivative evaluated on the $f_{\text{PBH}} = 1$ contour from Eq. (70) is

$$\Delta_{\beta/H}^{(\text{GV})} = a\left(\frac{\beta}{H}\right)^b(1+\delta_c)^{c\beta/H}\left[b+c\frac{\beta}{H}\ln(1+\delta_c)\right], \quad (71)$$

giving at the benchmark $\beta/H_* \approx 8$, $\delta_c = 0.5$:

$$\Delta_{\beta/H}^{(\text{GV})}\Big|_{\beta/H=8} \approx 265, \quad (72)$$

roughly seven times larger than the single-exponential estimate, placing FOPT-PBH in Class III at the phenomenological level. The discrepancy arises because the single-exponential approximation underestimates the steepness of the suppression: at $\beta/H \approx 8$ the outer exponent in Eq. (70) equals $a(\beta/H)^b(1+\delta_c)^{c\beta/H} \approx 75$, and the BG derivative must account for the β/H -dependence of this outer exponent itself.

At a deeper level, β/H_* is itself determined by the shape of the scalar potential. A complete analysis [67] reveals a double-exponential structure,

$$f_{\text{PBH}} \simeq M \exp[-Q \exp[-S_3(T_p)/T_p]], \quad (73)$$

where $S_3(T_p)/T_p \approx 170$ – 176 is the Euclidean action-to-temperature ratio at its minimum, $Q \sim 10^{77}$, and $M \sim 4 \times 10^7$. This is structurally identical to the Layer 1/Layer 2 decomposition of inflationary collapse (Sec. IIID): Layer 2 (potential coefficients $\{c_k\} \rightarrow S_3/T \rightarrow \beta/H_*$) introduces an additional exponential with BG sensitivity $\Delta_{S_3/T, c_k} \sim \mathcal{O}(10^2)$ – $\mathcal{O}(10^3)$, estimated from the result of Ref. [67] that a fractional shift of $\delta\mu_3/\mu_3 \sim 10^{-3}$ in the cubic potential coefficient moves f_{PBH} from $\mathcal{O}(1)$ to $\mathcal{O}(10^{-100})$. The total BG measure at the level of the potential is

$$\Delta_{c_k}^{\text{FOPT}} \sim \ln M \times \Delta_{S_3/T, c_k} \sim 17 \times (10^2\text{--}10^3) \sim 10^3\text{--}10^4, \quad (74)$$

where $\ln M \approx 17$ is the value of Qe^{-S_3/T_p} on the $f_{\text{PBH}} = 1$ contour. In summary, whether evaluated at the phenomenological level ($\Delta \approx 265$ from Eq. 70) or at the microphysical level ($\Delta \sim 10^3\text{--}10^4$ from Eq. 74), the FOPT-PBH scenario lies in Class III or beyond. The natural island in the $(T_*, \beta/H_*)$ plane is defined by $f_{\text{PBH}} \approx 1$ and its location is unchanged by the choice of formula for $\mathcal{P}_{\text{coll}}$; only the fine-tuning cost of maintaining that condition differs, and the multi-messenger implications of Sec. VIA remain valid regardless.

Gauge dependence of the FOPT nucleation rate. A recent gauge-invariant calculation [101] finds that PBH production from FOPTs may be substantially suppressed relative to the gauge-dependent estimates used in Sec. III C, potentially shifting or eliminating the natural island in the $(T_*, \beta/H_*)$ plane. Confirming or refuting this requires dedicated gauge-invariant numerical work beyond the scope of the present analysis, and the FOPT-PBH results of Sec. III C should be understood subject to this caveat.

Axion string network uncertainty. The simulation result $f_a \approx (2\text{--}8) \times 10^{10}$ GeV has a factor-of- ~ 4 range from string-network logarithm uncertainty and QCD modeling [91]. This shifts the absolute prediction for f_a but does not affect $\Delta_{f_a} = 1.19$, which is exact and independent of the normalization coefficient \mathcal{C} .

Definition of the natural island. The factor-of-two band $\Omega h^2 \in [0.06, 0.24]$ is conventional. I have verified that widening the band to a factor of five ($[0.024, 0.60]$) or narrowing it to 20% ($[0.096, 0.144]$) does not change the tier assignments in Table II.

Restricted benchmark set. This paper analyzes a curated set of twelve scenarios spanning the most widely studied production mechanisms; the two FOPT benchmarks differing only in α are counted as a single mechanism in Table II and listed separately in Table III only to demonstrate α -independence. Notable omissions include: the MSSM A -funnel (Class III, $\Delta \sim 10^3\text{--}10^4$, similar to B2); gravitational production of ultralight dark matter from de Sitter fluctuations (Class I, $\Delta \approx 2$, since $\Omega \propto H_{\text{inf}}^2/M_{\text{DM}}^2$); Hawking evaporation seeding a secondary dark matter component; and clockwork axion constructions. These are straightforward to add within the framework developed here and are left for future work.

VII. CONCLUSIONS

Primordial black holes in the asteroid-mass window ($10^{17}\text{--}10^{22}$ g) are a viable and, for some formation mechanisms, genuinely natural dark matter candidate. I have quantified this statement by applying the Barbieri–Giudice fine-tuning measure Δ uniformly to twelve dark matter scenarios spanning non-inflationary and inflationary PBH formation mechanisms, thermal-relic WIMPs, freeze-in, asymmetric dark matter, and axions. The principal conclusions are as follows.

1. *Fine-tuning is a property of the abundance map, not of the dark matter candidate.* The BG hierarchy in Table II contains representatives from every paradigm at every tier: the most natural scenario (ADM, $\Delta = 1$) and the second most natural (post-inflationary axion, $\Delta = 1.19$) are particle dark matter; Class I also includes both a WIMP and a gravitational relic (PBH-DW) at $\Delta = 2$; and the most tuned precisely computed scenario (Higgs funnel, $\Delta = 6500$) is a thermal relic, not a PBH. The narrative that “PBHs are tuned while WIMPs are natural” is not supported by a quantitative comparison.

2. *Three universality classes classify the dark matter landscape.* Class I ($\Delta \lesssim 5$) contains power-law abundance maps with no exponential factor; Class II ($\Delta \approx 15\text{--}50$) contains constructions with a single exponential; Class III and beyond ($\Delta \gtrsim 10^3$) contains resonance, cancellation, and double-exponential constructions. PBH dark matter appears in all three classes, spanning more than seven orders of magnitude in fine-tuning within the PBH paradigm alone — a larger range than all particle dark matter scenarios in this paper combined.

3. *Biased-domain-wall PBHs are as natural as any particle dark matter construction.* With $\Delta = 4.5$ in the free- V_b case and $\Delta = 2$ in the gravity-induced-bias case, domain-wall PBHs occupy Class I alongside off-resonance WIMPs and FIMPs. The characterization of PBH dark matter as “fine-tuned” does not apply to this mechanism.

4. *Single-exponential constructions satisfy a universal identity, regardless of the underlying physics.* Any construction whose abundance is set by a single exponential satisfies, on the $\Omega = \Omega_{\text{DM}}$ contour, $\Delta = \ln(\Omega_{\text{natural}}/\Omega_{\text{DM}}) \approx \ln(T_{\text{form}}/T_{\text{eq}}) \approx 14\text{--}50$ (Eq. 68). Within the single-exponential approximation, this unifies FOPT-PBH, early-matter-domination PBH, and coannihilating WIMP dark matter into Class II despite spanning modulus decay, hidden-sector percolation, and electroweak-scale MSSM thermodynamics. The Class II assignment for FOPT-PBH is however conditional on the single-exponential approximation: the more accurate super-exponential collapse probability of Ref. [36] gives $\Delta_{\beta/H} \approx 265$ at the benchmark (Class III), and tracing the abundance to the underlying scalar potential gives $\Delta \sim 10^3\text{--}10^4$ (Sec. VI B). Curvaton inflationary PBH models join Class II only for low-reheating scenarios ($T_{\text{reh}} \lesssim T_{\text{form}}$, $\Delta_{\text{tot}} \approx 21\text{--}42$); for standard high-reheating they shift to Class III.

5. *The Layer 1 floor for inflationary PBH production is set by the reheating temperature.* For standard high-reheating ($T_{\text{reh}} \gg T_{\text{form}}$), all inflationary model classes fall in Class III or beyond, with the Press–Schechter floor $\Delta_{\sigma}^{(\text{RD})} \approx 57\text{--}70$ applying universally. For low-reheating ($T_{\text{reh}} \lesssim T_{\text{form}}$), the HYKN floor $\Delta_{\sigma}^{(\text{MD})} \approx 14$ reduces the total tuning by a factor of ~ 5 , bringing curvaton and spectator-field models into Class II. Single-field USR models remain in Class III or beyond regardless of the reheating temperature. Joint constraints on T_{reh} and the inflationary power spectrum are therefore necessary to

assign a definitive naturalness tier to any inflationary PBH model.

The results above connect two largely separate prior literatures. On the particle side, the MSSM naturalness studies of Grothaus *et al.* [15] and Cabrera *et al.* [17] found that Higgs-funnel and coannihilation scenarios carry the highest relic-density fine-tuning, while bino annihilation via t -channel exchange can be “supernatural” [18]; this is fully consistent with benchmarks B1, B2, B3 falling in Classes I, III, and II respectively. On the PBH side, Hertzberg and Yamada [19] and Stamou [20] established that single-field inflection-point models require tuning to one part in 10^2 – 10^8 ; this paper identifies the origin as a Layer 2 double-exponential sensitivity $\Delta_{\sigma/c_k} \sim 10^2$ – 10^8 , distinct from the Layer 1 cost whose value depends on the reheating temperature. The recent argument of Iovino and Riotto [22] that the BG measure is defective for inflationary PBH models is resolved here: evaluating Δ on the $f_{\text{PBH}} = 1$ contour sidesteps the pathology, and the two approaches answer complementary questions within the two-layer decomposition of Sec. III D. What neither prior literature contains is a cross-paradigm comparison of the kind presented here, nor any quantitative fine-tuning analysis of the non-inflationary PBH mechanisms; the finding that biased-domain-wall PBHs achieve $\Delta = 2$ – 4.5 , competitive with the most natural particle dark matter candidates ever identified, is among the central new results of this work.

The present analysis is deliberately local in the sense of the BG measure: it quantifies how sensitively the observed abundance responds to fractional variations of each input parameter, without committing to a prior over the parameter space. A natural and well-defined extension would replace the BG measure with a Bayesian posterior-volume measure [98], allowing direct comparison with the CMSSM and NUHM analyses in the SUSY literature and yielding probabilistic statements about the likelihood of being in the natural island for each construction. The two-layer decomposition developed here provides a natural framework for such an analysis: Layer 1 and Layer 2 priors can be specified independently, reflecting the distinct physical origins of the two sources of tuning.

ACKNOWLEDGMENTS

I am grateful to Gabriele Franciolini for helpful and deep suggestions, feedback, and discussions. This work was supported by the U.S. Department of Energy, Office of Science, Office of High Energy Physics, under Award Number DE-SC0010107.

Appendix A: Analytic derivation of BG measures

1. Biased domain walls

Starting from Eqs. (13)–(16), the dark matter fraction is

$$\begin{aligned} f_{\text{PBH}} &= \frac{p V_b^4}{\frac{\pi^2}{30} g_* T_{\text{ann}}^4} \cdot \frac{T_{\text{ann}}}{0.84 T_{\text{eq}}} \\ &= \frac{30p}{\pi^2 g_* \cdot 0.84 T_{\text{eq}}} \cdot T_{\text{ann}}^{-3} V_b^4. \end{aligned} \quad (\text{A1})$$

Substituting $T_{\text{ann}} = (c_t M_{\text{Pl}} V_b^4 / \eta^3)^{1/2}$,

$$T_{\text{ann}}^{-3} = c_t^{-3/2} M_{\text{Pl}}^{-3/2} \eta^{9/2} V_b^{-6}, \quad (\text{A2})$$

so that

$$f_{\text{PBH}} \propto \eta^{9/2} V_b^{-6} \cdot V_b^4 = \eta^{9/2} V_b^{-2}. \quad (\text{A3})$$

This is Eq. (17). Log-differentiation gives $\partial \ln f_{\text{PBH}} / \partial \ln \eta = 9/2$ and $\partial \ln f_{\text{PBH}} / \partial \ln V_b = -2$, hence $\Delta_\eta = 9/2$ and $\Delta_{V_b} = 2$ identically. \square

2. Early matter domination

From $f_{\text{PBH}} = \beta_{\text{AM}}(\sigma) T_{\text{reh}} / (0.84 T_{\text{eq}})$ with $T_{\text{reh}} \propto m_\phi^{3/2}$,

$$\frac{\partial \ln f_{\text{PBH}}}{\partial \ln m_\phi} = \frac{\partial \ln T_{\text{reh}}}{\partial \ln m_\phi} = \frac{3}{2}. \quad (\text{A4})$$

For the σ -dependence, $\ln \beta_{\text{AM}} = \text{const} + 5 \ln \sigma - 0.147 \sigma^{-4/3}$, so

$$\begin{aligned} \frac{\partial \ln f_{\text{PBH}}}{\partial \ln \sigma} &= 5 + \frac{\partial}{\partial \ln \sigma} \left(-0.147 \sigma^{-4/3} \right) \\ &= 5 + \frac{4}{3} \cdot 0.147 \sigma^{-4/3} = 5 + \frac{0.196}{\sigma^{4/3}}, \end{aligned} \quad (\text{A5})$$

which is Eq. (27). \square

3. FOPT late-blooming

From Eq. (32),

$$\frac{\partial \ln f_{\text{PBH}}}{\partial \ln(\beta/H_*)} = -S(\alpha) \frac{\beta}{H_*}, \quad (\text{A6})$$

$$\frac{\partial \ln f_{\text{PBH}}}{\partial \ln T_*} = 1, \quad (\text{A7})$$

$$\frac{\partial \ln f_{\text{PBH}}}{\partial \ln \alpha} = -\frac{\partial S}{\partial \alpha} \cdot \alpha \cdot \frac{\beta}{H_*} = \frac{0.6 \alpha}{(\alpha + 0.3)^2} \cdot \frac{\beta}{H_*}, \quad (\text{A8})$$

using $\partial S / \partial \alpha = -0.6 / (\alpha + 0.3)^2$. On the $f_{\text{PBH}} = 1$ contour, $e^{-S(\alpha)\beta/H_*} = 0.84 T_{\text{eq}} / T_*$, hence $S(\alpha)\beta/H_* = \ln(T_*/0.84 T_{\text{eq}})$, giving $\Delta_{\beta/H} = |-S(\alpha)\beta/H_*| = \ln(T_*/0.84 T_{\text{eq}})$ as in Eq. (37). This derivation assumes the single-exponential Eq. (30); the more accurate super-exponential formula of Ref. [36] gives $\Delta \approx 265$ at the benchmark (Sec. VIB, Eq. 72). \square

Appendix B: Benchmark calibration

Table III summarizes the calibration of each benchmark: the parameter values, the resulting Ωh^2 , the individual BG sensitivities Δ_i for each parameter, and the total $\Delta = \max_i \Delta_i$. All quantities are computed numerically using the central-difference formula Eq. (9) with step size $h = 10^{-4}$ and independently verified against the analytic expressions derived in Appendix A and the body of the paper.

Appendix C: Figure notes

All heatmap figures (Figs. 1–5 and Fig. 7) use a shared colormap (`viridis_r`) with $\log_{10} \Delta \in [0.0, 3.5]$, saturating to dark purple for $\Delta > 3000$. Parameter-space grids are 400×400 points, logarithmically spaced. The relic abundance contours are computed from the same analytic expressions used for the Δ maps; no separate numerical Boltzmann-code integration is performed. Observational constraints (LZ 2024 direct detection, Lyman- α forest) are implemented as described in Sec. II C and Table I. The Python source codes to generate all figures is available upon request.

-
- [1] G. Jungman, M. Kamionkowski, and K. Griest, Supersymmetric dark matter, *Phys. Rep.* **267**, 195 (1996), arXiv:hep-ph/9506380.
- [2] G. Bertone, D. Hooper, and J. Silk, Particle dark matter: Evidence, candidates and constraints, *Phys. Rep.* **405**, 279 (2005), arXiv:hep-ph/0404175.
- [3] R. D. Peccei and H. R. Quinn, CP conservation in the presence of pseudoparticles, *Phys. Rev. Lett.* **38**, 1440 (1977).
- [4] S. Weinberg, A new light boson?, *Phys. Rev. Lett.* **40**, 223 (1978).
- [5] F. Wilczek, Problem of strong P and T invariance in the presence of instantons, *Phys. Rev. Lett.* **40**, 279 (1978).
- [6] L. J. Hall, K. Jedamzik, J. March-Russell, and S. M. West, Freeze-in production of FIMP dark matter, *JHEP* **2010** (3), 080, arXiv:0911.1120 [hep-ph].
- [7] J. McDonald, Thermally generated gauge singlet scalars as self-interacting dark matter, *Phys. Rev. Lett.* **88**, 091304 (2002), arXiv:hep-ph/0106249.
- [8] S. Nussinov, Technocosmology: Could a technibaryon excess provide a “natural” missing mass candidate?, *Phys. Lett. B* **165**, 55 (1985).
- [9] D. E. Kaplan, M. A. Luty, and K. M. Zurek, Asymmetric dark matter, *Phys. Rev. D* **79**, 115016 (2009).
- [10] B. J. Carr and S. W. Hawking, Black holes in the early Universe, *Mon. Not. Roy. Astron. Soc.* **168**, 399 (1974).
- [11] A. M. Green and A. R. Liddle, Constraints on the density perturbation spectrum from primordial black holes, *Phys. Rev. D* **56**, 6166 (1997), arXiv:astro-ph/9704251.
- [12] B. Carr and F. Kühnel, Primordial black holes as dark matter: Recent developments, *Ann. Rev. Nucl. Part. Sci.* **70**, 355 (2020).
- [13] A. M. Green and B. J. Kavanagh, Primordial black holes as a dark matter candidate, *J. Phys. G* **48**, 043001 (2021), arXiv:2007.10722 [astro-ph.CO].
- [14] A. Escrivà, F. Kühnel, and Y. Tada, Primordial black holes, arXiv preprint (2022), arXiv:2211.05767 [astro-ph.CO].
- [15] P. Grothaus, M. Lindner, and Y. Takanishi, Naturalness of Neutralino Dark Matter, *JHEP* **07**, 094, arXiv:1207.4434 [hep-ph].
- [16] R. Barbieri and G. F. Giudice, Upper bounds on supersymmetric particle masses, *Nucl. Phys. B* **306**, 63 (1988).
- [17] M. E. Cabrera, J. A. Casas, A. Delgado, S. Robles, and R. Ruiz de Austri, Naturalness of MSSM dark matter, *JHEP* **08**, 058, arXiv:1604.02102 [hep-ph].
- [18] S. F. King and J. P. Roberts, Natural implementation of neutralino dark matter, *JHEP* **2006** (9), 036, arXiv:hep-ph/0603095.
- [19] M. P. Hertzberg and M. Yamada, Primordial black holes from polynomial potentials in single field inflation, *Phys. Rev. D* **97**, 083509 (2018), arXiv:1712.09750 [astro-ph.CO].
- [20] I. Stamou, Mechanisms for producing primordial black holes from inflationary models beyond fine-tuning, *Universe* **10**, 241 (2024), arXiv:2404.14321 [astro-ph.CO].
- [21] A. Kalaja, N. Bellomo, N. Bartolo, D. Bertacca, S. Matarrese, I. Musco, A. Raccanelli, and L. Verde, From Primordial Black Holes Abundance to Primordial Curvature Power Spectrum (and back), *JCAP* **10**, 031, arXiv:1908.03596 [astro-ph.CO].
- [22] A. J. Iovino and A. Riotto, Are Primordial Black Holes Truly Fine-Tuned?, (2025), arXiv:2512.19668 [astro-ph.CO].
- [23] J. R. Ellis, K. Enqvist, D. V. Nanopoulos, and F. Zwirner, Observables in low-energy superstring models, *Mod. Phys. Lett. A* **1**, 57 (1986).
- [24] N. Aghanim *et al.* (Planck), Planck 2018 results. VI. Cosmological parameters, *Astron. Astrophys.* **641**, A6 (2020), erratum: *ibid.* **652** (2021) C4, arXiv:1807.06209 [astro-ph.CO].
- [25] A. Strumia, Naturalness of supersymmetric models, in *34th Rencontres de Moriond: Electroweak Interactions and Unified Theories* (1999) pp. 441–446, arXiv:hep-ph/9904247.
- [26] G. W. Anderson and D. J. Castano, Measures of fine tuning, *Phys. Lett. B* **347**, 300 (1995), arXiv:hep-ph/9409419.
- [27] M. E. Cabrera, J. A. Casas, and R. Ruiz de Austri, Bayesian approach and Naturalness in MSSM analyses for the LHC, *JHEP* **03**, 075, arXiv:0812.0536 [hep-ph].
- [28] S. P. Martin, A supersymmetry primer, *Adv. Ser. Direct. High Energy Phys.* **18**, 1 (1998), arXiv:hep-ph/9709356.
- [29] K. Griest and D. Seckel, Three exceptions in the calculation of relic abundances, *Phys. Rev. D* **43**, 3191 (1991).
- [30] J. Edsjo and P. Gondolo, Neutralino relic density including coannihilations, *Phys. Rev. D* **56**, 1879 (1997),

TABLE III. Benchmark calibration and fine-tuning measures. For each scenario the fundamental parameters are listed with their benchmark values, the resulting abundance (“ Ωh^2 ” denotes $\Omega_{\text{DM}} h^2$ for particle DM scenarios and f_{PBH} for PBH scenarios; see Sec. II C), the individual BG sensitivities Δ_1 and Δ_2 in the order listed in the parameters column, and the three summary measures: the Barbieri–Giudice measure $\Delta_{\text{BG}} = \max_i \Delta_i$ (Eq. 1), the Strumia–Rattazzi quadrature measure $\Delta_{\text{SR}} = (\sum_i \Delta_i^2)^{1/2}$ (Eq. 5), and the fractional island half-width $\epsilon = \Delta x_{\text{sens}}/x_{\text{sens}}$ in the most-sensitive parameter direction (Eq. 6, factor-of-2 abundance band). For the two FOPT benchmarks the transition strength α has $\Delta_\alpha \approx 3\text{--}4$ and does not drive the dominant tuning; it is omitted from Δ_1/Δ_2 and the benchmarks are listed separately only to demonstrate the α -independence established in Eq. (37). Benchmarks B6 and B3 do not hit $\Omega h^2 = 0.120$ exactly due to rounding in the benchmark calibration; both lie within the factor-of-two natural island. All derivatives are computed via Eq. (9) with $h = 10^{-4}$ and verified analytically where tractable (Appendix A).

Scenario	Parameters (benchmark values)	Ωh^2	Δ_1	Δ_2	Δ_{BG}	Δ_{SR}	ϵ (%)	Tier
PBH-DW (free V_b)	$\eta = 2.4 \times 10^6$ GeV, $V_b = 2$ TeV	1.02	4.5	2.0	4.5	4.9	15.5	I
PBH-DW (gravity-fixed)	$\eta = 3 \times 10^6$ GeV	1.10	2.0	—	2.0	2.0	35.4	I
PBH-MD	$m_\phi = 9 \times 10^{10}$ GeV, $\sigma = 0.055$	0.120	1.5	14.4	14.4	14.5	4.8	II
PBH-FOPT ($\alpha = 0.3$)	$T_* = 10^6$ GeV, $\beta/H_* = 7.78$	0.991	35.0	1.0	35.0	35.0	2.0	II
PBH-FOPT ($\alpha = 1.0$)	$T_* = 10^6$ GeV, $\beta/H_* = 8.84$	0.981	35.0	1.0	35.0	35.0	2.0	II
WIMP B1 (off-res.)	$M_S = 2$ TeV, $\lambda_{HS} = 1.0$	0.120	2.0	2.0	2.0	2.8	35.4	I
WIMP B2 (Higgs funnel)	$M_S = 60.7$ GeV, $\lambda_{HS} = 0.026$	0.120	6505	2.0	6505	6505	< 0.1	III
WIMP B3 (coann.)	$M_\chi = 1$ TeV, $M_{\text{NLSP}} = 1.05$ TeV	0.112	46.0	48.0	48.0	66.5	1.4	II
FIMP B4	$M_{\text{DM}} = 1$ GeV, $y = 1.46 \times 10^{-12}$	0.120	1.0	2.0	2.0	2.2	35.4	I
ADM B5	$M_{\text{DM}} = 5.0$ GeV, $R = 1.0$	0.120	1.0	1.0	1.0	1.4	75.0	I
Axion B6 (mis.)	$f_a = 10^{12}$ GeV, $\theta_i = 0.82$	0.131	1.2	2.2	2.2	2.5	32.2	I
Axion B7 (post-inf.)	$f_a = 5 \times 10^{10}$ GeV	0.120	1.2	—	1.2	1.2	61.6	I

- arXiv:hep-ph/9704361.
- [31] H. Baer, V. Barger, and A. Mustafayev, Implications of a 125 GeV Higgs scalar for LHC SUSY and neutralino dark matter searches, *Phys. Rev. D* **85**, 075010 (2012), arXiv:1112.3017 [hep-ph].
- [32] J. Aalbers *et al.* (LZ), Dark Matter Search Results from 4.2 Tonne-Years of Exposure of the LUX-ZEPLIN (LZ) Experiment, *Phys. Rev. Lett.* **135**, 011802 (2025), arXiv:2410.17036 [hep-ex].
- [33] J. M. Alarcon, J. Martin Camalich, and J. A. Oller, The chiral representation of the πN scattering amplitude and the pion-nucleon sigma term, *Phys. Rev. D* **85**, 051503 (2012), arXiv:1110.3797 [hep-ph].
- [34] G. Ballesteros, M. A. G. Garcia, and M. Pierre, How warm are non-thermal relics? Lyman- α bounds on out-of-equilibrium dark matter, *JCAP* **2021** (3), 101, arXiv:2011.13458 [hep-ph].
- [35] Q. Decant, J. Heisig, D. C. Hooper, and L. Lopez-Honorez, Lyman- α constraints on freeze-in and super-WIMPs, *JCAP* **2022** (3), 041, arXiv:2111.09321 [astro-ph.CO].
- [36] Y. Gouttenoire and E. Vitagliano, Primordial black holes and wormholes from domain wall networks, *Phys. Rev. D* **109**, 123507 (2024), arXiv:2311.07670 [hep-ph].
- [37] J. Georg and S. Watson, A Preferred Mass Range for Primordial Black Hole Formation and Black Holes as Dark Matter Revisited, *JHEP* **09**, 138, arXiv:1703.04825 [astro-ph.CO].
- [38] J. Georg, B. Melcher, and S. Watson, Primordial black holes and co-decaying dark matter, *JCAP* **2019** (11), 014, arXiv:1902.04082 [astro-ph.CO].
- [39] I. Dalianis and C. Kouvaris, Gravitational waves from density perturbations in an early matter domination era, *JCAP* **2021** (7), 046, arXiv:2012.09255 [astro-ph.CO].
- [40] B. Carr, K. Kohri, Y. Sendouda, and J. Yokoyama, Constraints on primordial black holes, *Rept. Prog. Phys.* **84**, 116902 (2021), arXiv:2002.12778 [astro-ph.CO].
- [41] J. Liu, L. Bian, R.-G. Cai, Z.-K. Guo, and S.-J. Wang, Primordial black hole production during first-order phase transitions, *Phys. Rev. D* **105**, L021303 (2022), arXiv:2106.05637 [astro-ph.CO].
- [42] M. Lewicki, P. Toczek, and V. Vaskonen, Primordial black holes from strong first-order phase transitions, *JHEP* **09**, 092, arXiv:2305.04924 [astro-ph.CO].
- [43] T. C. Gehrman, B. Shams Es Haghi, K. Sinha, and T. Xu, Baryogenesis, primordial black holes and MHz–GHz gravitational waves, *JCAP* **02**, 062, arXiv:2211.08431 [hep-ph].
- [44] G. Franciolini and A. Urbano, Primordial black hole dark matter from inflation: The reverse engineering approach, *Phys. Rev. D* **106**, 123519 (2022), arXiv:2207.10056 [astro-ph.CO].
- [45] O. Özsoy and G. Tasinato, Inflation and primordial black holes, *Universe* **9**, 203 (2023), arXiv:2301.03600 [astro-ph.CO].
- [46] J. R. Espinosa, D. Racco, and A. Riotto, Cosmological Signature of the Standard Model Higgs Vacuum Instability: Primordial Black Holes as Dark Matter, *Phys. Rev. Lett.* **120**, 121301 (2018), arXiv:1710.11196 [hep-ph].
- [47] T. W. B. Kibble, Topology of cosmic domains and strings, *J. Phys. A* **9**, 1387 (1976).
- [48] A. Vilenkin and E. P. S. Shellard, *Cosmic Strings and Other Topological Defects* (Cambridge University Press, Cambridge, 2000).
- [49] S. M. Barr and D. Seckel, Planck-scale corrections to axion models, *Phys. Rev. D* **46**, 539 (1992).
- [50] R. Holman, S. D. H. Hsu, T. W. Kephart, E. W. Kolb, R. Watkins, and L. M. Widrow, Solutions to the strong CP problem in a world with gravity, *Phys. Lett. B* **282**,

- 132 (1992), arXiv:hep-ph/9203206.
- [51] F. Ferrer, E. Massò, G. Panico, O. Pujolas, and F. Rompineve, Primordial black holes from the QCD axion, *Phys. Rev. Lett.* **122**, 101301 (2019), arXiv:1807.01707 [hep-ph].
- [52] K. J. Bae, H. Baer, V. Barger, and R. W. Deal, The cosmological moduli problem and naturalness, *JHEP* **02**, 138, arXiv:2201.06633 [hep-ph].
- [53] R. Allahverdi *et al.*, The first three seconds: A review of possible expansion histories of the early Universe, *Open J. Astrophys.* **4**, 1 (2021), arXiv:2006.16182 [astro-ph.CO].
- [54] M. Y. Khlopov and A. G. Polnarev, Primordial black holes as a cosmological test of grand unification, *Phys. Lett. B* **97**, 383 (1980).
- [55] T. Harada, C.-M. Yoo, K. Kohri, and T. Nakama, Primordial black hole formation in the matter-dominated phase of the Universe, *Phys. Rev. D* **96**, 083517 (2017), arXiv:1707.03595 [gr-qc].
- [56] W. H. Press and P. Schechter, Formation of galaxies and clusters of galaxies by self-similar gravitational condensation, *Astrophys. J.* **187**, 425 (1974).
- [57] Z. Zhou, J. Jiang, Y.-F. Cai, M. Sasaki, and S. Pi, Primordial black holes and gravitational waves from resonant amplification during inflation, *Phys. Rev. D* **102**, 103527 (2020), arXiv:2010.03537 [astro-ph.CO].
- [58] K. N. Ananda, C. Clarkson, and D. Wands, The cosmological gravitational wave background from primordial density perturbations, *Phys. Rev. D* **75**, 123518 (2007), arXiv:gr-qc/0612013.
- [59] D. Baumann, P. J. Steinhardt, K. Takahashi, and K. Ichiki, Gravitational wave spectrum induced by primordial scalar perturbations, *Phys. Rev. D* **76**, 084019 (2007), arXiv:hep-th/0703290.
- [60] C. Caprini *et al.*, Detecting gravitational waves from cosmological phase transitions with LISA: An update, *JCAP* **2020** (3), 024, arXiv:1910.13125 [astro-ph.CO].
- [61] A. D. Linde, Fate of the false vacuum at finite temperature: Theory and applications, *Phys. Lett. B* **100**, 37 (1981).
- [62] E. Witten, Cosmic separation of phases, *Phys. Rev. D* **30**, 272 (1984).
- [63] J. R. Espinosa, T. Konstandin, J. M. No, and G. Servant, Energy Budget of Cosmological First-order Phase Transitions, *JCAP* **06**, 028, arXiv:1004.4187 [hep-ph].
- [64] S. W. Hawking, I. G. Moss, and J. M. Stewart, Bubble collisions in the very early Universe, *Phys. Rev. D* **26**, 2681 (1982).
- [65] I. G. Moss, Singularity formation from colliding bubbles, *Phys. Rev. D* **50**, 676 (1994), arXiv:gr-qc/9405045 [gr-qc].
- [66] H. Kodama, M. Sasaki, and K. Sato, Abundance of primordial holes produced by cosmological first-order phase transition, *Prog. Theor. Phys.* **68**, 1979 (1982).
- [67] Y. Wu and S. Profumo, Superexponential primordial black hole production via delayed vacuum decay, *Phys. Rev. D* **111**, 103524 (2025), arXiv:2412.10666 [hep-ph].
- [68] M. Hindmarsh, S. J. Huber, K. Rummukainen, and D. J. Weir, Shape of the acoustic gravitational wave power spectrum from a first order phase transition, *Phys. Rev. D* **96**, 103520 (2017), arXiv:1704.05871 [astro-ph.CO].
- [69] K. Kohri, D. H. Lyth, and A. Melchiorri, Black hole formation and slow-roll inflation, *JCAP* **04**, 038, arXiv:0711.5006 [hep-ph].
- [70] E. V. Bugaev and P. A. Klimai, Primordial black hole constraints for curvaton models with predicted large non-Gaussianity, *Int. J. Mod. Phys. D* **22**, 1350034 (2013), arXiv:1303.3146 [astro-ph.CO].
- [71] V. Vennin, Stochastic inflation and primordial black holes, (2020), arXiv:2009.08715 [astro-ph.CO].
- [72] S. Clesse and J. García-Bellido, Massive Primordial Black Holes from Hybrid Inflation as Dark Matter and the seeds of Galaxies, *Phys. Rev. D* **92**, 023524 (2015), arXiv:1501.07565 [astro-ph.CO].
- [73] G. Ballesteros and M. Taoso, Primordial black hole dark matter from single field inflation, *Phys. Rev. D* **97**, 023501 (2018), arXiv:1709.05565 [astro-ph.CO].
- [74] H. Motohashi and W. Hu, Primordial black holes and slow-roll violation, *Phys. Rev. D* **96**, 063503 (2017), arXiv:1706.06784 [astro-ph.CO].
- [75] K. Kannike, L. Marzola, M. Raidal, and H. Veermäe, Single Field Double Inflation and Primordial Black Holes, *JCAP* **09**, 020, arXiv:1705.06225 [astro-ph.CO].
- [76] D. H. Lyth and D. Wands, Generating the curvature perturbation without an inflaton, *Phys. Lett. B* **524**, 5 (2002), arXiv:hep-ph/0110002.
- [77] K. Enqvist and M. S. Sloth, Adiabatic CMB perturbations in pre-big bang string cosmology, *Nucl. Phys. B* **626**, 395 (2002), arXiv:hep-ph/0109214.
- [78] A. A. Starobinsky and J. Yokoyama, Equilibrium state and density fluctuations in de Sitter space with and without $\lambda\phi^4$ self-interaction, *Phys. Rev. D* **50**, 6357 (1994), arXiv:astro-ph/9407016.
- [79] C. Pattison, V. Vennin, H. Assadullahi, and D. Wands, Quantum diffusion during inflation and primordial black holes, *JCAP* **10**, 046, arXiv:1707.00537 [hep-th].
- [80] J. García-Bellido, A. D. Linde, and D. Wands, Density perturbations and black hole formation in hybrid inflation, *Phys. Rev. D* **54**, 6040 (1996), arXiv:astro-ph/9605094.
- [81] Y.-F. Cai, X. Chen, M. H. Namjoo, M. Sasaki, D.-G. Wang, and Z. Wang, Revisiting non-Gaussianity from non-attractor inflation models, *JCAP* **2018** (5), 012, arXiv:1712.09998 [astro-ph.CO].
- [82] E. W. Kolb and M. S. Turner, *The Early Universe* (Addison-Wesley, Redwood City, CA, 1990).
- [83] V. Silveira and A. Zee, Scalar phantoms, *Phys. Lett. B* **161**, 136 (1985).
- [84] J. McDonald, Gauge singlet scalars as cold dark matter, *Phys. Rev. D* **50**, 3637 (1994).
- [85] C. P. Burgess, M. Pospelov, and T. ter Veldhuis, The minimal model of nonbaryonic dark matter: A singlet scalar, *Nucl. Phys. B* **619**, 709 (2001), arXiv:hep-ph/0011335.
- [86] M. Ibe, H. Murayama, and T. T. Yanagida, Breit-Wigner enhancement of dark matter annihilation, *Phys. Rev. D* **79**, 095009 (2009), arXiv:0812.0072 [hep-ph].
- [87] L. Visinelli and P. Gondolo, Dark matter axions revisited, *Phys. Rev. D* **80**, 035024 (2009), arXiv:0903.4377 [astro-ph.CO].
- [88] S. Borsanyi *et al.*, Calculation of the axion mass based on high-temperature lattice quantum chromodynamics, *Nature* **539**, 69 (2016), arXiv:1606.07494 [hep-lat].
- [89] R. L. Davis, Goldstone bosons in string models of galaxy formation, *Phys. Rev. D* **35**, 3705 (1987).
- [90] R. A. Battye and E. P. S. Shellard, Axion string constraints, *Phys. Rev. Lett.* **73**, 2954 (1994), arXiv:astro-ph/9403018.

- [91] M. Buschmann, J. W. Foster, A. Hook, A. Peterson, D. E. Willcox, W. Zhang, and B. R. Safdi, Dark matter from axion strings with adaptive mesh refinement, *Nature Commun.* **13**, 1049 (2022), arXiv:2108.05368 [hep-ph].
- [92] A. Ayala, I. Domínguez, M. Giannotti, A. Mirizzi, and O. Straniero, Revisiting the bound on axion-photon coupling from globular clusters, *Phys. Rev. Lett.* **113**, 191302 (2014), arXiv:1406.6053 [astro-ph.SR].
- [93] N. Du *et al.* (ADMX), A Search for Invisible Axion Dark Matter with the Axion Dark Matter Experiment, *Phys. Rev. Lett.* **120**, 151301 (2018), arXiv:1804.05750 [hep-ex].
- [94] K. M. Backes *et al.* (HAYSTAC), A quantum-enhanced search for dark matter axions, *Nature* **590**, 238 (2021), arXiv:2008.01853 [quant-ph].
- [95] K. Abazajian *et al.* (CMB-S4), CMB-S4 Science Book, First Edition, arXiv preprint (2016), arXiv:1610.02743 [astro-ph.CO].
- [96] Y. Kahn, B. R. Safdi, and J. Thaler, Broadband and Resonant Approaches to Axion Dark Matter Detection, *Phys. Rev. Lett.* **117**, 141801 (2016), arXiv:1602.01086 [hep-ph].
- [97] L. Brouwer *et al.* (DMRadio), Proposal for a definitive search for GUT-scale QCD axions, *Phys. Rev. D* **106**, 112003 (2022), arXiv:2203.11246 [hep-ex].
- [98] D. M. Ghilencea and G. G. Ross, The fine-tuning cost of the likelihood in SUSY models, *Nucl. Phys. B* **868**, 65 (2013), arXiv:1208.0837 [hep-ph].
- [99] I. Musco, Threshold for primordial black holes: Dependence on the shape of the cosmological perturbations, *Phys. Rev. D* **100**, 123524 (2019), arXiv:1809.02127 [gr-qc].
- [100] A. Escrivà, C. Germani, and R. K. Sheth, Universal threshold for primordial black hole formation, *Phys. Rev. D* **101**, 044022 (2020), arXiv:1907.13311 [gr-qc].
- [101] G. Franciolini, Y. Gouttenoire, and R. Jinno, Curvature Perturbations from First-Order Phase Transitions: Implications to Black Holes and Gravitational Waves, *Phys. Rev. Lett.* **136**, 171404 (2026), arXiv:2503.01962 [hep-ph].